MINIMUM-STRUCTURE BOREHOLE GRAVITY INVERSION

CRAIG R.W. MOSHER

MINIMUM–STRUCTURE BOREHOLE GRAVITY INVERSION

BY

CRAIG R. W. MOSHER

A THESIS SUBMITTED IN PARTIAL FULFILLMENT OF THE

REQUIREMENTS FOR THE DEGREE OF

MASTER OF SCIENCE

IN

EARTH SCIENCE (GEOPHYSICS)

MEMORIAL UNIVERSITY OF NEWFOUNDLAND

MAY 2009

MASTER OF SCIENCE THESIS

OF

CRAIG R. W. MOSHER

APPROVED:

Thesis Committee:

Major Professor _____

_____

_____

_____
DEAN OF THE GRADUATE SCHOOL

MEMORIAL UNIVERSITY OF NEWFOUNDLAND

2009

ABSTRACT

The borehole gravity technique has been well established in hydrocarbon exploration geophysics since the 1970's. The concept behind borehole gravity is simply to measure the variation in the Earth's gravitational field while traveling along a borehole. Densities both close to and far from the borehole can be derived from such measurements. However, the borehole gravity technique has not yet been routinely used for mineral exploration because gravimeters that fit in the narrower diameter holes used in mineral exploration have not existed. Such gravimeters are now being developed. Complementary investigation and development of interpretation procedures for borehole gravity data in a mineral exploration context are required. Here, results are presented of a study inverting synthetic borehole gravity data for three–dimensional, mineral exploration relevant Earth models. The forward-modelling on which the inversion is based is a finite–difference solution of Poisson's equation. The inversion is performed using a standard minimum–structure algorithm for multiple scenarios of varying borehole locations, amount of borehole data and varying model parameters. The intention is to demonstrate what we can expect to determine about the density variation around and between boreholes given varying amounts and locations of down-hole and surface data. It is observed that the benefits of borehole gravity data depend on the locations of the boreholes relative to the anomalous mass. Inversions which produce images of complex subsurface density distributions are attainable with the most successful models resulting from combined surface and borehole data. Minimum–structure borehole gravity inversion is shown to be a beneficial interpretation option which can provide accurate information of an anomaly's shape with proper depth resolution and density distribution.

ACKNOWLEDGMENTS

I would like to thank my co-supervisor Colin Farquharson for his support, guidance, inspiration and advice, all of which he provided in numerous ways. His teachings, company and overall influence are greatly appreciated. Equal thanks are extended to my co-supervisor Chuck Hurich for his encouragement, input and assistance throughout the project. I would also like to thank the Atlantic Innovation Fund and Vale Inco for financial support through the Inco Innovation Centre at Memorial University. Thank you to the University of British Columbia's Geophysical Inversion Facility for making their visualization program MeshTools3D available. Finally, I would like to thank my family for their continued support and love, which without none of this would have been possible.

TABLE OF CONTENTS

Page

Page

Page

Page

LIST OF TABLES

Table **Page**

LIST OF FIGURES

Figure **Page**

Figure **Page**

Figure **Page**

Figure **Page**

CHAPTER 1

Introduction

1.1 Overview

The measurement of the vertical component of gravitational acceleration is a long-standing geophysical technique that has applied to geophysical exploration since the early nineteenth century. The Earth's gravitational field is variant due to density distributions in the subsurface, therefore variations in rock densities can be examined (Reynolds, 2005).

In explorational practices, gravity is typically surveyed by means of surface and air-borne measurements. These measurements do result in successful analysis of the subsurface, however density information is focused on materials closer to the surface rather than the geology found at greater depths. For mature projects or ones which target deep into the subsurface, drilling and exploration is being performed to greater depths, meaning that surface measurements give a limited scope and are less likely to provide useful information where exploration depths reach over one kilometer (Nind et al., 2007). Due to this, gravity measurement logging along a borehole was introduced and has been used in hydrocarbon exploration since the 1970's (see, e.g., Nabighian et al. (2005)).

Despite its success, the borehole gravity technique has rarely been used in mineral exploration. The reason is generally associated with technological issues, as the gravimeters developed for hydrocarbon exploration do not fit down the narrower boreholes typically drilled in mineral exploration. However, a gravimeter to fit down slim holes is currently being developed as part of a Canadian Mining Industry Research Organization (CAMIRO) research project. Interpretation techniques for the data that will be provided by slim–hole gravimeters in a mineral exploration context are therefore required. A major objective of the study presented here is to demonstrate what one can

expect to determine about the density variation around and between boreholes given varying amounts and locations of down-hole and surface data. Investigations using the minimum–structure inversion technique are presented for the interpretation of such data.

Minimum–structure inversion of surface gravity data is now common-place. However, existing computer programs mostly cannot handle measurements from within the subsurface. This is because the forward-modelling is typically done using the expression of Nagy (1966), or similar, for the gravitational attraction of a rectangular prism. This expression is not valid for observation locations within the prism. With the introduction of borehole gravimeters to the mineral industry, there is now the need for minimum–structure inversion procedures that can handle subsurface data. The inversion procedure discussed here uses a new forward-modelling approach that incorporates the finite–difference solution to Poisson's equation making it able to invert borehole gravity data. Results are presented for simple, preliminary inversions of synthetic data for models in a zero halfspace. Later, inversions of synthetic borehole data from a model of Voisey's Bay Nickel Deposit are examined. Multiple trials involving differing scenarios of borehole data, locations of boreholes and varying inversion parameters are conducted for each starting model. Through exhaustive investigations, the results begin to illustrate the issues peculiar to the inversion of downhole gravity data.

1.2 Gravitational Theory

Newton proposed the force of gravity between two particles of mass to be directly proportional to the product of the masses and inversely proportional to the square of the distance between the centers of mass (Blakely, 1996):

$$\mathbf{F} = \gamma \frac{m m_0}{r^2} \hat{\mathbf{r}} \tag{1}$$

Where a mass m at point $P_2(x, y, z)$ and a mass m_0 at point $P_1(x', y', z')$ are separated by a distance r which is equal to $r = [(x - x')^2 + (y - y')^2 + (z - z')^2]^{1/2}$. A unit vector,

$\hat{\mathbf{r}}$ is directed from m towards m_0, and γ is the universal gravitational constant, which is equal to 6.672×10^{-8} $\mathrm{Nm^2/kg^2}$ in SI units.

The acceleration due to the force of gravity is derived by the application of Newton's second law ($F = ma$) where acceleration 'a' is noted as gravitational acceleration 'g' and 'm' is referred to as 'm_0'. By combining Newton's Second Law and equation (1), the acceleration of gravity for point P_1 acting on m is given by,

$$\mathbf{g}(P_1) = -\gamma \frac{m}{r^2} \hat{\mathbf{r}}. \tag{2}$$

It is important to note that the relationship for gravitational acceleration in equation 2 is only valid for observation points outside of the mass. An expression for observation locations inside a massive volume is derived later in the section.

Because gravity is considered a conservative field (meaning that the work done to move a mass in a gravitational field is independent of the path taken between two points), it can be represented as a scalar potential function, known as *Newtonian Potential*, by taken its gradient.

$$\mathbf{g}(P_1) = \nabla U(P_1) \tag{3}$$

giving,

$$U(P_1) = \gamma \frac{m}{r} \tag{4}$$

The Newtonian Potential is used to solve for the gravitational attraction for any observation point outside of a massive anomalous distribution of volume V. If the observation point is located at a distance r, then using the relationship for density ($dm = \rho(r)\, dv$), gravitational potential can be described as,

$$U(P_1) = \gamma \int_V \frac{dm}{r} = \gamma \int_V \frac{\rho(P_2)}{r}\, dv \tag{5}$$

Applying equation (3) to all space and in cartesian coordinates, the acceleration of gravity can be represented as,

$$\mathbf{g}(P_1) = \frac{\partial U(P_1)}{\partial x}\hat{\mathbf{i}} + \frac{\partial U(P_1)}{\partial y}\hat{\mathbf{j}} + \frac{\partial U(P_1)}{\partial z}\hat{\mathbf{k}} \tag{6}$$

However, since the gravity exploration method simply utilizes the positive vertical downward or z-direction gravitational acceleration, only $\partial U/\partial z$ is of concern. Applying this to the integral representation for potential seen in equation (5), an expression for the vertical acceleration due to gravity for any point located outside any volume of mass is derived as,

$$\mathbf{g}_z(P_1) = \frac{\partial U(P_1)}{\partial z} = -\gamma \int_V \frac{z - z'}{r^3} \rho(P_2)\, dv. \tag{7}$$

Where $dv = dx\, dy\, dz$ and in SI units, $\mathbf{g}$ is in m/s^2, ρ is in kg/m^3 and r is in meters.

The expression from equation (7) is only applicable to observation points outside of a volume of mass. If the observation point P is inside of a volume of mass, the integral of equation (5) is singular and improper. The gravitational attraction from inside a volume of mass is described by Kellogg (1967) and discussed in further detail in Section 2.3

1.3 Borehole Gravity

Because exploration is continually reaching deeper into the surface, a method to acquire information about deep geological density features is necessary. This led to the concept of measuring the Earth's gravitational field down a borehole. This method provides density information that relates to a number of important rock properties pertinent to the petroleum industry as discussed by Smith (1950) and LaFehr (1983). The first borehole gravimeter was developed by LaCoste & Romberg, commercialized in the 1970s by Edcon. From these measurements, formation bulk densities can be determined and estimates of densities from remote sensing tens or hundreds of metres into a formation can be made (Hammer, 1950).

Regardless of this success, the technique is rarely used in the mineral industry. This is because the gravimeters developed for petroleum exploration have a limited self-leveling range and do not fit down the small diameter boreholes drilled in mineral exploration. However, Scintrex (as part of a CAMIRO consortium research project) is

currently developing a gravimeter appropriately sized to travel along these slim holes while maintaining the same sensitivity specifications as modern day surface instruments. This is being done by implementing Scintrex's well proven quartz element technology into the gravity sensor (Nind et al., 2007).

The use of borehole gravity data is beneficial in many stages of mining activities such as deposit evaluation, mine planning and grade control. Two major information assets derived from borehole gravity measurement are remote detection and mean bulk density determination.

1.3.1 Remote Detection

Remote detection from borehole gravity data provides information about the distribution of the densities both close to the borehole and far into the geological formation. The application of remote detection procedures allow explorationists to estimate the depth and shape of a density anomaly. This is a process done regularly from surface gravity measurements alone, however with the additional borehole data, models can be created with increased spatial resolution and sensitivities for more deeply buried structures.

Borehole gravity data is also beneficial when combined with other geophysical detection methods. For example, when exploring possible massive sulphide deposits at greater depth, typically borehole electromagnetic (EM) logging is used for detection which provides an apparent location for conductive sulphide lenses, however does not provide a reliable measure for the mass of the source. In addition, no information is obtained as to whether the source is a sulphide body, shear–zone or a non-metallic conductor such as graphite. When used in conjunction with EM logging, borehole gravity measurement provides the answers to important questions about the unknown excess mass. Also, gravity measurements for multiple boreholes can be logged and used in conjunction with surface and airborne gravity anomalies for inversions which create three dimensional

images of the deposit with far greater depth and geometric resolution. Borehole gravity measurement is also helpful in other types of metallic and non–metallic deposits where other methods fail, provided that there is a distinguishable difference in densities between the deposit and surrounding geology.

1.3.2 Bulk Density

The introduction of borehole gravity measurement provides the ability to measure in situ bulk density. These density measurements are unaffected by casing, pore hole conditions and fluid invasion and in many situations will provide mining personnel access to quick information in determining the grade of the ore. Also, a better understanding of the grade control for many types of deposits is achieved by knowing the distinct percentage contrasts between rock and mineral, which gravity data provides. This results in an accuracy improvement over previous methods used for core analysis, which prove to be erroneous if the porosity of the ore is not correctly considered (Nind et al., 2007). Overall, an accurate measure of the in situ bulk density of the rock in mining applications is pertinent to its quality and can positively impact deposit evaluation and future planning for the mine.

1.4 Gravity Measurement

Gravity measurements are typically done at a fixed location by devices known as gravimeters. Modern day gravimeters can record measurements to a sensitivity of the order of approximately 0.001 mGals (Telford et al., 1990) or approximately a few parts per billion μGals of the normal Earth's gravitational acceleration (Nind et al., 2007). Gravimeters are essentially an extremely sensitive mechanical balance, whereas the majority are comprised of a mass hanging on a spring. Measurements are recorded when minute changes in the vertical force of gravity displace the mass against the acting restoring force of the spring. This displacement is proportionally linked to the gravitational

force by Hooke's Law, which states,

$$\Delta F = -k\Delta z, \tag{8}$$

where k is the spring constant and Δz is the vertical displacement of the mass. By applying Newton's Second Law, a measurement for the change in gravity, Δg, can be obtained.

$$\Delta F = m\Delta g$$
$$\Delta g = \frac{\Delta F}{m} = \frac{-k\Delta z}{m}. \tag{9}$$

Here, m is the value of mass. New age gravimeters employ a 'zero-length' spring that has a unique proportionality link between tension and length. This property causes the spring length to collapse to zero if all external forces are removed on the system (Telford et al., 1990). The Scintrex designed borehole gravimeter uses quartz (Nind et al., 2007) as the material for the zero–length spring (Scintrex, 2009).

Despite the presence of a density anomaly, it is not possible to determine a unique source since, similar to magnetic, radioactivity and resistivity techniques, gravity is a potential field source. Gravity measurement along a borehole is not a continuous log. Measurements are typically taken at marked depths spaced 10–50 ft apart and usually a gravimeter requires 5–10 minutes to register a recording (EDCON, Inc.).

1.4.1 Corrections to Borehole Gravity Measurement

With the ability to obtain gravity measurements along a borehole, it is important to note the corrections which need to be made to the data before an accurate representation of the gravitational differentiation is achieved. The corrections that need to be applied to gravity data are as follows (Nind et al., 2007).

Free-Air Correction

It is necessary to account for the vertical gradient of gravity for an observation location to account for the change of the force of gravity at elevation. This is known as

the free-air correction and is given by the relations (Telford et al., 1990),

$$g_{FA} = \Lambda z \tag{10}$$

$$\Lambda = 2\gamma \frac{M_e}{R_e^3} = 0.3086 \text{ mGal/m}, \tag{11}$$

where M_e and R_e are the mass and radius of the Earth respectively and z is defined as the depth of the measurement relative to the mean sea level The free-air correction, however, does not consider dense material between the station and mean sea level.

Bouguer Correction

The Bouguer correction is needed to account for the dense material that the free-air correction did not account for between the observation point and mean sea-level. For borehole gravity measurements, the Bouguer correction is equal to,

$$g_B = Bz \tag{12}$$

where,

$$B = 4\pi\gamma\rho. \tag{13}$$

Here, ρ is defined as density. The Bouguer correction is twice the value used for surface measurements. This is because the downward attraction of gravity is removed and upward attraction is added when passing downward through a dense layer (Hammer, 1950).

Depth Correction

Uncertainties in depth can result in critical errors in borehole gravity readings and strongly affect the accuracy of bulk density calculations. Therefore for the increment of gravity Δg, it is important to log the correct depth, Δz, between two stations and include the free–air vertical gravity gradient and Bouguer corrections.

$$\Delta g = (\Lambda - 4\pi\gamma\rho)\,\Delta z \tag{14}$$

If the length of the borehole L is drilled at an inclination angle ϕ then

$$\Delta z = \Delta L \sin \phi \tag{15}$$

Latitude Correction

Increases in gravity with the angle of latitude are due to the rotation of the Earth and its equatorial bulge. Similar to its surface gravity correction, all borehole gravity data must incorporate the latitude (denoted as θ) at which they were measured. The correction for latitude is performed by application of the following,

$$g_L = 0.813 \sin 2\theta - 1.78 \times 10^{-3} \sin 4\theta \tag{16}$$

Here, the gravitational latitude correction is given in units of μGal/m.

Atmospheric Pressure Correction

An increase in atmospheric pressure will decrease observed gravity values because of an increased mass in the air column above the borehole. To adjust for this factor, the following correction is applied

$$\Delta g_A = -3.6\mu \text{ Gal/kPa}. \tag{17}$$

However, if a pressure gauge is used to measure the depth of the gravimeter, an increased pressure occurs and thus, a correction of $\Delta g = -12.2$ μGal/kPa is needed.

Other Corrections

Other corrections that need to be considered when recording borehole gravity measurements include accounting for the Earth's tides which involves the time and longitude of the readings; surface topography and local mining activity; regional gravity gradient modifications, which can be present due to large scale geologic features; and corrections

for the temporal drift of the instrument which may have occurred along the length of the borehole.

With all corrections accounted for, a consistent relation between gravity measurement and density is possible.

1.5 Gravity Inversion

With the introduction of borehole gravity measurement to the mineral industry, interpretation techniques are required for the data in a mineral exploration context. Methods to model and interpret borehole gravity data are currently being conducted by the applied geophysics group of École Polytechnique de Montréal by calculating the gravity response over arbitrary polyhedrons (Giroux et al., 2007). Here, a different approach using a technique known as minimum–structure inversion is investigated for the interpretation of such data. The minimum–structure inversion method is chosen due its general reliability and robustness in producing images of the subsurface from potential static field data. The procedure has already proven successful in areas of complex geology (Constable et al., 1987; de Groot-Hedlin and Constable, 1990; Smith and Booker, 1988; Oldenburg and Li, 1994; Li and Oldenburg, 1996, 1998, 2000; Farquharson et al., 2008) and the models produced have limited artifacts that arise from noise in the observations. The borehole gravity inversion procedure presented follows a similar trend to the surface gravity minimum–structure inversion program, *GRAV3D*, created by the University of British Columbia Geophysical Inversion Facility (UBC–GIF) (Li and Oldenburg, 1996, 1998, 2000; GRAV3D, 2007). The thee-dimensional inversion program works by minimizing an objective function which includes a model structure function and data misfit function. A model is created by distributing parameters in a mesh which generate a synthetic dataset that fits the observed data. The inversion continues until the synthetic data from the distribution of parameters matches the collected data within a certain statistical misfit.

Despite being a proven method for gravity inversion, the *GRAV3D* approach is unable to incorporate measurements within the subsurface, therefore cannot make use of borehole gravity measurements. The inversion procedure shown here implements a different forward-modelling approach that is able to handle measurements inside the grid. This is performed by application of the finite–difference solution to Poisson's equation.

1.5.1 Forward Modeling

The forward modeller is an essential component to the inversion program. It is used to simulate data for particular known models to obtain synthetic observed data. Also, it is responsible for the minimization of the data misfit portion of the objective function.

The minimum–structure borehole inversion procedure investigated here implements a forward-modelling procedure that evaluates the finite–difference solution to Poisson's equation (Farquharson and Mosher, 2009) seen in equation (18) and is discussed in greater detail in Chapter 2.

$$\nabla^2 U = -4\pi\gamma\rho \tag{18}$$

Poisson's equation represents the gravitational potential in all space, either inside or outside of the mass distribution. The forward solver begins by defining the finite–difference equations associated with a finite-volume rectangular mesh. From these, a linear system of equations that provide an approximate solution to gravitational potential is generated. To maintain sparseness, a conjugate-gradient method is used to obtain the solution of the gravitational potential. Components of the gravitational acceleration are then computed using a finite–difference approximation of the gradient operator. One major advantage worth noting is the sparseness of the linear system of equations, because of this the forward solver requires much less virtual memory, therefore is less computationally taxing to run.

The finite–difference method presented here is best suited for programs which utilize a conjugate-gradient based inversion. This type of inversion does not directly evaluate

the Jacobian, however calculates the matrix-vector products implicitly in a pseudo-forward problem (Mackie and Madden, 1993; Rodi and Mackie, 2001). The use of the pseudo forward problem provides the inversion with the typical Jacobian matrix–vector products without actually having to compute the Jacobian. Since the Jacobian can be large in most modern inversions, this method ensures greater computational efficiency.

1.5.2 Minimum–Structure Inversion

The application of minimum–structure inversion has proven successful in the interpretation of gravity, magnetic, electric, and electromagnetic survey data, especially in areas with complex geology. A typical minimum–structure inversion procedure (Li and Oldenburg, 1996; Portniguine and Zhadov, 1999; Boulanger and Chouteau, 2001) parameterizes the Earth's subsurface into cubic cells which each hold a physical property, for gravity this is density, creating a right rectangular mesh. Techniques using irregular grids with arbitrarily designed polyhedrons have also been studied (Barnett, 1976; Gotze and Lahmeyer, 1988; Coggon, 1976; Singh and Guptasarma, 2001). The inversion aims to recover the parameters of a model which holds the least spatial variability. This is done by minimizing an objective function which is comprised of two parts. The first part deals with the gravity measurements and fits a set of observed data to a density model's predicted data. The second part is a model objective function which continually distributes density into the mesh until a single model is achieved which is able to adequately reproduce the observed data within a desired statistical misfit. Because the minimization is an underdetermined problem, there are a number of different density models which will fit the observed gravity measurements within a misfit. Due to this quality of non–uniqueness, there are often spatially dependent weighting functions incorporated into the model objective function to limit the number of possible density models

The issue of non–uniqueness is a common problem amongst all forms of static po-

tential field geophysical inversions. This is due to the fact that there are an infinite number of different density models which will be able to fit the finite number of density distributions. It is typical to see a priori knowledge incorporated into inversions; qualitative information already known about the subsurface. Common methods to incorporate known density contrasts, weighting parameters (Chasseriau and Chouteau, 2003), and geological constraints (Ash, 2007) into reference models are all performed to achieve a more accurate solution. Each reference model can be weighted accordingly to have differing impacts on the inversion.

Another issue commonly associated with minimum–structure inversion is the lack of apparent depth resolution which occurs for all potential field inversions. This is due to the fact that surface gravity data decay with depth (Li and Oldenburg, 1998). The result is that inversions display an excess distribution of density anomalies near the surface of the model grid. To address this problem, a depth weighting function is incorporated into the model objective function with the purpose of allocating density anomalies at depth by counteracting the natural decay of the kernels. Kernel decay issues also occur with borehole gravity inversions, however, instead of a preference for density anomalies to be allocated towards cells near the surface, the anomalies tend to appear more frequently around and along the length of a borehole. Similar to the depth weighting applied to surface inversions, a side or lateral weighting is incorporated in the minimum–structure borehole gravity inversion, which is able to relocate density anomalies away from the borehole.

Overall, the minimum–structure inversion process is generally reliable and robust, and produces models in which noise in the observations produce only a limited amount of artifacts. However, the models obtained are typically of smeared shapes and do not exhibit the sharp interfaces that are usually assumed to separate subsurface geologic structures. Techniques for developing sharper interfaces in models have been described

by Last and Kubik (1983), Portniguine and Zhadov (1999), and Farquharson (2008).

1.5.3 Models

To study the effects of borehole gravity data on minimum–structure inversions, a multitude of trials involving a differing amount of borehole data and differing borehole locations are conducted. The results for minimum–structure inversions tests are shown initially for a block and wedge–in–a–halfspace true models in Chapters 4 and 5. The observed data for the studies is of the synthetic brand and is calculated from different scenarios of borehole and surface locations. Inversions incorporating a priori information and sharper, blocky-style outcomes are also examined. Other investigations include the influence of additional weighting matrices and reference models. Finally, inversions of the main Ovoid model of Voisey's Bay nickel deposit is examined. The results illustrate some of the issues peculiar to the inversion of down-hole gravity data.

1.6 Voisey's Bay Deposit

The Voisey's Bay mining project is owned by Vale-Inco Ltd. and is a Nickel-Copper-Cobalt deposit located on the northeast coast of Labrador, Canada approximately 35 km southwest of Nain and 350 km north of Happy Valley-Goose Bay. The location on a regional geological map is seen in Figure 1. The site was discovered in 1993 by prospectors originally searching for diamonds and is now regarded as one of the most significant mineral discoveries in Canada in the past 40 years (Naldrett et al., 1996). Mining of the ore began in August, 2005 and processing began in September, 2005.

In 2007, it was believed that the main Ovoid deposit contains approximately 28.9 million tonnes of proven and probable resources. In addition to the proven and probable reserves in the Ovoid, there are an additional 38.5 million tonnes of indicated resource and 6.3 million tonnes of inferred resource (VBNC, 2009).

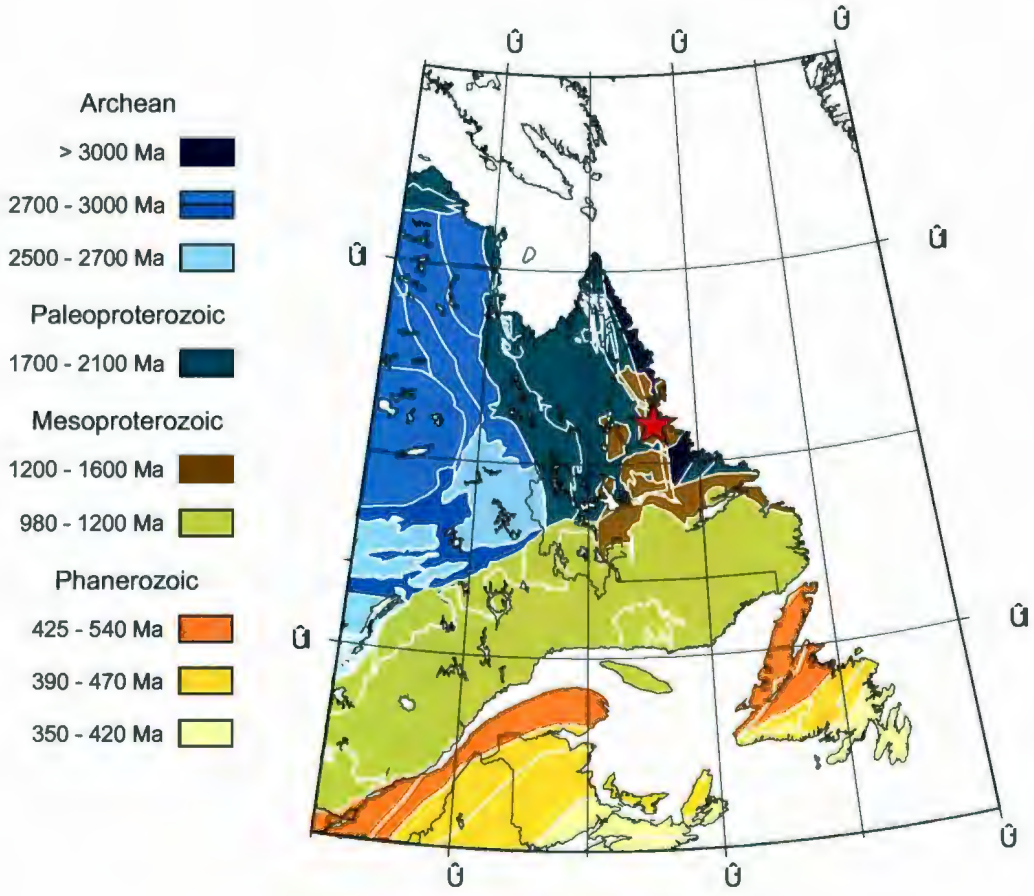

Figure 1. Regional geological map of Newfoundland and Labrador, Canada. The location of the Voisey's Bay Ni-Cu-Co deposit is indicated by the red star.

CHAPTER 2

Forward Modeller

2.1 Overview

Current three–dimensional minimum–structure inversion programs discretize the Earth to represent the subsurface. A right rectangular mesh where each cell contains a uniform density is commonly used (Bear et al., 1995; Li and Oldenburg, 1998; Portniguine and Zhadov, 1999; Nagihara and Hall, 2001; Chasseriau and Chouteau, 2003). Other techniques apply irregular grids with arbitrarily designed polyhedrons to represent the subsurface (Gotze and Lahmeyer, 1988; Singh and Guptasarma, 2001; Giroux et al., 2007), however the use of a regular rectangular grid has many advantages. Depending on the dimensions of the cells, a mesh has the potential to represent multifarious density distributions. Due to the geometric simplicity of a right rectangular mesh, a linearity relationship between the data and sought parameters is formed if mesh boundaries are fixed and if computation for the gravitational potential algorithms is simple.

To compute synthetic data for an inversion that uses a fixed mesh, it is common practice to apply a matrix-vector product:

$$\mathbf{d} = \mathbf{Gm} \tag{19}$$

where the vector $\mathbf{d}$ is formed of the synthetic values for the vertical component of the gravitational acceleration at each observation point i, the vector $\mathbf{m}$ has elements of density values that correspond to cells j, and the matrix $\mathbf{G}$ includes elements g_{ij} that contain the gravitational contribution from a particular density in the jth cell for the data evaluated at the ith observation point. This matrix $\mathbf{G}$ is known as the Jacobian or sensitivity matrix and is also required for minimizing the misfit between observed and synthetic data in a steepest-descent or Gauss-Newton inversion process.

There are multiple algorithmic variations used to express the gravitational attraction of a right rectangular prism. The algorithms have been presented in the past and a full summary is given by Li and Chouteau (1998). Most surface gravity inversion programs (Li and Oldenburg, 1998) apply the closed-form expression given by Nagy (1966), however, problems exist within this algorithm as it encounters mathematical fallacies when gravitational values at observation points inside rectangular prism are desired. In addition, other computational difficulties occur with this method when the x–axis is crossed (y boundary values have different signs), y–axis is crossed (x boundary values have different signs) or both axes are crossed. If either of these cases occur, the integral of equation (7) must be evaluated from the lower limit to zero and from zero to the upper limit. Specifically, these problems occur due to the use of an *arcsin* term in the algorithm. Methods that do not exhibit these problems are presented by Soronkin (1951), Haáz (1953), Jung (1961), Plouff (1976), and Okabe (1979), Steiner and Zilahi-Sebess (1988) and avoid error by utilizing an *arctan* term instead of *arcsin*. For the purposes of this study, the closed form formula by Okabe (1979) and Steiner and Zilahi-Sebess (1988) is used. This is given by,

$$g_{ij} = -G \sum_{i=1}^{2} \sum_{j=1}^{2} \sum_{k=1}^{2} \mu_{ijk} \left[x \ln(y_j + r_{ijk}) + y_j \ln(x + r_{ijk}) + 2z_k \arctan \frac{x_i + y_j + r_{ijk}}{z_k} \right] \tag{20}$$

where

$$r_{ijk} = \sqrt{x_i^2 + y_j^2 + z_k^2}$$

$$\mu_{ijk} = (-1)^i (-1)^j (-1)^k$$

The g_{ij} values calculated by equation (20) comprise the elements of the sensitivities matrix $\mathbf{G}$.

With a vector of densities $\mathbf{m}$ and by using equation (20) to obtain the values of $\mathbf{G}$, the vertical gravitational acceleration for any dense right rectangular mesh can be calculated at desired observation points through application of equation (19).

2.2 Computation

Although equation (19) works well for computing gravitational values, the vastness of the matrix $\mathbf{G}$ is of concern. In many Gauss-Newton inversion algorithms, the computational memory required to compute $\mathbf{G}$ and the Hessian matrix $\mathbf{G}^T\mathbf{G}$, which is also used in the inversion process, is substantial. These computational issues increase in relevance for inversions that contain large data–sets and meshes with finely discretized cells. Several methods to resolve computation memory concerns have been well documented over the years.

One method to reduce the computational size of the sensitivity matrix is presented by Oldenburg and Li (1994) who use a more general model objective function by incorporating a subspace methodology, which bypasses the full matrix computations normally found in Gauss-Newton equations. Another method is the use of conjugate–gradients to avoid the need to solve the Hessian in inversions (Li and Oldenburg, 2000) and to exploit symmetries (Boulanger and Chouteau, 2001). A method incorporating fast wavelet transforms with small wavelet coefficients is presented by Li and Oldenburg (2003). This method creates a sparse representation of the Jacobian matrix and performs fast matrix-vector multiplications in the wavelet domain for forward modelling.

The success of the forward modelling for 2-D and 3-D magnetotelluric inversions presented by Mackie and Madden (1993) and Rodi and Mackie (2001) provided the inspiration to create a similar method to forward model gravity data (Farquharson and Mosher, 2009). This method uses a conjugate–gradient procedure that implicitly performs matrix-vector products of the Jacobian. This means that the Jacobian is not actually formed, but its product with a vector is given by the solution of a pseudo–forward problem. The pseudo forward problem has the same matrix as equation (19), however incorporates the product involving the sensitivity matrix on the right hand side. Due to the sparseness of the calculations, this type of forward modeller is efficient and

produces solutions using an iterative method.

A method to forward model synthetic gravity data by use of the finite–difference solution to Poisson's equation analogous to the method of Mackie and Madden (1993) and Rodi and Mackie (2001) is presented here. The main advantages of this method are to increase computational efficiency with respect to other methods and to introduce a method for incorporating borehole gravity data into the minimum–structure inversion process. Forward modelling of gravity data for 3-D inversions by way of Poisson's equation is presented by Zhang et al. (2004), however in this paper, a finite-elements solution is used instead of applying a finite–difference procedure.

The forward modeller program described above was created by Farquharson (Farquharson and Mosher, 2009). Testing of the code was performed by Mosher and is presented in Section 2.4.

2.3 Theory

The following section describes the theoretical derivation of a finite–difference solution to Poisson's equation. The steps taken in this method are analogous to the process described by Farquharson and Mosher (2009).

The theory to determine the gravitational potential outside of a distribution of mass through the use of equation (7). is presented in Chapter 1. To derive the gravitational potential inside a volume of mass, equation (5) is re–examined first. If the observation point P is inside a volume of mass, the integral of equation (5) is singular and improper. Despite this, Kellogg (1967) shows that an integral of nature

$$U(P) = \int_V \frac{\rho}{r^n}\, dv \tag{21}$$

is convergent for any point P inside a volume V and thus is continuous throughout V provided that it is bounded, ρ is piecewise continuous, and $n < 3$. If the potential $U(P)$ and gravity $\mathbf{g}(P)$ exist and are continuous both inside and outside of a distribution of

mass, it is therefore assumed that $\mathbf{g}(P) = \nabla U(P)$ inside the mass as well. By application of the Helmholtz theorem derived from Maxwell's equations (Blakely, 1996), potential and gravity thus relate as,

$$U = \frac{1}{4\pi} \int \frac{\nabla \cdot \mathbf{g}}{r} \, dv \tag{22}$$

By rearranging equation (22) and equation (5), an expression referred to as Poisson's equation is formed,

$$\nabla^2 U(P) = -4\pi\gamma\rho(P). \tag{23}$$

Here, Poisson's equation describes the relationship between mass and potential throughout space. If no mass is present, Poisson's equation is simplified to give Laplace's equation ($\nabla^2 U = 0$). A concrete example for the derivation of Poisson's equation investigating the gravitational effects on a solid sphere is given by Blakely (1996).

The forward modeller presented here describes gravitational potential through the use of a finite–difference solution to Poisson's equation, it is derived through the use of two fundamental gravitational relations examined below. To aid in this derivation, a rectangular mesh which represents an area of interest within the subsurface is used. The center of each rectangular cell in the mesh has indices i, j and k and it is assumed that each cell has a uniform density ρ_{ijk}. A diagram of a section of the mesh is seen in Figure 2. In Figure 2, the jth plane normal to the y–direction is shown for the cell centered at point (x_i, y_j, z_k). To obtain the solution to Poisson's equation, the potential at the center of each cell and the gravitational acceleration component values at the centers of the six faces for each cell must be accounted for.

2.3.1 Potential at Cell Centers

To provide a solution for the gravitational potential at the centres of the cells, Gauss' Law for gravitational acceleration is considered, which states that for a region R bounded by a surface S, the total mass M in a region is proportional to the normal component of gravitational attraction integrated over the closed boundary of the region

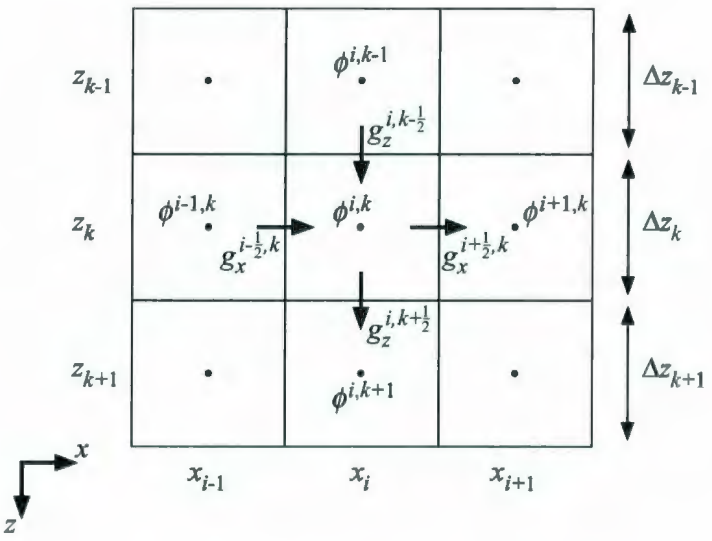

Figure 2. A section of the jth x–z plane of the mesh. The centered cell with indices (i, j, k) and surrounding cells are shown (NOTE: The index j has been removed from all shown potentials and components of the gravitational acceleration).

(Blakely, 1996),

$$-4\pi M = \int_S \mathbf{g} \cdot \hat{\mathbf{n}}\, dS = \int_R \nabla \cdot \mathbf{g}\, dv = \int_R \nabla^2 U\, dv$$

where $\mathbf{g} = \mathbf{g}(r)$ is gravity, r is the vector form source point to observation point, $\hat{\mathbf{n}}$ is outward normal unit to the surface. Then, substituting in Poisson's equation (23) yields,

$$\int_{S_{i,j,k}} \mathbf{g} \cdot \hat{\mathbf{n}}\, dS = -4\pi\gamma\rho_{i,j,k} V_{i,j,k} \tag{24}$$

where $S_{i,j,k}$ is the surface boundary of cell (i, j, k) and $V_{i,j,k}$ is the volume of the cell.

Consider the case where the gravitational acceleration of a cell face normal to the x–plane between a cell center (i, j, k) and it's adjacent cell center $(i-1, j, k)$ is desired (see Figure 2). For this case, the integral in equation (24) is denoted as $\int_{S_{i,j,k}} g_x\, dydz$. To obtain an expression for the value inside this integral, a Taylor series expansion is applied about the center of the face,

$$g_x\left(x_{i-1/2},y,z\right)=g_x^{i-1/2,j,k}+\frac{\partial g_x}{\partial y}(y-y_j)+\frac{\partial g_x}{\partial z}(z-z_k)+O\left((y-y_j)^2\right)+O\left((z-z_k)^2\right). \tag{25}$$

By integrating the Taylor series expression over the face between cells $(i-1,j,k)$ and (i,j,k), the following solution is obtained,

$$\begin{aligned}\int_{y_j-\Delta y_j/2}^{y_j+\Delta y_j/2}\int_{z_j-\Delta z_j/2}^{z_j+\Delta z_j/2} g_x\,dydz &= g_x^{i-1/2,j,k}\Delta y_j\Delta z_k \\ &\quad +O\left(\Delta y_j^2\right)\Delta y_j\Delta z_k+O\left(\Delta z_k^2\right)\Delta y_j\Delta z_k\end{aligned} \tag{26}$$

Where Δy_j and Δz_j are the lengths in the $y-$ and $z-$direction of cell (i,j,k). If the same procedure is applied to the other five sides of cell (i,j,k), then a complete representation for the approximation of Gauss' Law, equation (24), can be presented as,

$$\begin{aligned}\int_{S_{i,j,k}}\mathbf{g}\cdot\hat{\mathbf{n}}\,dS &= \left(g_x^{i+1/2,j,k}-g_x^{i-1/2,j,k}\right)\Delta y_j\Delta z_k+\left(g_y^{i,j+1/2,k}-g_x^{i,j-1/2,k}\right)\Delta x_i\Delta z_k \\ &\quad +\left(g_z^{i,j,k+1/2}-g_z^{i,j,k-1/2}\right)\Delta x_i\Delta y_j \\ &= -4\pi\gamma\rho_{i,j,k}V_{i,j,k}+O\left(\Delta^4\right).\end{aligned} \tag{27}$$

Here, the Δ term represents the linear extent of the cell in any direction. Next, dividing equation (27) by the volume of the cell results in,

$$\begin{aligned}&\frac{1}{\Delta x_i}\left(g_x^{i+1/2,j,k}-g_x^{i-1/2,j,k}\right)+\frac{1}{\Delta y_j}\left(g_y^{i,j+1/2,k}-g_x^{i,j-1/2,k}\right)+\frac{1}{\Delta z_k}\left(g_z^{i,j,k+1/2}-g_z^{i,j,k-1/2}\right) \\ &\qquad = -4\pi\gamma\rho_{i,j,k}+O\left(\Delta\right)\end{aligned} \tag{28}$$

This expression relates the components of gravitational acceleration on cell faces to each other and the density in the cell. It is noted that this is a finite–difference *approximation* to Gauss' Law, when the remainder term $O\Delta$ in equation (28) is considered insignificant and ignored. When this remainder term is ignored, equation (28) can be transformed

into a more compact matrix notation:

$$\mathbf{D}_x\mathbf{g}_x + \mathbf{D}_y\mathbf{g}_y + \mathbf{D}_z\mathbf{g}_z = \mathbf{r} \tag{29}$$

Here, the matrix $\mathbf{D}_x$ has dimensions $n_x n_y n_z$ by $(n_x + 1)\, n_y\, n_z$ and is characterized as a sparse matrix which contains $2n_x n_y n_z$ non-zero elements, where n_x, n_y and n_z are the numbers of cells in $x-$, $y-$ and $z-$directions. Values for the non-zero elements in $\mathbf{D}_x$ are $\pm 1/\Delta x_i$. Matrices $\mathbf{D}_y$ and $\mathbf{D}_z$ are created in a similar way, however have dimensions $n_x n_y n_z$ by $n_x(n_y + 1)n_z$ and $n_x n_y n_z$ by $n_x n_y(n_z + 1)$ and non-zero element values of $\pm 1/\Delta y_j$ and $\pm 1/\Delta z_k$ respectively.

The vector $\mathbf{g}_x$ contains $(n_x + 1)n_y n_z$ elements and contains the approximate values for the $x-$components of the gravitational acceleration at the centers of the cell faces that have $x-$directed normal. Vectors $\mathbf{g}_y$ and $\mathbf{g}_z$ contain $n_x(n_y + 1)n_z$ and $n_x n_y(n_z + 1)$ elements respectively and contain the gravitational acceleration approximations at the centres of their faces respective to their normals. Finally, vector $\mathbf{r}$ contains the densities of each cell and incorporates the constant $-4\pi\gamma$.

With the components of the gravitational acceleration at the center of each cell face calculated, it is now necessary to derive an expression that represents the values of the potential at the centers of each cell face to obtain a solution to Poisson's equation.

2.3.2 Gravity at Cell Faces

To obtain an expression relating the potential at cell centres to the components of the gravitational acceleration at the center of each cell face, the potential between two points is considered. Since gravity is a conservative field, gravitational potential between two points P_1 and P_2 can be expressed as,

$$\int_{P_1}^{P_2} \mathbf{g} \cdot \mathbf{dl} = U(P_2) - U(P_1) \tag{30}$$

Where $\mathbf{dl}$ is the incremental length vector along the path between the two points. If equation (30) is applied to examine the potential for the centers of two adjacent cells

(i,j,k) and $(i-1,j,k)$ in the $x-$direction,

$$\int_{x_{i-1}}^{x_i} g_x \, dx = U^{i,j,k} - U^{i-1,j,k} \tag{31}$$

Expanding g_x in a Taylor series about the center of the face separating the center of cells (i,j,k) and $(i-1,j,k)$ in the x-direction gives,

$$g_x(x, y_j, z_k) = g_x^{i-1/2,j,k} + \frac{\partial g_x}{\partial x}\left(x - x_{i-1/2}\right) + O\left(\left(x - x_{i-1/2}\right)^2\right). \tag{32}$$

Substituting the lower order approximation equation (32) into equation (30) gives,

$$g_x^{i-1/2,j,k}\left(\frac{\Delta x_{i-1}}{2} + \frac{\Delta x_i}{2}\right) = U^{i,j,k} - U^{i-1,j,k} + O\left(\Delta^3\right) \tag{33}$$

Thus,

$$g_x^{i-1/2} = \left(\frac{2}{\Delta x_{i-1} + \Delta x_i}\right) U^{i,j,k} - \left(\frac{2}{\Delta x_{i-1} + \Delta x_i}\right) U^{i-1,j,k} + O\left(\Delta^2\right) \tag{34}$$

This expression represents the $x-$component of the gravitational acceleration at the center of the cell in the $x-$normal face and is used to derive equations for all cell faces in the $x-$direction. Cells at the beginning or ending edge of the mesh, $(0,j,k)$ and (n_x+1,j,k) are incorporated as 'ghost' cells and are assigned a potential of zero. Doing so is an implicit means of applying homogeneous Dirichlet boundary conditions on the approximate potential. It is assumed that a region of non-zero density surrounding the mesh and these boundaries is sufficiently deep that it represents well actual boundary conditions of the potential at infinity. A similar method is applied for constructing equations equivalent to equation (34) in the $y-$ and $z-$directions is applied.

The remainder from equation (34) is of order Δ^2 and is once again ignored. The gravitational acceleration components for all $x-$, $y-$ and $z-$ normal cell faces can be expressed in matrix form as,

$$\mathbf{g}_x = \mathbf{F}_x \mathbf{p} \tag{35}$$

$$\mathbf{g}_y = \mathbf{F}_y \mathbf{p} \tag{36}$$

$$\mathbf{g}_z = \mathbf{F}_z \mathbf{p} \tag{37}$$

The matrices $\mathbf{F}_x$, $\mathbf{F}_y$ and $\mathbf{F}_z$ incorporate finite–difference derivatives and have dimensions $(n_x + 1)\, n_y n_z$ by $n_x n_y n_z$; $n_x\, (n_y + 1)\, n_z$ by $n_x n_y n_z$; and $n_x n_y\, (n_z + 1)$ by $n_x n_y n_z$. Each has $2 n_x n_y n_z$ non-zero elements. Respectively, the non–zero elements of each matrix are $\pm\, (2/\Delta x_{i-1} + \Delta x_i)$, $\pm\, (2/\Delta y_{i-1} + \Delta y_i)$ and $\pm\, (2/\Delta z_{i-1} + \Delta z_i)$. The vector $\mathbf{p}$ contains the values of the approximate potential at all the cell centres. Equation (37) is a finite–difference approximation for the z–component of equation (3).

By re–arranging equation (37) and equation (29), the following expression is obtained,

$$(\mathbf{D}_x \mathbf{F}_x + \mathbf{D}_y \mathbf{F}_y + \mathbf{D}_z \mathbf{F}_z)\, \mathbf{p} = \mathbf{r} \tag{38}$$

This expression is the finite–difference approximation to Poisson's equation (23) and incorporates the approximation of the homogeneous Dirichlet boundary conditions on the potential at infinity. The remainder term associated with equation (38) is of order Δ and is spawned from the remainder of order Δ^2 from equation (34) and the remainder of order Δ from equation (28).

2.4 Forward Modelling

To use the finite–difference approximation to Poisson's equation to create synthetic gravity data for a specific model, the matrices in equation (38) are constructed in a sparse matrix format (compressed sparse row). A tool kit known as SPARSKIT, specializing in sparse matrix operations, performs all the sparse matrix multiplication and addition routines necessary on the left hand side of equation (38). A conjugate–gradient routine from SPARSKIT with incomplete LU decomposition preconditioning (Saad, 2003) solves the matrix equation. This produces an approximate value for the potential at the centers of each individual cell. The potential values calculated are arranged in the vector $\mathbf{p}$ and are accurate to the order of Δ^3 (Farquharson and Mosher, 2009).

The approximate vertical component of gravitational acceleration at the z–normal

cell faces is then computed using the z–direction product of equation (37), $\hat{\mathbf{g}}_z = \mathbf{G}_z\mathbf{p}$. To obtain the vertical component of gravity at desired observation locations, linear interpolation of the two closest z–normal face centers is used.

2.4.1 Gravity Patterns

A typical borehole gravity pattern for a massive sulphide body is characterized by an increase in gravity above the center of mass of the body and a decrease below it. The cross-over point marks the approximate depth of the center of mass and the peak to peak distance provides an estimate of the distance to the center of the mass from the borehole. In general, the peak to peak distance is at a minimum for boreholes located through the center of the mass and increases as the borehole moves away from the center of mass. If the borehole does not travel deep enough to the center of the mass, then only positive gravity changes will be observed (Nind et al., 2007).

2.4.2 Example

The example presented here simulates borehole gravity measurement by use of a finite–difference approximation to Poisson's equation. Gravity values for a simple dense block in a zero halfspace are presented for different borehole locations.

To compute synthetic borehole gravity, values are calculated along the z-axis at a fixed (x, y) point. The mesh presented here has dimensions $(x, y, z) \Rightarrow (0 : 600, 0 : 600, 150 : -450)$. The density model used is a $100 \times 100 \times 100$m cube block located in the center of the mesh at $(x, y, z) \Rightarrow (250 : 350, 250 : 350, -100 : -200)$. The block cells have a density of 2000 kg/m^3, all cells not included in the block have zero density. The data for three different borehole locations, that travel the length $z \Rightarrow (0 : -300)$ are examined; one outside the block located at $(x, y) = (150, 300)$; one on the edge of the cube located at $(x, y) = (250, 300)$; and one through the middle of the cube located at $(x, y) = (300, 300)$. The locations of these boreholes and the dense cuboid model are

seen in Figure 3.

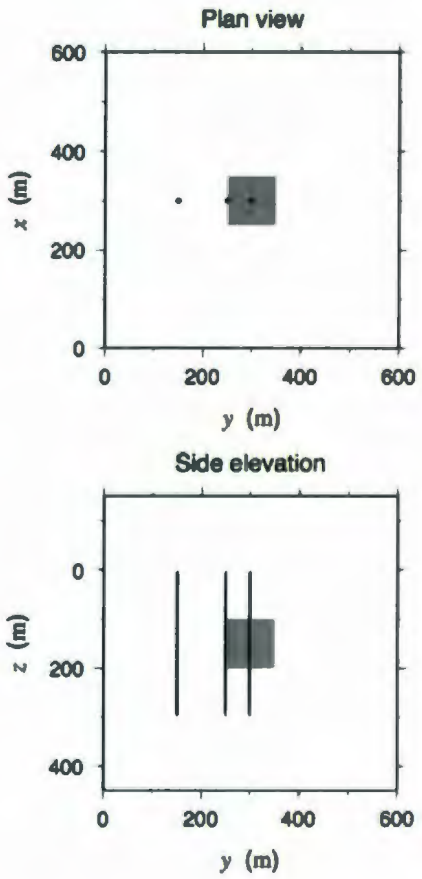

Figure 3. The dense cuboid model in gray, the boundaries of the mesh and the three borehole locations from a plan and side view. The gray cuboid has a density of 2000 kg/m^3 in a zero density wholespace.

To demonstrate the errors associated with varying the coarseness of the spatial discretization of the meshes used, four dimensionally identical meshes are examined, however each is subdivided with differently sized cubic cells. Cells sizes for the four meshes are 50, 25, 10 and 5 meters in each direction. Therefore, the first mesh has 1,728 total cells each of size $50 \times 50 \times 50m$; the second has 13,824 total cells of size $25 \times 25 \times 25m$; the third has 216,000 total cells of size $10 \times 10 \times 10m$; and the fourth has 1,728,000 total cells of size $5 \times 5 \times 5$m. The values for the vertical component of gravitational acceleration are computed from the finite–difference solution to Poisson's

equation at thirty–nine distinct observation points approximately 7.7 meters apart along the previously mentioned boreholes in each of these meshes for the cuboid density model. For comparison purposes, gravity values at identical observation points are computed for the exact density model using the gravitational attraction of a right rectangular prism presented by Okabe – Steiner and Zilahi-Sebess' formula (Li and Chouteau, 1998) seen in equation (20).

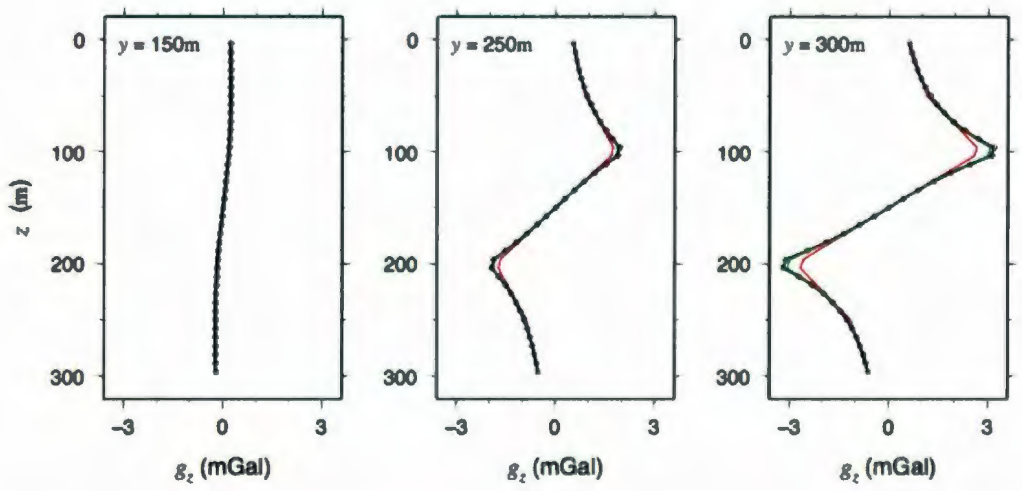

Figure 4. The gravity values calculated from the boreholes and density model seen in Figure 3. The red, green, blue and black lines represented the gravity values obtained by the finite–difference solution by using the 50, 25, 10 and 5 m meshes respectively. The closed form gravity values are in black dots.

The values for the vertical component of the gravitational acceleration for the three boreholes are seen in Figure 4.

From the graphs, the values computed by the Okabe- Steiner-Zilahi-Sebess' formula are indistinguishable from the finite–difference results for the 5 and 10 m meshes. The 25 and 50 m results follow a similar gravity distribution pattern, however deviations occur mostly at the peaks of the gravity values. The values in error for each observation point from the four finite–difference meshes is examined against the closed-form equation and plotted in Figure 5.

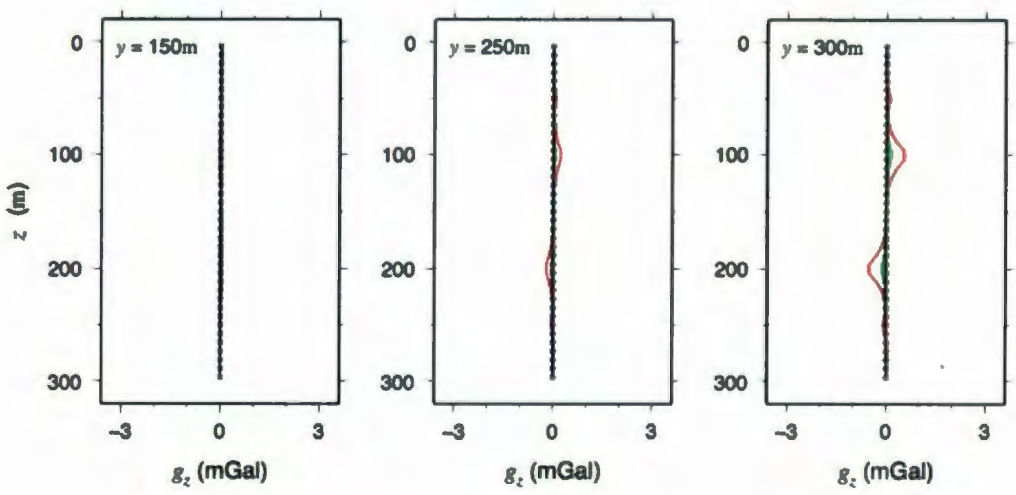

Figure 5. The errors in gravity values calculated from the boreholes and density model seen in Figure 3. The red, green, blue and black lines represent the errors in gravity values for the 50, 25, 10 and 5 m meshes respectively compared to the closed form values in black dots.

To emphasize the increased accuracy of the finite–difference approximation with finely discretized meshes, the cumulative error for the four sized meshes is calculated. The cumulative error is obtained by taking the square root of the sum of the squares for each mesh, which incorporates the error from three borehole locations. The cumulative error for the four meshes are shown in Table 1.

An integral part of the minimum–structure inversion process is employing a capable and accurate forward modeller. The forward modelling process presented here incorporates a finite–difference approximate solution to Poisson's equation. This method is able to compute gravity values within and outside of a three–dimensional dense model with good accuracy, depending on the cell discretization used. The method is efficient in computational memory usage because it avoids the creation of the full Jacobian matrix in its application. However, the method is generally slower than methods which evaluate the full Jacobian (Farquharson and Mosher, 2009). Due to the success of the finite–difference approximation to Poisson's equation for gravity measurement, it is used as

Δ	**Cumulative Error** (mGal)
50	0.3350
25	0.1498
10	0.0389
5	0.0335

Table 1. List of cumulative errors associated with cell sizes (Δ) in the different meshes.

the forward modelling method for all minimum structure inversions presented throughout the following Chapters.

CHAPTER 3

Minimum–Structure Inversion

The following chapter describes the steps necessary to perform a minimum–structure inversion. The mathematical theory is presented as well as methods used to accommodate non–uniqueness and the lack of depth resolution – common issues that affect the accuracy of the inversion problem. These difficulties are addressed by the inclusion of spatial and depth weighting functions and incorporating prior information into the inversion. The inversion algorithm used is known as *g3dfd* written by Colin Farquharson. The program works analogously to the *GRAV3D* method created by the University of British Columbia's Geophysical Inversion Facility (UBC–GIF) (Li and Oldenburg, 1998; GRAV3D, 2007), however is characterized by two main differences. First, the forward modeller uses a finite difference approximation to Poisson's equation as discussed in Chapter 2. Second, in addition to the typical l_2 style, the inversion code is able to perform l_1 style inversions which produce "blocky" models that exhibit sharper interfaces between densities.

3.1 Inversion Overview

The use of inversions for gravity data provides the ability to reconstruct density contrast models of the subsurface and is now a common practice for interpretation of surface and airborne gravity measurements.

A major issue associated with inversions of gravity data, and all static potential fields, is the non–uniqueness of the problem, meaning that there are an infinite number of possible density distributions that will reproduce the observed data (Li and Oldenburg, 1998). The cause of non–uniqueness can be attributed to a consistent problem associated with all static potential fields: a lack of depth resolution.

Many methods using differing criteria to reduce ambiguity in density distributions

have been authored. Pedersen (1979) presents a method that assumes a constant density contrast between an anomaly and outer cells, and tries to obtain the position of the polygonal or polyhedral anomaly from inversions. Methods that assume the shape or center of an anomaly and proceed to construct a density contrast as a function of spatial position have also been authored. For example, Green (1975) employs a weighted minimum distance method combined with a procedure which forces single density models. Guillen and Menichetti (1984) apply a minimization procedure using the inertia of the anomaly with respects to the center of the body or an axis which passes through it.

A method authored by Li & Oldenburg known as minimum–structure inversion to image 3–D magnetic data (Li and Oldenburg, 1996) and gravity data (Li and Oldenburg, 1998) has proven particularly successful in areas of complex geology. In this method, the earth is discretized using a right rectangular mesh. The cells of the mesh stay fixed and hold a uniform density, however the density in able to vary throughout the course of the inversion. An initial density model is input into the mesh and a forward modelling method is used to obtain a predicted gravity data–set. The predicted data–set is then matched to the initial observed data–set in hopes that it adequately satisfies a certain measure of misfit. If this does not occur, the inversion adjusts the density distribution until the predicted data and observed data are in agreement within the measure of uncertainty. The process is robust and reliable and does well to produce models which have a limited number of artifacts due to noise in the observations.

Minimum–structure inversions incorporate user controlled constraints into the minimization algorithm. The constraints can encompass a number of different physical and geological properties previously known about the subsurface. These are included in hopes of confining the inversion to a geologically reasonable result.

3.2 Theory

For minimum–structure inversions of a gravity data–set, gravity measurements and their associated errors at distinct observation locations are required. The uncertainty which accompanies each gravity datum is derived from the collection of gravity data and the Bouguer reduction techniques (Ash, 2007). The subsurface of the Earth is discretized into a mesh or grid, typically in Cartesian coordinates. Throughout the inversion, the mesh stays fixed with each cell holding a density value. The more cells in a mesh, the more flexible a representation of the Earth's subsurface is achieved.

The inversion is complete upon the minimization of an objective function. The objective function is comprised of two terms that incorporate measures of the gravity data and the density distribution, and is given by the relation,

$$\Phi = \phi_d + \beta\phi_m \tag{39}$$

where ϕ_d is the gravity data misfit, ϕ_m is the measure of model structure, and β is a trade-off parameter. The value of β is of order $\in [0, \infty]$ and is dependent on the relative importance sought between the data misfit and model structure. An ideal β value is one that produces results which fit the data neither too well (in which case the inversion is fitting the noise in the data) nor too poorly.

3.2.1 Data Misfit

The purpose of the data misfit term is to minimize the difference between the observed gravity data–set and a predicted data–set produced from an inversion model. It is defined as,

$$\phi_d = \| \mathbf{W}_d \left(\mathbf{d(m)} - \mathbf{d}^{obs} \right) \|_2^2. \tag{40}$$

Here, $\mathbf{d}^{obs}$ is the observed gravity data vector and $\mathbf{d(m)}$ is the predicted data which is produced by forward modelling of a density model $\mathbf{m}$. The diagonal matrix $\mathbf{W}_d$ incorporates the error associated with the observed gravity data and is defined as,

$$\mathbf{W}_d = \begin{pmatrix} \frac{1}{\alpha_i} & 0 & \cdots & 0 \\ 0 & \frac{1}{\alpha_i} & \cdots & 0 \\ \vdots & \vdots & \ddots & \vdots \\ 0 & 0 & \cdots & \frac{1}{\alpha_N} \end{pmatrix}$$

where α_i is the standard deviation error for the ith gravity value measurement and is assumed to be uncorrelated noise. In general, the statistical nature of the data misfit function is a χ^2–distribution, therefore an acceptable result for the inversion misfit is one that equals the number of observations. If the value of ϕ_d is lower than the number of observations, it is assumed statistically that the predicted gravity data–set is fitting the observed data–set too well and therefore fitting the error associated with the observed data–set.

3.2.2 Model Structure

Since there are multiple models that are able to fit the observed gravity data, a model objective function is vital to minimize the number of density models that satisfy the data misfit constraints. The model objective function incorporates different weighting functions and a reference model $\mathbf{m}_0$, which can be adjusted depending on a priori knowledge and the nature of the inversion. The model objective function is defined as,

$$\begin{aligned} \phi_m = & \alpha_s \int_V w_s \left\{ w(z) \left[\mathbf{m} - \mathbf{m}_0 \right] \right\}^2 dv \\ & + \alpha_x \int_V w_x \left\{ \frac{\partial w(z) \left[\mathbf{m} - \mathbf{m}_0 \right]}{\partial x} \right\}^2 dv \\ & + \alpha_y \int_V w_y \left\{ \frac{\partial w(z) \left[\mathbf{m} - \mathbf{m}_0 \right]}{\partial y} \right\}^2 dv \\ & + \alpha_z \int_V w_z \left\{ \frac{\partial w(z) \left[\mathbf{m} - \mathbf{m}_0 \right]}{\partial z} \right\}^2 dv. \end{aligned} \tag{41}$$

Where $w(z)$ is a depth weighting function, $\mathbf{m}$ is a density vector and functions w_s, w_x, w_y and w_z are spatially dependent weighting functions. The terms α_s, α_x, α_y and α_z are coefficients that affect the relative importance of different components in the objective function (Li and Oldenburg, 1996). The models produced by minimum–

structure inversions are generally smoothed images with little density variation from one cell to its adjacent. The ratio between the α terms impacts the smoothness that is present in the model. The smoothness increases as the ratio between α_x/α_s, α_y/α_s and α_z/α_s increases in each axis direction respectively.

The function w_s controls how close the final model $\mathbf{m}$ is to the reference model $\mathbf{m}_0$. The reference model can include densities that have been estimated from previous models or can be a zero model. The weighting functions w_x, w_y and w_z are designed to allow for enhancement or attenuation in their respective axes in various regions of the model domain. The reference model and four weighting functions are included into the minimization to incorporate additional information in hopes that a model is recreated that not only fits the data adequately but also more accurately represents the subsurface. Additional information that can be included comes from knowledge of density contrast, other geophysical surveys, and interpretations of the regional geologic structures and their relationship to density.

3.2.3 Depth Weighting

In surface gravity inversions, the lack of depth resolution is a problem. This applies to all static potential field data when trying to minimize a function of nature $\|\rho\|^2 = \int \rho^2 dv$ as is the case for equation 39. This arises on account of the created models direct linear combination with the kernel functions. The nature of the kernel function amplitudes are to rapidly decay with depth (Li and Oldenburg, 1998). This results in model outcomes where density distribution is concentrated near the surface of the mesh despite the presence of a dense body source at depth. To address this situation, Li and Oldenburg (1998) note that the gravitational kernels decay with an inverse distance squared relation and introduce a depth weighting function for surface gravity inversions defined as,

$$w(z) = \frac{1}{(z + z_0)^{\beta/2}}, \tag{42}$$

This function is incorporated into the inversion to counteract the geometric decay of the kernels and encourage the inversion to distribute density in cells distant from the surface with equal probability. For surface gravity inversions, β is usually equal to two and the value of z_0 is dependent on the cell size defined in the mesh and the observation height at which the data was recorded.

Similarly, in borehole gravity inversions, a weighting function is needed to counteract the natural decay of kernels away from the observation locations along a borehole. For 3–D inversion of borehole magnetic data, Li and Oldenburg (2000) present a method to address this problem by introduction of a distance–based weighting function. Thus, a distance weighting is defined by the distance between cells and observation locations whether they are recorded at surface or along boreholes. The distance weighting function combines the distance characteristics of the original depth weighting for surface data (equation (42)) with the generality of root mean squared sensitivities for all cells in all directions. The distance weighting function is given by,

$$w_j = \left\{ \sum_{i=1}^{N} \left[\int_{\Delta V_j} \frac{dv}{(r_{ij} + r_0)^{\tilde{\beta}}} \right]^2 \right\}^{\sigma/4} \quad j = 1, ..., M. \tag{43}$$

Here, N is the number of data points, M is the number of cells in the mesh, ΔV_j is the volume of the jth cell and r_{ij} is the distance between the ith observation and any point within ΔV_j. The parameter r_0 is a constant and typically has a value of one–half the cell width in the mesh. For magnetic inversions, the parameter σ is usually a value between 0.5 and 1.5 and for gravity inversion is of a constant value $\sigma = 1$. The value of $\tilde{\beta}$ above the denominator is typically equal to two. The effects of the value of $\tilde{\beta}$ on 3–D minimum–structure gravity inversions is studied in examples to follow.

3.3 Inversion Procedure: l_2 style

Inversion of a gravity data–set is complete when a density distribution $\mathbf{m}$ is found that minimizes ϕ_m and reproduces a data–set that satisfies the misfit ϕ_d within error

boundaries. To begin the inversion, the objective function of equation (39) is discretized for the mesh used. This leads to equation (41) being presented as,

$$\begin{aligned}\phi_m &= (\mathbf{m}-\mathbf{m}_0)^T\left(\mathbf{W}_s^T\mathbf{W}_s+\mathbf{W}_x^T\mathbf{W}_x+\mathbf{W}_y^T\mathbf{W}_y+\mathbf{W}_z^T\mathbf{W}_z\right)(\mathbf{m}-\mathbf{m}_0)\\ &= (\mathbf{m}-\mathbf{m}_0)^T\left(\mathbf{W}_m^T\mathbf{W}_m\right)(\mathbf{m}-\mathbf{m}_0)\\ &= \|\mathbf{W}_m(\mathbf{m}-\mathbf{m}_0)\|_2^2\end{aligned} \tag{44}$$

Here, $\mathbf{m}$ and $\mathbf{m}_0$ are vectors of length M and $\mathbf{W}_m$ is a diagonal matrix that is constructed from the coefficients and weighting functions discussed in Section 3.2.2.

Optimization is done by use of a proper minimization technique. Since the elements in equation (39) exhibit a sum of squares nature, a Gauss-Newton method is favoured. The derivative of equation (39), with respect to the coefficients, is taken and set equal to zero. The derivatives of the data misfit and model structure functions are obtained by application of a Taylor series expansion about a parameter vector $\mathbf{m}^n$ at the nth iteration. The expanded model objective gives,

$$\phi_m\left(\mathbf{m}^n+\delta\mathbf{m}\right) = \|\mathbf{W}_m\delta\mathbf{m}+\mathbf{W}_m(\mathbf{m}^n-\mathbf{m}_0)\|^2 \tag{45}$$

Applying a similar Taylor series expansion to the data misfit function about the parameter vector $\mathbf{m}^n$ yields,

$$\phi_d\left(\mathbf{m}^n+\delta\mathbf{m}\right) = \left\|\mathbf{W}_d\mathbf{J}\delta\mathbf{m}+\mathbf{W}_d(\mathbf{d}-\mathbf{d}^{obs})\right\|^2, \tag{46}$$

where $\mathbf{J}$ is the Jacobian sensitivity matrix. If a Gauss Newton mininization process is used to minimize the objective function, equations (45) and (46) are rearranged to produce the following (Farquharson, 2008),

$$\begin{aligned}&\left[\mathbf{J}^T\mathbf{W}^T\mathbf{W}_d\mathbf{J}+\beta\sum_k\mathbf{W}_k^T\mathbf{W}_k\right]\delta\mathbf{m}\\ =&\mathbf{J}^T\mathbf{W}_d^T\mathbf{W}_d\left(\mathbf{d}^{obs}-\mathbf{d}(\mathbf{m}^n)\right)\\ &+\beta\sum_k\mathbf{W}_k^T\mathbf{W}_k\left(\mathbf{m}_k^{rcf}-\mathbf{m}_0\right).\end{aligned} \tag{47}$$

By application of equation (47), a $\delta\mathbf{m}$ vector is obtained and is added to the starting model to produce a density vector $\mathbf{m} = \delta\mathbf{m}+\mathbf{m}_0$ that adequately reproduces the observed data and minimizes the objective function. This 'l_2' style of inversion is a linear inverse problem and requires only one iteration to complete.

In typical l_2 style minimum–structure inversion algorithm, the measure of model structure is given by four terms in a 3–D model. Usually, the first term incorporates a diagonal weighting matrix and a reference model. The three other terms incorporate the finite differences in the x–, y– and z–directions.

The l_2 style inversion is advantageous as minimization is preformed using a linear system of equations. It is also efficient in fitting the data, as long as the noise follows a Gaussian distribution. The smooth, fuzzy image produced by the l_2 style inversion is directly attributed to squaring the vectors in the model norms. This means that large-valued elements differ greatly from the norm. The minimization procedure forces a resulting vector that has no large, distinct elements. This is due to the nature of the inversion minimization, which rules out single large discrepancies. In the model minimization, l_2 minimizations spread the changes in density gradually over a number of adjacent cells, thus avoiding an abrupt change of density between adjacent cells.

3.4 Inversion procedure: l_1 style

Most minimum–structure inversion procedures follow the method of the l_2 style inversions presented in the previous section. This inversion style has been proven to successfully image the subsurface for potential field geophysical methods and are typically considered robust and reliable. This method of inversion uses a sum–of–squares measure for model structure and thus inversion results generally exhibit a smeared, fuzzy and smooth density model.

However, the actual subsurface is expected to certain sharp, uniform geologic interfaces, and so inversions which produce density models displaying these characteristics

are desired. In one attempt,Last and Kubik (1983) present a iterative technique that imposes a volume constraint on the anomalous body of the model produced. Portniguine and Zhadov (1999) introduce a method to produce sharp interfaces in inversions based on minimum gradient support functionals, which minimize the area where strong model parameter variations and discontinuity occur. However, the most common technique has typically been done by implementing an iteratively re–weighted least–squares algorithm. This method, known as an l_1 style inversion (Farqharson and Oldenburg, 1998; Loke et al., 2003; Farquharson and Oldenburg, 2003) produces models with sharp interfaces while using an analogous method to l_2 style minimum–structure inversions.

Minimization of l_1 style inversions is similar to the methodology used for l_2 style inversions, however the process is completed over a number of iterations by application of a technique known as iteratively re–weighted least squares (IRLS). In this case, the objective function is redefined as

$$\Phi^n = \phi_d^n + \beta^n \phi_m^n, \tag{48}$$

where n refers to the number of iterations. More importantly, the model objective function is defined as,

$$\phi_m = \|\mathbf{W}_m(\mathbf{m} - \mathbf{m}_0)\| \tag{49}$$

Since equation (49) lacks the squared element seen in equation (44), a sum of squares measurement procedure can not be executed for minimization. As in l_2 style inversions, the objective function of equation (48) is differentiated with respect to the coefficients and equalled to zero. The derivative of the data misfit remains as seen in equation (46) and differentiating the model measure for a parameter vector $\mathbf{x}$ results in (Farqharson and Oldenburg, 1998),

$$\frac{\partial \phi(\mathbf{x})}{\partial \delta m_k} = \sum \int_j \rho(x_j) \frac{\partial x_j}{\partial \delta m_k}, \tag{50}$$

where, in a perturbed l_p-norm measure of Ekblom (Farqharson and Oldenburg, 1998), ρ

is equal to,

$$\rho(x) = \left(x^2 + \varepsilon^2\right)^{p/2}, \tag{51}$$

where the constant ε is a small number and included to avoid calculatory errors should $x_i = 0$. In cases where $x_i \neq 0$, ε is considered negligible. A discreet form of equation (50)yields,

$$\frac{\partial \phi(\mathbf{x})}{\partial \delta \mathbf{m}} = \mathbf{B}^T \mathbf{q}, \tag{52}$$

where $\partial\phi/\partial\delta\mathbf{m} = (\partial\phi/\partial\delta m_1, \ldots, \partial\phi/\partial m_N)^T$, $B_{ij} = \partial x_i/\partial\delta m_j$, and $q = (\rho'(p_1), \ldots, \rho'(x_N))^T$. In a discreet notation, a diagonal matrix $\mathbf{R}$ is incorporated into equation (52) to yield,

$$\frac{\partial \phi(\mathbf{x})}{\partial \delta \mathbf{m}} = \mathbf{B}^T \mathbf{R} \mathbf{x}, \tag{53}$$

where,

$$\mathbf{R} = \begin{pmatrix} \frac{\rho(x_1)}{x_1} & 0 & \cdots & 0 \\ 0 & \frac{\rho(x_2)}{x_2} & \cdots & 0 \\ \vdots & \vdots & \ddots & \vdots \\ 0 & 0 & \cdots & \frac{\rho(x_N)}{x_N} \end{pmatrix}.$$

The value of ρ in equation (51) means the elements of $\mathbf{R}$ are,

$$R_{ii} = p\left(x_i^2 + \varepsilon^2\right)^{p/2-1}. \tag{54}$$

Here $p = 2$ for l_2 style inversions and $p = 1$ for l_1 style inversions. The minimization of equation (48) thus involves solving the following linear system of equations at each iteration,

$$\begin{aligned} &\left[\mathbf{J}^T \mathbf{W}_d^T \mathbf{R}_d \mathbf{W}_d \mathbf{J} + \beta \sum_k \alpha_k \mathbf{W}_k^T \mathbf{R}_k \mathbf{W}_k\right] \delta \mathbf{m} \\ &= \mathbf{J}^T \mathbf{W}_d^T \mathbf{R}_d \mathbf{W}_d \left(\mathbf{d}^{obs} - \mathbf{d}^{n-1}\right) \\ &\quad + \beta \sum_k \mathbf{W}_k^T \mathbf{R}_k \mathbf{W}_k \left(\mathbf{m}_k^{ref} - \mathbf{m}^{n-1}\right) \end{aligned} \tag{55}$$

Here, the matrices $\mathbf{R}$ are dependent on the model and recalculated after each iteration. The values of the products involving the Jacobian vector or its transpose are calculated using a pseudo forward modeling process, performed by solving the right–hand side of the forward problem (See Chapter 2). The solution of equation (55) is obtained iteratively by incomplete LU decomposition preconditioned conjugate gradients (Farquharson, 2008). The results provided by the l_1 style of minimization exhibit sharp interfaces between regions of differing densities and are considered to better represent the density distribution in the subsurface due to their block–like nature.

3.5 Inversion Elements

To perform minimum–structure inversions of borehole gravity data, the program *g3dfd* written by Farquharson is used. To run, the program requires a number of input files that specify the parameters of the subsurface of the area of interest. The code is able to generate l_2 or l_1 style inversions, incorporate contributions from horizontal, vertical and diagonal differences, and it incorporates a forward modeller which solves a finite difference approximation to Poisson's equation. The program *g3dfd* references an input file *g3dfd.in*. The contents of an example *g3dfd.in* file are seen in Figure 6 and a description of the entries in the input file are discussed below.

```
GRAV3D                          ! Format of input and output files.
borehole                        ! Root for filenames for output
Res_Bouguer.grv                 ! Observations file.
mesh10x10x5.txt                 ! Mesh file.
zerohspace_10x10x5.mod          ! Starting model.
DEFAULT                         ! Reference model (DEFAULT means use starting model).
none                            ! RM_267.wsExtra model weights for smallest component.
DEFAULT                         ! Topography information (DEFAULT means flat z=0 surface).
DEFAULT                         ! Active cells information (not used at the moment).
DEFAULT                         ! Distance weighting parameters (DEFAULT means beta=2, znot=1/4 smallest cell).
DEFAULT                         ! Huber parameter (DEFAULT means 1000.)
DEFAULT                         ! Ekblom parameters (DEFULT means 12 stuff)
DEFAULT                         ! Coefficients in the model measure (DEFAULT means 0,1,1,1,0,.. )
0.0000035  0.0000035   0.9 ! Starting and final trade-off parameters, and factor for decrease
1                               ! Maximum number of iterations in the inversion
1.0E-03                         ! Small number for inversion convergence tests
200   1.0E-20  1.0E-20  20  0.     ! Solver parameters for GN inversion solver
500    0.      1.0E-40  20  0.     ! Solver parameters for forward/sensitivity solver
```

Figure 6. The *g3dfd.in* input file. The contents of the file control parameters and reference elements necessary for executing the *g3dfd* minimum–structure inversion program.

3.5.1 Mesh File

To discretize the earth in rectangular cells, it is necessary that a mesh file is created that provides the boundaries of the subsurface and also defines the dimensions of each cell. The file, a generic text file, is referred to on line four in Figure 6 seen as mesh$10x10x5.\ txt$. This file has the following structure,

nE	nN	nV	
E_0	N_0	V_0	
ΔE_1	ΔE_2	...	ΔE_{nE}
ΔN_1	ΔN_1	...	ΔN_{nN}
ΔV_1	ΔV_1	...	ΔV_{nV}

where nE, nN and nV are the number of cells in the easting, northing and vertical directions respectively and E_0, N_0 and V_0 are the coordinates of the southwest top corner of the mesh. The cell widths in the easting direction traveling from west to east are given by $(E_1 : E_{nE})$. Cell widths in the northing direction traveling from south to north are given by $(N_1 : N_{nN})$. Cell widths in the vertical direction traveling from top to bottom are given by $(V_1 : V_{nV})$. The mesh file configuration is analogous to that used by the GRAV3D (2007) format.

Typically, the mesh is designed to represent an area of the subsurface which is directly beneath the area of observed data. Cells of different dimensions can be used in the mesh to obtain an increased number of cells where there may be particular areas of interest or where there is an increased amount of data. A region of larger cells outside of a core set of smaller cells is referred to as a 'padding zone'.

3.5.2 Topography

Topography is an optional file that is input depending on wether there is information about the surface topography of the surveyed area. The topography file is input on line eight in Figure 6. If marked as *DEFAULT*, this line denotes that the gravity measurements were taken on a flat surface ($z = 0$). The configuration of the topography

file is,

$$\begin{array}{|lll|}
\hline
n & & \\
E_1 & N_1 & ELEV_1 \\
E_2 & N_2 & ELEV_2 \\
\vdots & \vdots & \vdots \\
E_n & N_n & ELEV_n \\
\hline
\end{array}$$

where n is the number of topographic data points and E_i, N_i and $ELEV_i$ provide the easting, northing and elevation coordinates for the ith point. The elevation must have the same reference height as the values of V_0 in the mesh file. The topographic surface value above each column of cells is found by direct triangulation interpolation of the input topographic data (GRAV3D, 2007).

3.5.3 Observation File

The observation file name is given on line three of the input file. In Figure 6 the filename is *Res_Bouguer.grv*. The file contents include the calculated gravity measurement, its error and coordinates. The observation file has the following structure,

$$\begin{array}{|lllll|}
\hline
n & & & & \\
E_1 & N_1 & V_1 & G_1 & \sigma_1 \\
E_2 & N_2 & V_2 & G_2 & \sigma_2 \\
\vdots & \vdots & \vdots & \vdots & \vdots \\
E_n & N_n & V_n & G_n & \sigma_n \\
\hline
\end{array}$$

where n is the number of data points. The coordinate for the ith observation is given by (E_i, N_i, V_i) with the corresponding gravity measurement G_i and its accompanying estimated error σ_i. The gravity values input into the observation file have been subjected to all necessary corrections outlined in Chapter 1.

3.5.4 Initial Model

Another file required for inversion is the starting model read on line five of the input file. In Figure 6 this is file *zerohspace_10x10x5.mod*. This file contains $\mathbf{m}_0$ referred to

in equation (41). The file is essentially organized as a vector with density elements and its length is equal to the number of cells in the mesh. It is organized similar to the GRAV3D (2007) format as,

$$\begin{bmatrix} \rho_{1,1,1} \\ \vdots \\ \rho_{1,1,nV} \\ \rho_{1,2,1} \\ \vdots \\ \rho_{i,j,k} \\ \vdots \\ \rho_{nN,nE,nV} \end{bmatrix}.$$

Here the density $\rho_{i,j,k}$ is the starting density for the cell located at coordinate $[i, j, k]$. The first element of the file corresponds to the density in the top–south–west corner of the mesh. The vector is arranged in a specific order so that k changes the quickest (from 1 to nV), followed by j (from 1 to nE), then followed by i (from 1 to nN). If the inversion incorporates a topography file, any density value above the topographic surface is ignored. Other files that are arranged in a similar vector structure include a *reference model file* entered on line six of the input file (Figure 6) (note: a DEFAULT in this field means the starting model is used as the reference model) and an *extra model weighting file* entered on line four of the input file (Figure 6). The reference model allows the user to input specific constraints on the density that force the inversion to allocate certain density values to corresponding cells. An extra model weighting file can be added to increase or decrease the weighting implications for individual cells.

3.5.5 Input Parameters

The *g3dfd.in* input file allows the user to control the type of inversion. Input on line twelve implements whether an l_1 or l_2 style inversion is performed and the number indicated on line fifteen informs the number of iterations performed for an l_1 style inversion.

Inversion results that utilize either vertical, horizontal or diagonal differences in the model structure are obtained through customization of fourteen terms to values of either 0 or 1 on line thirteen of the input file (Figure 6).

The parameters of the distance weighting function, β and R_0 seen in equation (43) are specified on line ten. The starting and final trade–off parameters, which control the limits of the data misfit, are specified on line fourteen, and various forward solver parameters can be set the input file.

Setting aside the various available options with the *g3dfd* inversion code, the files needed to execute the program are: a mesh file, an observation file containing values of $\mathbf{d}^{obs}$ (see equation (40)), a reference model which contains values of $\mathbf{m}_0$ (equation (44)) and the input file *g3dfd.in* which references all files and incorporates inversion and forward modelling parameters. The code is run by executing the executable *g3dfd* in a unix terminal with a Fortran 95 compiler.

When complete, the program produced files include: a model density file, a predicted data–set file, and a output file. The model density file which has the name *filename. mod*, where *filename* is specified on line 2 of the input file, has the same structure as the starting model file and is able to be viewed with a corresponding mesh using UBC–GIF's visualization program MeshTools3D. The predicted data–set file, output as *filename. prd*, has the same format as the observation file with contents that include the observation locations and gravity data values obtained by forward solving the density model. The program also produces a *g3dfd.out* file which includes information about the data misfit ϕ_d, model structure ϕ_m, trade–off parameter β, and overall misfit Φ for each iteration.

CHAPTER 4

Cube–in–a–halfspace Inversion Examples

In the following chapter, examples of completed inversions are analyzed. The inversions are performed using the forward modelling and minimum–structure inversion procedures discussed in Chapters 2 & 3. The results presented are inversions of synthetic data derived from surface and borehole gravity data for a block–in–a–halfspace model. Both l_2 and l_1 style inversions are executed for scenarios with various locations and numbers of borehole and surface gravity data. Only a select few of the multiple inversion scenarios executed are presented here, for a full library of results please refer to Appendix A. The predicted data and observed data plots are shown only for a select few examples due to the redundancy of the plots. For every example examined, the predicted data match the observed data within a measure of error.

To obtain the observed data input into an inversion, synthetic data is calculated by forward modelling methods at observation locations around a particular density model. The mesh used in the block density model and for all inversions has dimen-

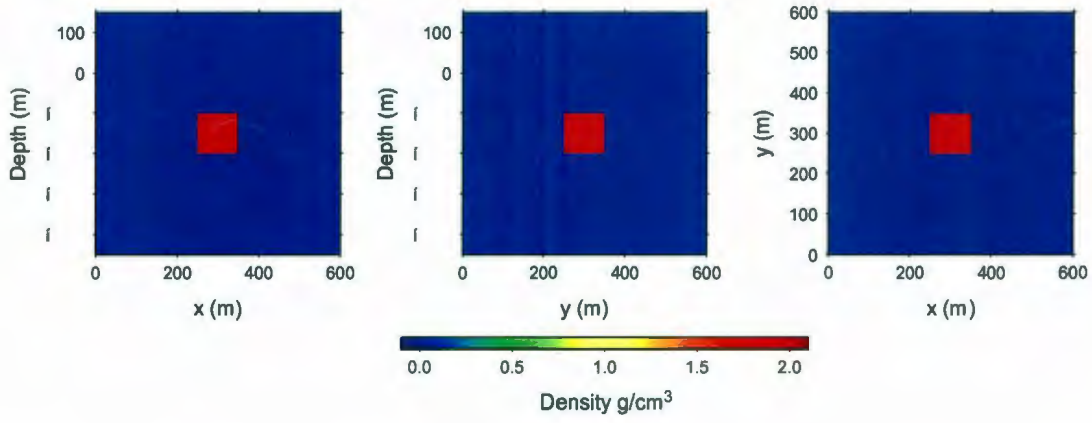

Figure 7. The mesh and block in a half–space model used for the inversion examples.

sions $(x, y, z) \rightarrow (0, 0, 150) : (600, 600, -450)$ and cell sizes of 10m in each direction. The mesh therefore contains 216,000 cells. A cube with a density of 2.0 g/cm^3 is located at the center of the mesh with coordinates, $(x, y, z) \rightarrow (250, 250, -100) : (350, 350, -200)$. The cells outside of the cube have a density of zero. The block density model is shown in Figure 7. The contrasting density values of 2.0 g/cm^3 and zero are chosen to represent the difference in densities between a massive sulphide and surrounding host rocks. A similar density contrast is seen in the main Ovoid of Voisey's Bay Nickel Mine (refer to Ash, 2007).

Using this model and mesh setup, a number of different scenarios of borehole and surface data configurations are studied. All observed data–sets are synthetic in nature and were produced by the forward modelling method using the finite–difference solution to Poisson's equation detailed in Chapter 2. For all borehole data, observation points are taken along a borehole which travels from $(z) \rightarrow (-3.846 : -296.153)$ m. A total of thirty nine observations are taken at evenly spaced intervals along the length of the boreholes, therefore approximately every 7.7 m. Random Gaussian noise of standard deviation equal to five percent of the magnitude of the datum is added to all data–sets.

The inversions are performed using the default l_2 norm of model structure and x, y and z first-order finite–difference terms with $\alpha_1 = 0$, $\alpha_2 = \alpha_3 = \alpha_4 = 1$, and $\alpha_5 = \cdots = \alpha_{14} = 0$ (Section 3.5.5). The distance weighting parameters are set to default with $\tilde{\beta} = 2$ and $z_0 = 2.5$ m (a quarter of the smallest cell dimension) (Section 3.2.3). The inversions are performed with a value of β that reproduces a data misfit value ϕ_d that equals the total number of data points within a 10% error margin. The inversion results are presented in an x–, y– and z–slice taken from the produced density model. The x–slice displays the xz plane at $y = 300$; the y–slice displays the yz plane at $x = 300$ and the z–slice displays the xy plane taken at $z = -150$. The goal of each example is for the inversion to reproduce a density model that correlates well with the

structure and density distribution of the true cube model in Figure 7.

4.1 Two Boreholes

The first scenario examined for the block–in–a–halfspace model is a minimum–structure inversion of data from two boreholes. With thirty-nine observations measured along each borehole, there is a total of 79 data points. The first borehole is located at $(x, y) \rightarrow (150, 300)$ and the second is located at $(x, y) \rightarrow (450, 300)$, both symmetrically located at a distance of 150 m along the x-axis. Figure 8 shows the returned density distribution from the inversion with the borehole locations seen in white and the outline of the original model in black.

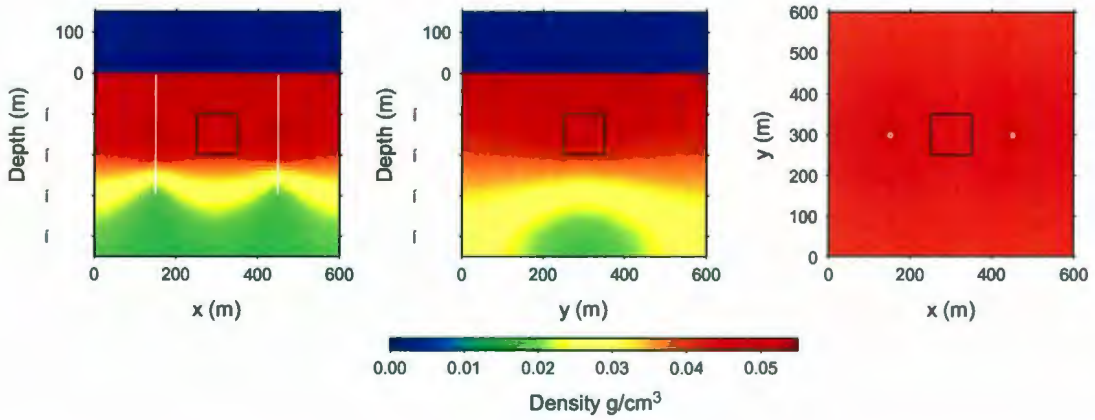

Figure 8. Inversion results for a block–in–a–halfspace of gravity data from two boreholes. *left*: the x–slice, *middle*: the y–slice; *right*: the z–slice. Borehole locations are displayed in white. The true block model is outlined in black.

The results presented in Figure 8 exemplify a poor inversion result as the structure and recovered densities significantly differ from those of the true model. From the two sets of borehole data, the inversion is able to produce a density distribution with an appropriate depth as it allocates its peak densities to cells at at approximately $z \rightarrow (-100 : -200)$ seen in Figure 8 *left*. The density model, however, does not possess any spatial resolution in the x and y plane compared to the true model. The lack of spatial

resolution can be attributed to the fact that the boreholes are of identical distance from the center of mass in the symmetric true model and results in two identical gravity data–sets. Inversion examples using two non–symmetrical borehole datasets are examined in Appendix A. With the limited information from two symmetrical data–sets, the inversion interprets this as a large plane or sheet of low density which spans the entire xy plane of the mesh at approximately the correct depth as seen in Figure 8 *right.* Upon completion, the inversion parameters are as follows:

- $\rho_{max} = 0.0535$
- $\rho_{min} = 0.0$
- $\beta = 0.25000E-03$
- $\phi_d = 82.575$
- $\phi_m = 0.27860E+06$
- $\Phi = 152.23$

4.2 Three Boreholes

The next situation examined further continues the investigation of the previous example in hopes of producing a density model which appropriately corresponds to the true model. A third borehole data–set is included in the inversion through the center of the dense block located at $(x, y) \rightarrow (300, 300)$. The inversion result is seen in Figure 9.

By adding an extra borehole data–set through the center of the dense block, the density model displays a greatly improved representation of the true model. The outcome model is a fuzzy and smeared image typical of the l_2 style inversion. The role of the central borehole provides precise information on the depth of the density boundaries and recreates a strong density contrast at depths $z = -100$ and $z = -200$. The data from the two outlying boreholes also serves a role by confining the gradual density spread away from the center of mass and reproducing a less smeared image. The influence of the two outlying boreholes is seen by comparing the density spread away from the central borehole of the inversion slices in Figure 9 *left* and *middle.* Figure 9 *right* also demonstrates this as the density decreases in value gradually over the cells in the

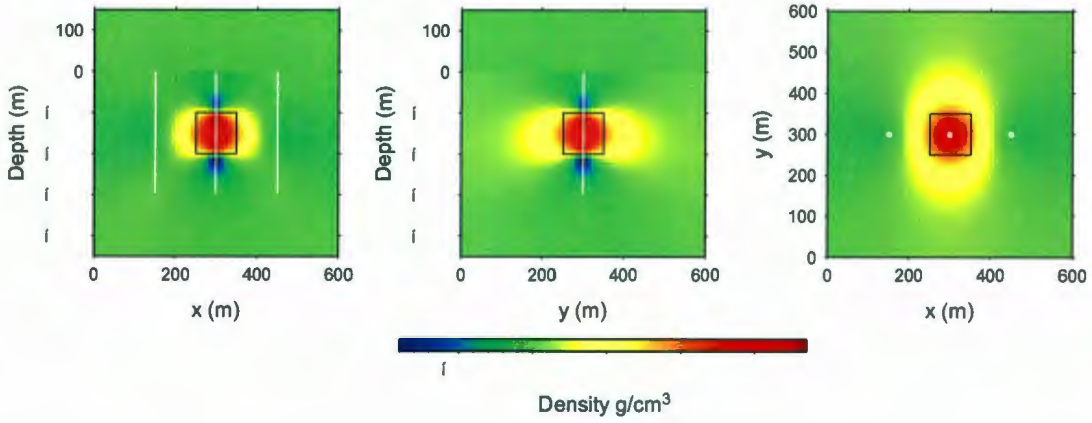

Figure 9. Inversion results for a block–in–a–halfspace from a line of three boreholes. *left*: the x–slice, *middle*: the y–slice; *right*: the z–slice. Borehole locations are displayed in white. The true block model is outlined in black.

y–direction. The density values diminish more abruptly over cells in the x–direction, which is confined by the outer borehole data.

The predicted and observed data for each borehole are plotted in Figure 10. Here, the observed data is represented by circles and the predicted data is plotted in red. The observed and predicted data match well, with the largest deviations occurring at the peak values. By examining the three plots in Figure 10, it is clear that the outer boreholes influence the inversion result by constraining low densities away from the central dense block. The magnitude of the gravity data–set in the middle borehole has peak density values greater than ten times that of the two outer boreholes. Therefore, in the recovered model, high density values surround the middle borehole and are lacking in cells which surround the outer boreholes.

A plot of the difference between the predicted data and the observed data is seen in Figure 11.

The main areas of difference in the borehole located at $(x, y) \rightarrow (300, 300)$ seen in Figure 11 *middle* occur at depths $(z) \rightarrow (-100)$ m and $(z) \rightarrow (-200)$ m. These large

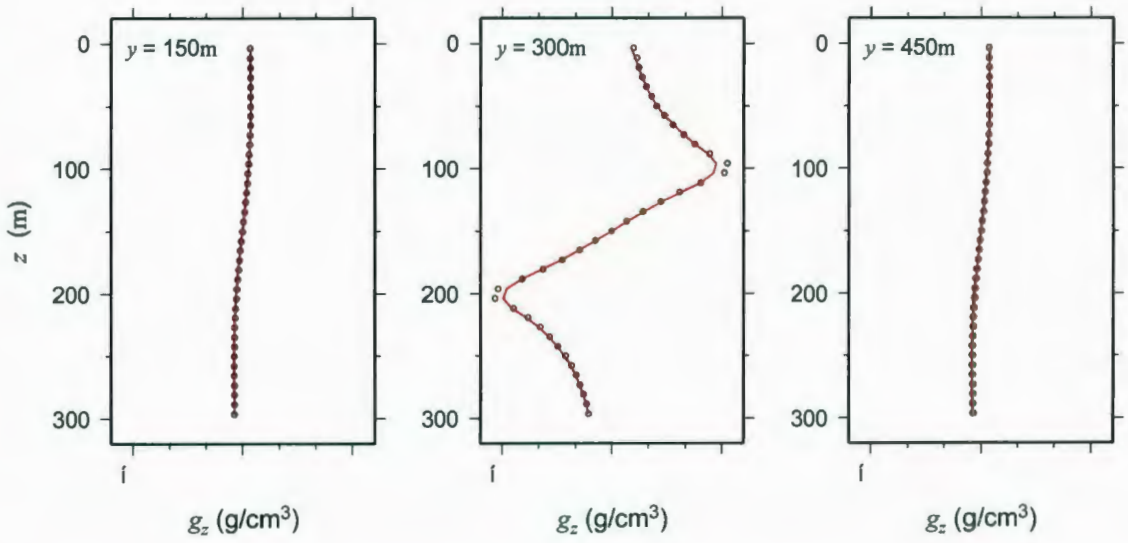

Figure 10. The observed data–set calculated for the block model shown in circles and the predicted data–set returned by the inversion plotted in red for varying borehole locations. *left*: $(x, y) \rightarrow (150, 300)$; *middle* $(x, y) \rightarrow (300, 300)$; *right*: $(x, y) \rightarrow (450, 300)$.

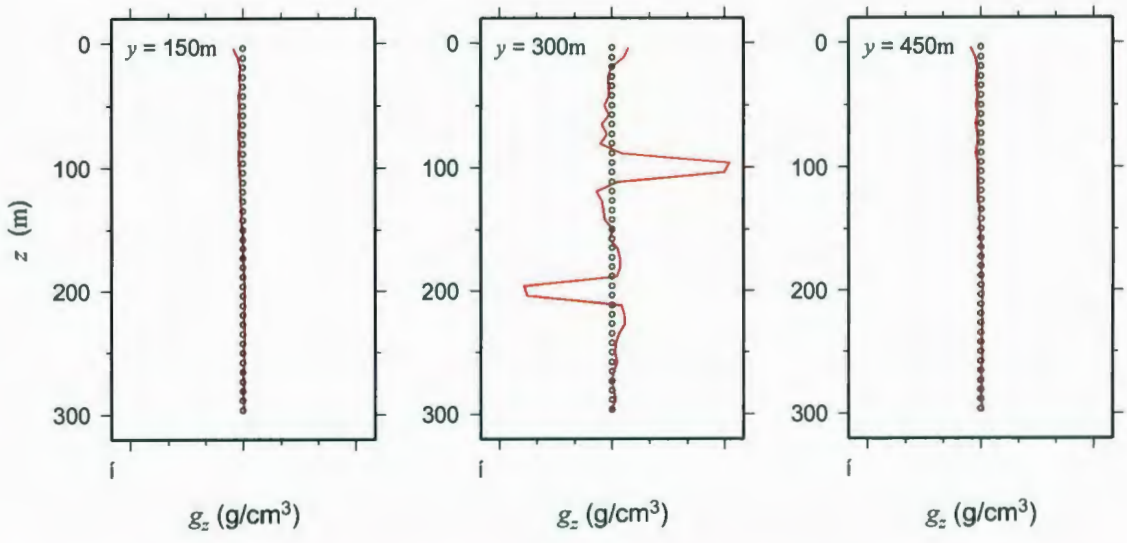

Figure 11. The errors in the gravity values computed by the inversion of the predicted data in red relative to the values of the observed data–set for the block model shown in circles for varying borehole locations. *left*: $(x, y) \rightarrow (150, 300)$; *middle* $(x, y) \rightarrow (300, 300)$; *right*: $(x, y) \rightarrow (450, 300)$.

differences correspond with the minimum and maximum gravity values for the data–set. The largest magnitude of difference for a single datum between the observed and predicted data is a value of 0.313 g/cm^3 for a gravity value of 3.16 g/cm^3 calculated at a depth of $z = -96.15$ m. Therefore resulting in a percentage error of 9.9%.

The data–sets for boreholes $(x, y) \rightarrow (150, 300)$ and $(x, y) \rightarrow (450, 300)$ are identical due to the symmetry of the block model. The maximum deviation between observed and predicted data–sets is a value of 0.0263 g/cm^3 for a gravity value of size 0.201 g/cm^3 occurring at a depth $z = -3.846$ m. This results in a percentage error of 13.1%. The output parameters of the completed inversion are,

- $\rho_{max} = 1.84\text{g/cm}^3$
- $\rho_{min} = -0.92\text{g/cm}^3$
- $\beta = 0.10E-05$
- $\phi_d = 125$
- $\phi_m = 0.944E+09$
- $\Phi = 1069$

The effects of the outer boreholes on restricting the spreading of the density anomaly is also seen in a three borehole simulation aligned in an "L" shape. The density distribution resulting from an inversion of gravity data from boreholes located at coordinates $(x, y) \rightarrow (150, 300)$, $(x, y) \rightarrow (300, 300)$ and $(x, y) \rightarrow (300, 150)$ is seen in Figure 12.

This example further exemplifies the influence that the additional boreholes bear on the inversion result. In Figure 12 *right* it is seen that without any confining borehole data on the top–right of the diagram, the l_2 style characteristically produces a fuzzy-smeared image where the density change between a cell and neighbouring cells is minimal. The output parameters from this inversion are as follows,

- $\rho_{max} = 1.73$ g/cm^3
- $\rho_{min} = -1.06$ g/cm^3
- $\beta = 0.10E-05$
- $\phi_d = 116.8$
- $\phi_m = 0.872E+09$
- $\Phi = 989$

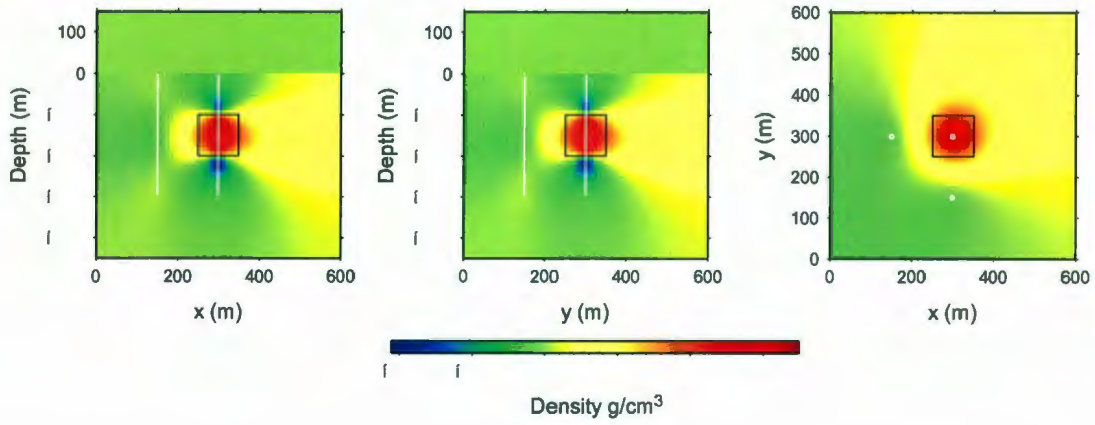

Figure 12. Inversion results for a block–in–a–halfspace from an "L" configuration of three boreholes. *left*: the x–slice, *middle*: the y–slice; *right*: the z–slice. Borehole locations are displayed in white. The true block model is outlined in black.

4.3 Surface Data

The next example is the result from a typical inversion performed with only surface gravity data. A total of 1521 data points are taken at the surface ($z = 0$), from $(x, y) \rightarrow (105.13, 105.13) : (494.87, 494.87)$ m, meaning measurements are calculated at approximately every 10.25 m. The density distribution produced from the inversion is seen in Figure 13. The observed data, predicted data and difference between the two are plotted in Figure 14.

The inversion result exemplifies a common problem associated with all surface gravity data inversions: a lack of depth resolution. Since the surface measurements do not carry any information regarding the possible depth of an anomaly, the nature of the inversion is to distribute density to cells closer to the surface or points of observation. This is caused by the natural decay of the kernel functions, for a more detailed explanation refer to Chapter 3. Because the density anomaly is spread out vertically, the peak density values in the produced model differ greatly from that of the true model. Also, due to the lack of depth resolution, the highly dense region corresponds poorly

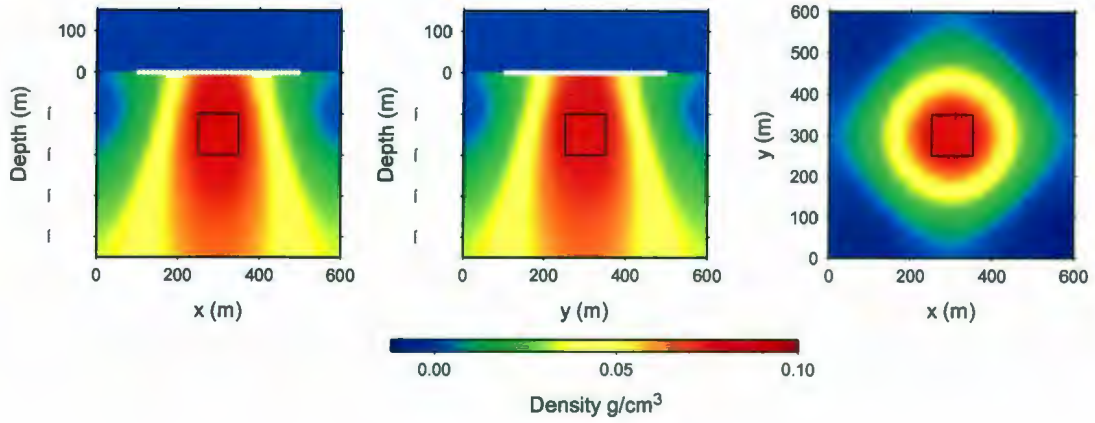

Figure 13. Inversion results for a block–in–a–halfspace from surface gravity data. *left*: the x–slice, *middle*: the y–slice; *right*: the z–slice. Borehole locations are displayed in white. The true block model is outlined in black.

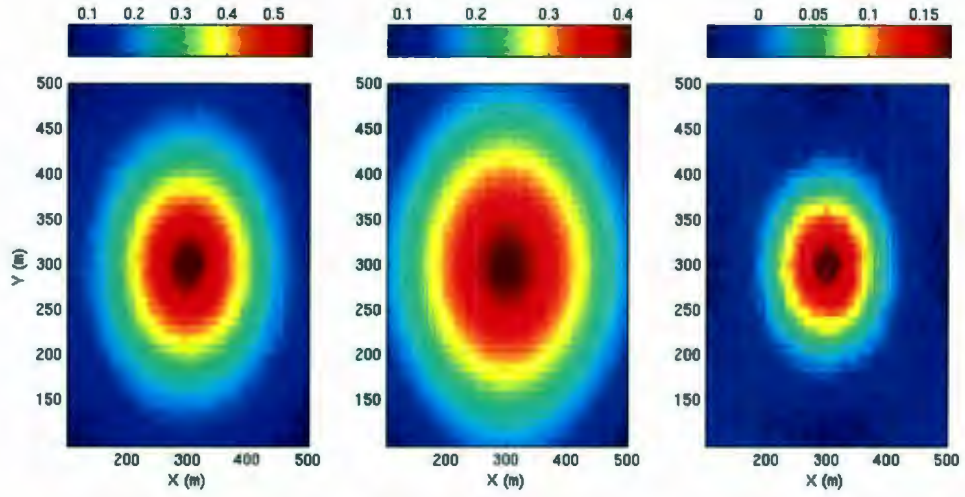

Figure 14. The observed surface data–set calculated for the block model the predicted surface data–set returned by the inversion, and a plot of the difference. *left*: the observed data–set; *middle* the predicted data–set; *right*: the difference between the observed and predicted data–sets.

with the shape of the true model in the x– and y– slices of Figure 13. Despite this, the inversion is able to localize the center of density in the z–slice, however the anomaly is characterized by a typical smeared–out fuzzy image and lack of resolution typical from l_2 style inversions. Upon completion of the inversion, the output parameters are as follows:

- $\rho_{max} = 0.092$ g/cm^3
- $\rho_{min} = -0.012$ g/cm^3
- $\beta = 0.270E-02$
- $\phi_d = 1508$
- $\phi_m = 0.671E+06$
- $\Phi = 3320$

4.4 One Borehole

In a comparative study, the inversion results from data calculated for one borehole traveling directly through the center of the dense cube is examined. Here, the borehole is located at $(x, y) \rightarrow (300, 300)$. The inversion results are seen in Figure 15.

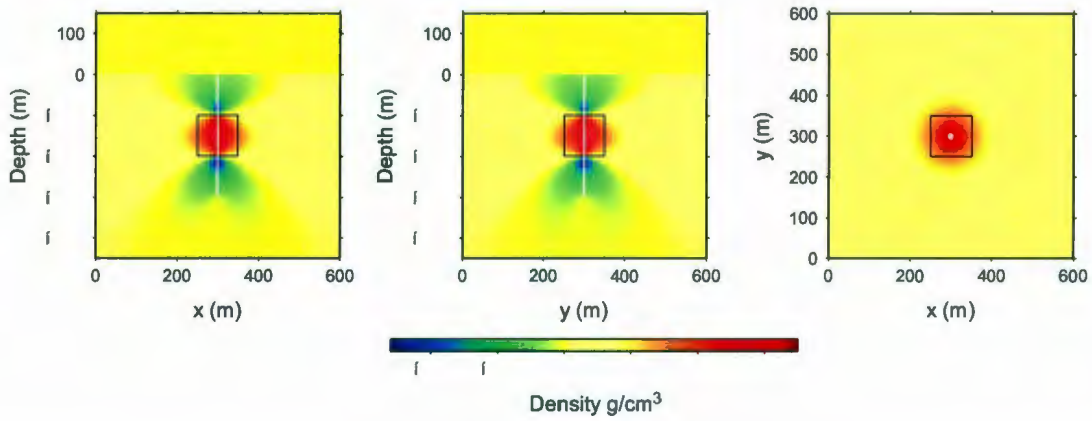

Figure 15. Inversion results for a block–in–a–halfspace of gravity data from one borehole located at $(x, y) \rightarrow (300, 300)$. *left*: the x–slice, *middle*: the y–slice; *right*: the z–slice. Borehole locations are displayed in white. The true block model is outlined in black.

Despite the minimal amount of input data, the inversion is able to reproduce a fairly accurate representation of the initial density model. The input of only one borehole is

able to accurately allocate high densities to the correct depth of the dense structure, however struggles with confining high density within the xy–plane. In the output model, the inversion does well to match the peak densities inside the anomalous block and for the zero density valued cells outside, however, negative densities are present in cells located directly above and below the borehole.

The generally good inversion obtained from the one borehole scenario in Figure 15 is most likely due to the ideal location of the borehole and the geometric symmetry and simplicity of the true model. With measurements being taken directly through the center of the anomalous mass, the largest gravity values appear at the top and bottom edge of the true model and are large in magnitude compared to gravity values taken along the remainder of the borehole. This results in a condensed distribution of density, which happens to fit the true model well in the xy plane due to the symmetry of a cubed true model and the general smeared image of the l_2 style inversion. In an l_1 style inversion, it is assumed that only the cells adjacent to the borehole between depths of -250 and -350 m would exhibit high density in the recovered model (picture of L1 one borehole model to come upon completion). The outcome parameters obtained from the l_2 inversion are,

- $\rho_{max} = 1.73$ g/cm^3
- $\rho_{min} = -1.28$ g/cm^3
- $\beta = 0.42000E-06$
- $\phi_d = 36.469$
- $\phi_m = 0.84904E+09$
- $\Phi = 393.06$

4.5 Surface Data, One Borehole

In the final example of this section, an inversion combining the surface gravity measurements from subsections 4.3 and 4.4 is examined. This inversion was performed in the hope of being able to recover the confined density resolution in the xy–plane displayed by the surface gravity inversion with the accurate depth resolution traits presented by

the single borehole inversion. The density distribution from the completed inversion is seen in Figure 16.

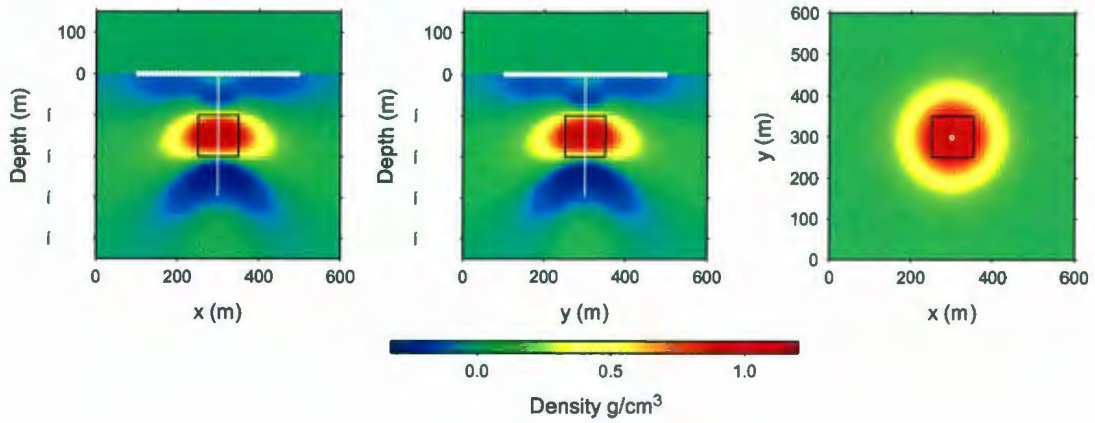

Figure 16. Inversion results for a block–in–a–halfspace from surface gravity data and data from one borehole. *left*: the x–slice, *middle*: the y–slice; *right*: the z–slice. Borehole locations are displayed in white. The true block model is outlined in black.

The inversion of surface and borehole gravity data does well to recreate the structure of the true model. The surface data locates the center of density of the true model in the xy–plane and limits the high density distribution close to the confines of the true model cube. The result is produces a less smeared image that falls mostly within the distinct boundaries of the true model. The inclusion of the borehole gravity data provides the necessary depth resolution needed in the surface data inversion example. However, inclusion of the surface gravity data also contributes in spreading the high density values to the edges of the true cube and away from the cells adjacent to the borehole present in the one borehole scenario. The use of both borehole and surface gravity data enables a better representation of the dense cube. In addition, the produced density distribution does well to mimic the density distribution outside of the true cube and allocates small magnitudes of density to those cells replicating the zero-halfspace background of the true model. The density values present in the produced model also correspond nicely with

the dense region of the true model. The parameters of the output inversion include,

- $\rho_{max} = 1.18$ g/cm^3
- $\rho_{min} = -0.322$ g/cm^3
- $\beta = 0.30500E-04$
- $\phi_d = 1549.9$
- $\phi_m = 0.12090E+09$
- $\Phi = 5237.3$

4.5.1 Surface Data, One Borehole l_1 inversion

Having obtained a reasonable result from inverting gravity data from a borehole and surface data, an l_1 style inversion was conducted with the same data–sets. The inversion ran 20 iterations with default Ekblom parameters of $p = 1$ and $\varepsilon = 10^{-4}$. The model was produced using only the horizontal and vertical finite–differences creating a piecewise constant or blocky model with interfaces only either horizontal or vertical. The resulting density model for the $20th$ iteration from this inversion is seen in Figure 17.

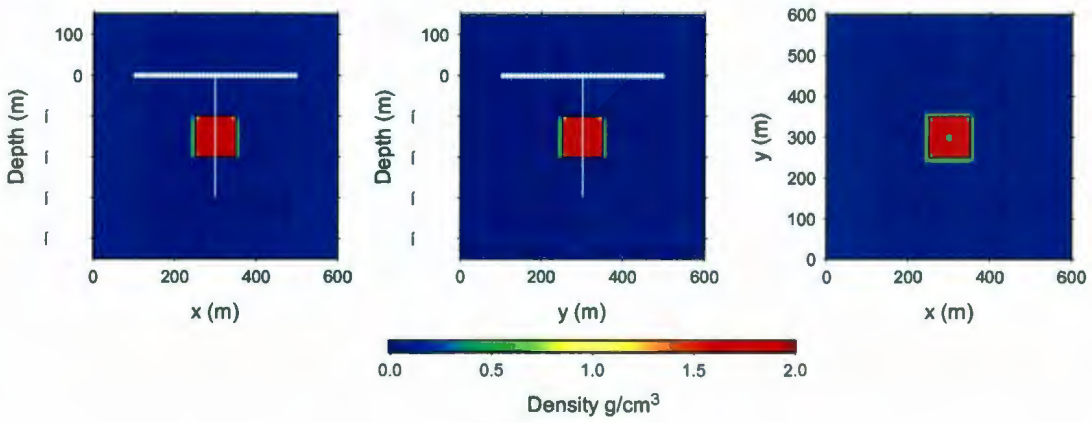

Figure 17. An l_1 style inversion result for a block–in–a–halfspace from a combined surface and one borehole gravity data. *left*: the x–slice, *middle*: the y–slice; *right*: the z–slice. Borehole locations are displayed in white. The true block model is outlined in black.

From the results of the l_1 inversion, it is examined that the inversion outcome model is almost analogous to the true model in location, shape and density contrasts.

The output parameters for the $20th$ iteration are,

- $\rho_{max} = 1.92$ g/cm^3
- $\rho_{min} = -0.00887$ g/cm^3
- $\beta = 0.25000E-02$
- $\phi_d = 17.270$
- $\phi_m = 0.10612E+07$
- $\Phi = 2670.3$

4.6 Summary

Inversions scenarios of gravity data for a block–in–a–halfspace model were presented throughout the Chapter and in Appendix A. These examples show that the ability for the produced model to recreate the density distribution of the true model depends on the locations and number of borehole and surface gravity data used in the inversion. Gravity data from boreholes located directly through the dense block produced the maximum gravitational peaks and thus, the produced density models display areas of high density where the borehole intersects the true block model. This is the case for all boreholes intersecting the block model including boreholes located on the edge of the model. Scenarios where boreholes were located away from the true block model produced, generally, a poorer recreation of the true density distribution. The produced models from theses examples displayed a more evenly distributed density profile across the domain of the mesh with moderate density peaks occurying at the center of mass at depth, however with no spatial resolution in the xy–plane.

Scenarios with boreholes located through the dense block and away from the dense block produced better density models. In these cases, the borehole located through the block produced an area of high density and the outer boreholes produced an area of lower density in the model. The boreholes located away from the density anomaly confined the high densities to the boundaries of the block creating a model which better resembled the density distribution of the true model.

Examples that used surface and borehole data in the inversion were also examined.

The inclusion of surface data was able to confine high densities with greater spatial resolution. The inclusion of borehole data with surface data was able to produce a density model with high densities at the correct depth. The use of borehole data to produce a model with correct depth solved a problem common to surface gravity data inversion, which is a lack of depth resolution.

Through the study of the examples, it is observed that the more borehole and surface data present in an inversion, the greater the produced model will represent the density distribution of the true model. Since an infinite number of data is not an option, the examples suggest that a borehole located directly through the center of an anomalous mass, plus additional boreholes surrounding the anomaly will produce an accurate density distribution. This setup sees that the central borehole will recreate an appropriate peak density, while the outer boreholes confine the high densities to the edges of the density anomaly.

CHAPTER 5

Wedge–in–a–halfspace Inversion Examples

In the following chapter, examples of completed inversions are analyzed. The inversions are performed using the forward modelling and minimum–structure inversion procedures discussed in Chapters 2 & 3. The results presented are inversions of synthetic data derived from surface and borehole gravity data for a wedge–in–a–halfspace model. Both l_2 and l_1 style inversions are executed for scenarios of varying locations and numbers of borehole and surface gravity data. Only a select few of the multiple inversion scenarios executed are presented here, for more inversion examples please refer to Appendix B. The predicted data and observed data plots are shown only for a select few examples due to the redundancy of the plots. For every example examined, the predicted data match the observed data within a measure of error.

With the previous set of inversions focused on recovering a simple and symmetric dense cuboid, the following inversion examples are aimed to recover a model that differs in symmetry. The base model from which simulated gravity values are calculated is a dense wedge in a halfspace. Similar to the previous block–in–a–halfspace examples, slices of the density models are displayed for an x–plane at $y = 300$, a y–plane at $x = 300$, and a z–plane at $z = -150$. The true model of the wedge–in–a–half space is shown in Figure 18.

The mesh and cell sizes are defined identically to the block–in–a–halfspace examples and the wedge model is essentially designed the same as the block model, however sliced in half. The density of the wedge is 2.0g/cm^3 and located in the center of the mesh. The y–coordinates of the wedge are $(y) \rightarrow (250 : 350)$. The x– and z– coordinates of the wedge decrease by 10m per cell, the x– and z–coordinate are $(x, z) \rightarrow (250, -100) : (350, -110)$ to $(x, z) \rightarrow (250, -100) : (350, -200)$. The cells outside of the wedge have a

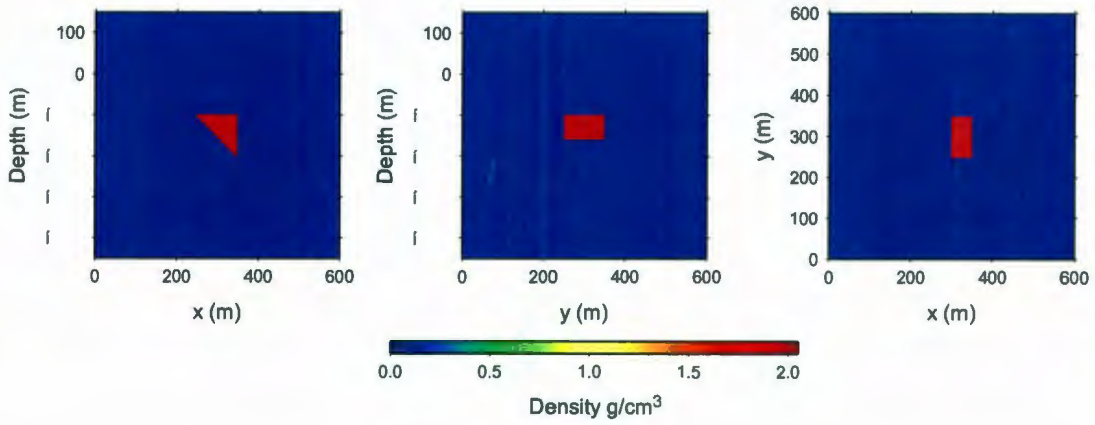

Figure 18. The mesh and wedge–in–a–halfspace model used for the inversion examples. *top*: the x–slice, *middle*: the y–slice; *bottom*: the z–slice. Borehole locations are displayed in white. The true wedge model is outlined in black.

background density of zero. The goal of each example is for the inversion to reproduce a density model that correlates well with the structure and density distribution of the true wedge model in Figure 18.

Using this model and mesh setup, a number of different scenarios of borehole and surface data configurations are studied. All observed data–sets are calculated synthetically and were produced by a forward modelling method that evaluates the finite–difference solution to Poisson's equation detailed in Chapter 2. All borehole data are calculated along boreholes which travel from $z \rightarrow (0 : -300\text{m})$. Thirty nine observations are taken at evenly spaced intervals at approximately 7.7m apart. Random Gaussian noise of standard deviation equal to five percent of the magnitude of the datum is added to all data–sets. The density models are produced using the default l_2 norm of model structure and x, y and z first-order finite–difference terms with $\alpha_1 = 0$, $\alpha_2 = \alpha_3 = \alpha_4 = 1$, and $\alpha_5 = \cdots = \alpha_{14} = 0$ (Section 3.5.5).

5.1 Five Boreholes

The first scenario examined for the wedge–in–a–halfspace model incorporates gravity data–sets from five different borehole locations. The borehole set up includes a central borehole traveling directly through the center of density at $(x, y) \rightarrow (300, 300)$, and four boreholes surrounding the model at locations $(x, y) \rightarrow (150, 300)$, $(x, y) \rightarrow (450, 300)$, $(x, y) \rightarrow (300, 150)$, $(x, y) \rightarrow (300, 450)$. The density distribution from the completed inversion is seen in Figure 19. The borehole data configuration was chosen in the hope of

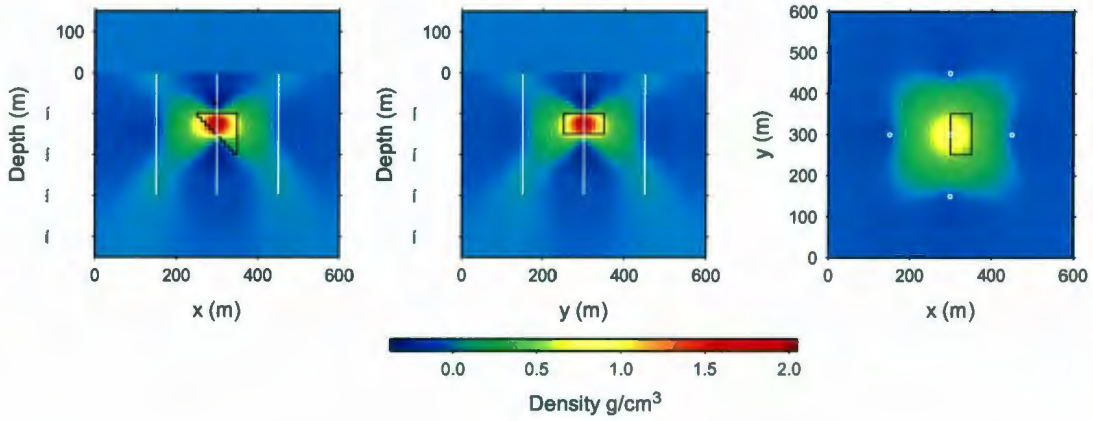

Figure 19. Inversion results for a wedge–in–a–halfspace of gravity data from five boreholes. *left*: the x–slice, *middle*: the y–slice; *right*: the z–slice. Borehole locations are displayed in white. The true wedge model is outlined in black.

obtaining a central density distribution with the outlying boreholes constraining the density to produce a wedge. The observed and predicted borehole data is seen in Figures 20 and 21

The resulting density model is poor in comparison with the true model. Despite the good representation of peak density values (2.04 compared to 2.0), structurally the resulting model differs greatly from the true model. The inversion model shows a concentration of high density around the middle borehole, located at $(x, y) \rightarrow (300, 300)$, between the depths -100 and -150 m. The outer boreholes surrounding the dense wedge

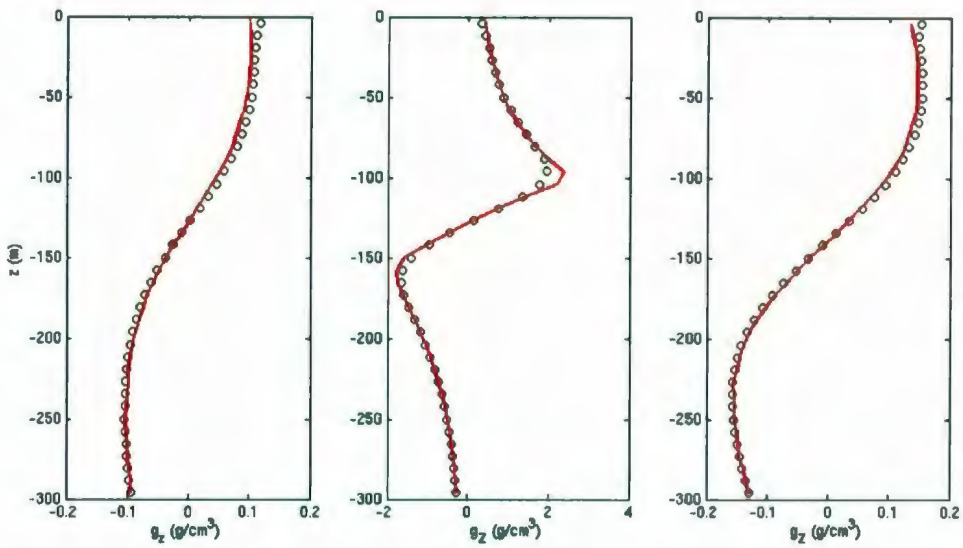

Figure 20. The observed data–set calculated from a wedge model shown in circles and the predicted data–set returned by the inversion plotted in red for varying borehole locations. *left*: $(x, y) \rightarrow (150, 300)$; *middle* $(x, y) \rightarrow (300, 300)$; *right*: $(x, y) \rightarrow (450, 300)$.

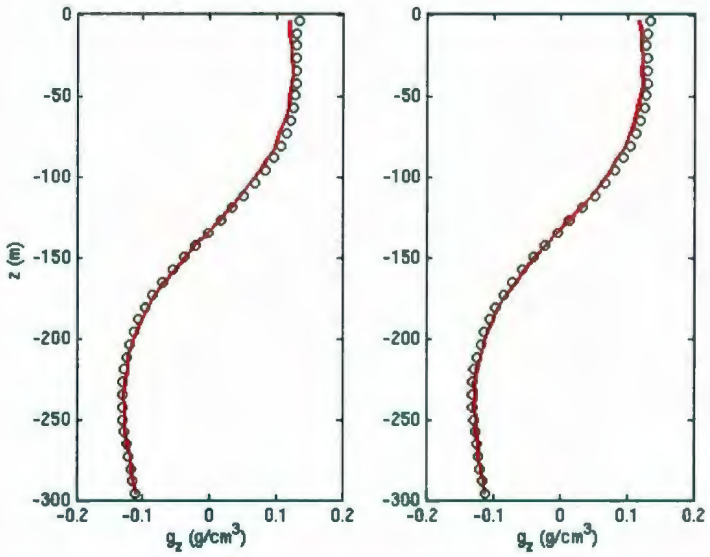

Figure 21. The observed data–set calculated from a wedge model shown in circles and the predicted data–set returned by the inversion plotted in red for varying borehole locations. *left*: $(x, y) \rightarrow (300, 150)$; *right*: $(x, y) \rightarrow (300, 450)$.

appear to have little influence on reproducing the high density values at the edges of the wedge. The output file from the inversion involved the following information.

- $\rho_{max} = 2.04$ g/cm^3
- $\rho_{min} = -0.375$ g/cm^3
- $\beta = 0.16500E-05$
- $\phi_d = 192.99$
- $\phi_m = 0.61609E+09$
- $\Phi = 1209.5$

5.2 Five Boreholes Edge

In an effort to obtain more of a wedge type structure from the inverted model using a similar five borehole scenario, the locations of the outer boreholes were moved so that they appear at the edge of the anomaly. The four outlying boreholes are relocated to $(x, y) \rightarrow (250, 300)$, $(x, y) \rightarrow (350, 300)$, $(x, y) \rightarrow (300, 250)$, and $(x, y) \rightarrow (300, 350)$, with the fifth borehole remaining in the center of the mesh at $(x, y) \rightarrow (300, 300)$. The resulting inverted model slices from this borehole arrangement are seen in Figure 22

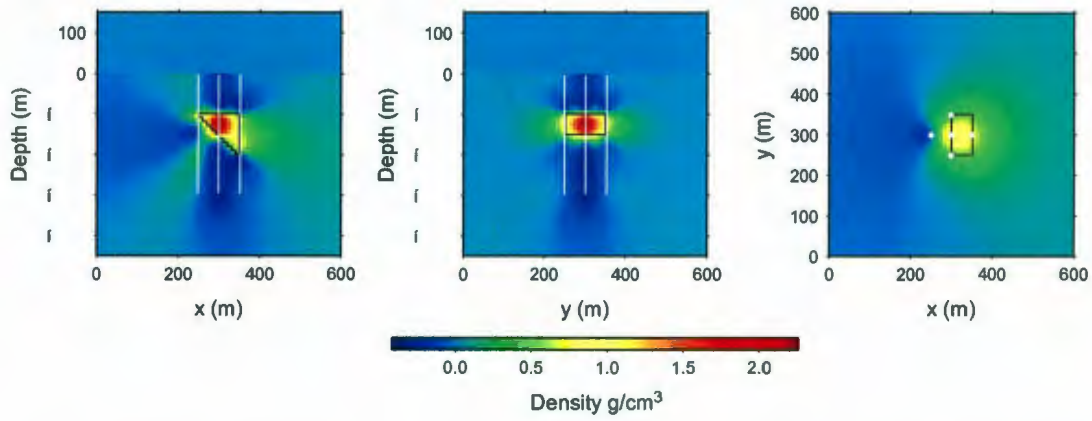

Figure 22. Inversion results for a wedge–in–a–halfspace of gravity data from five boreholes. *left*: the x–slice, *middle*: the y–slice; *right*: the z–slice. Borehole locations are displayed in white. The true wedge model is outlined in black.

By the inclusion of borehole data closer to the dense area, the inversion is able to reproduce a better structural representation of the true model. The density at the edges

of the wedge is of lesser magnitude than the center, however is still high in comparison to the density distribution outside of the wedge. The produced model still exhibits a smeared density distribution typical to l_2 style inversions, with the majority of the density spreading occurring around the borehole located at $(x, y) \rightarrow (350, 300)$. The predicted and observed data for boreholes located at $(x, y) \rightarrow (250, 300)$, $(300, 300)$, $(350, 300)$ are plotted in Figure 23. The observed data is represented by circles and the predicted data is plotted in red. A plot of the differing values between the predicted data with respect to the observed data is seen in Figure 24.

The correlation between the predicted and observed data in Figure 23 *left* match well with a peak gravity value occurring at a depth of $z = -96$ m, the last measurement location before passing through the dense wedge. The negative density peak occurs at a depth of $z = -173$ m. This depth, approximately 60 m away from where the borehole exited the dense wedge, is where the wedge density has the greatest impact on gravity measurement after the initial peak. The curve of the plot reflects the asymmetrical shape of the wedge with sudden and sharp increase in gravity values near the upper surface, and the more gradual, less abrupt change in gravity values below the lower surface. Out of the 39 observations, 15 are positive gravity values and 24 are negative. The error between the observed and predicted data is seen in Figure 24 *left* and the greatest difference between observed and predicted data has a value of 0.18 g/cm^3. This error accompanies a gravity value of 0.043 g/cm^3 and occurs at a depth $z = -111$ m. This results in a percentage error of 416 %. The large percent error is due to the data being close to zero and near a cross-over point, as the next largest percentage error between the two data–sets is 13 %.

The central borehole curve in Figure 23 *middle* follows a similar trend, however the difference in magnitude between the positive and negative peaks is not as large. The negative peak occurs at $z = -157$ m and the surrounding gravity values differ less

drastically compared to those around the positive peak. Out of the 39 gravity values measurement, the first 17 are positive and the remaining 22 are negative. The differences between data–sets is plotted in Figure 24 *middle*. The largest deviation has a value of 0.315 g/cm^3 at a depth of $z = -96.2$ m and corresponds to a datum equal to 2.38 g/cm^3. The resulting percentage error is 13%.

A plot of the data–set traveling along borehole located at $(x, y) \rightarrow (350, 300)$ in Figure 23 *right* produces density peaks similar to the data plot seen in Figure 10 *middle* with peaks occurring at depths corresponding to the boundaries of the dense wedge in the true model. The curve, however, exhibits a non–symmetric shape, which is due to the non–symmetry of the wedge model. Here, 18 of the total gravity values are positives and 21 are negative. The error between data–sets is plotted in Figure 24 *right*. The highest magnitude of error has a value of 0.11 g/cm^3 for a gravity value of size 1.48 g/cm^3 and occurs at a depth $z = -104$ m. This results in a percentage error of 7%.

The data–sets from the boreholes located at $(x, y) \rightarrow (300, 250)$ and $(300, 350)$ are not shown as they have a similar data trend as Figure 10 *middle*, however exhibiting data with lower overall magnitude.

The output file parameters from the inversion are as follows.

- $\rho_{max} = 2.25$ g/cm^3
- $\rho_{min} = -0.418$ g/cm^3
- $\beta = 0.12000E - 05$
- $\phi_d = 214.33$
- $\phi_m = 0.77041E + 09$
- $\Phi = 1138.8$

5.2.1 Five Boreholes Edge l_1 style

Since inverting gravity data from five boreholes produces a model with some features of a dense wedge, a model which contains less of a smeared density distribution is sought. An l_1 style inversion with gravity data–sets from the same boreholes was performed in hopes of obtaining a model that exhibits sharp and distinct interfaces between densities.

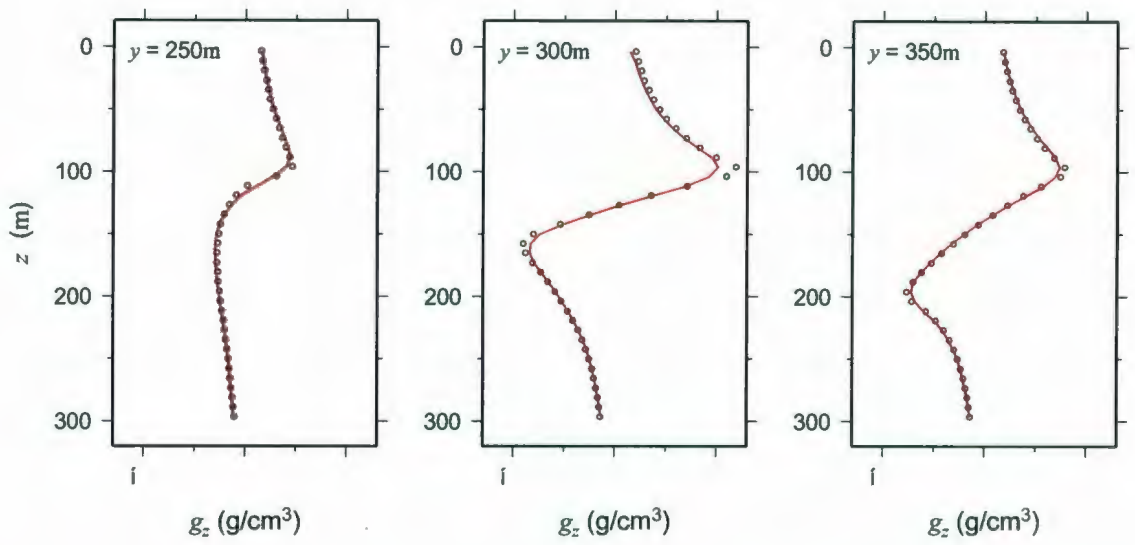

Figure 23. The observed data–set calculated from a wedge model shown in circles and the predicted data–set returned by the inversion plotted in red for varying borehole locations. *left*: $(x, y) \rightarrow (250, 300)$; *middle* $(x, y) \rightarrow (300, 300)$; *right*: $(x, y) \rightarrow (350, 300)$.

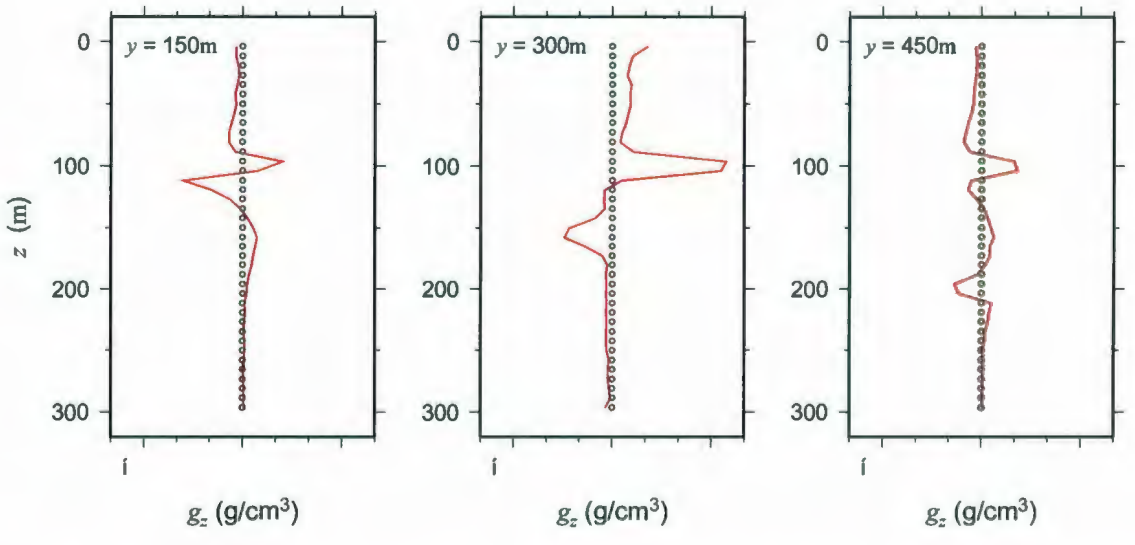

Figure 24. The errors in the gravity values computed by the inversion of the predicted data in red relative to the values of the observed data–set for the wedge model shown in circles for varying borehole locations. *left*: $(x, y) \rightarrow (250, 300)$; *middle* $(x, y) \rightarrow (300, 300)$; *right*: $(x, y) \rightarrow (350, 300)$.

The inversion ran 5 iterations with Elkbom parameters of $p = 1$ and $\epsilon = 10^{-4}$ (Section 3.4). The model is produced with only horizontal and vertical finite–differences creating a piecewise constant or blocky model with interfaces only either horizontal or vertical. The model results from this inversion are seen in Figure 25.

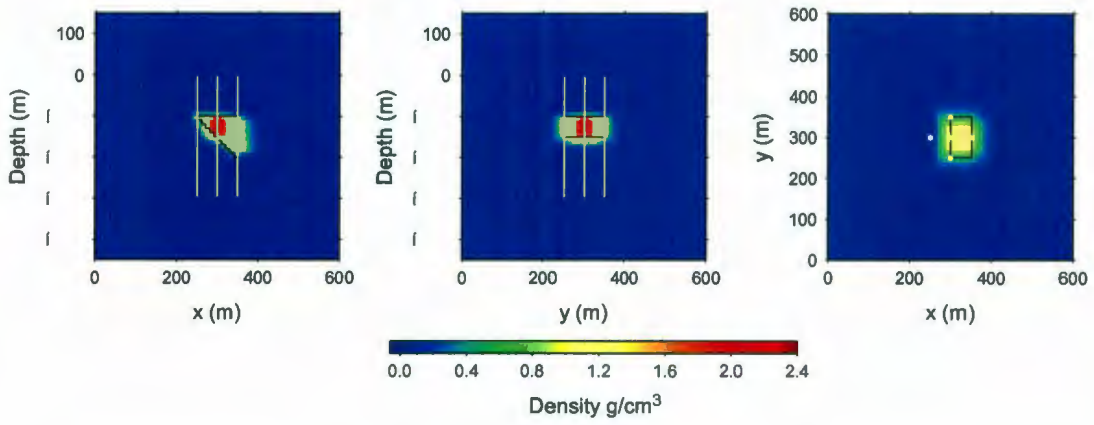

Figure 25. The mesh and block in a half–space model used for the inversion examples. *left*: the x–slice, *middle*: the y–slice; *right*: the z–slice. Borehole locations are displayed in white. The true block model is outlined in black.

The l_1 style inversion provides a density model that is a reasonable structural match to the true model in that it confines the anomalous density within the boundaries of the wedge where the inversion of Figure 22 did not. The recovered density model still displays peak densities around the central borehole, however, appropriately reproduces the true image with sharp interfaces between cells. The l_1 style inversion succeeds in eliminating the smeared and fuzzy style image present along the borehole located at $(x, y) \rightarrow (300, 350)$ in Figure 22. The output parameters of the $5th$ iteration are,

- $\rho_{max} = 2.33$ g/cm^3
- $\rho_{min} = -0.0519$ g/cm^3
- $\beta = 0.20000E - 02$
- $\phi_d = 303.83$
- $\phi_m = 0.19514E + 07$
- $\Phi = 4206.7$

5.3 Four Boreholes

In the previous five–borehole–edge scenario, the density model produced by the inversion created reasonable results in both the l_1 and l_2 style inversions. Despite this, however, the recovered models exhibited large density values concentrated around the central borehole location at $(x, y) \rightarrow (300, 300)$ seen in Figure 19, Figure 22, and Figure 25. In an attempt to produce a more even density confined within the outline of the true wedge, an inversion eliminating the central borehole data–set is performed, leaving only the data–sets from the four boreholes located on the edges of the true model to be inverted. The boreholes locations are at the exact coordinates seen in subsection 5.2. The resulting density model from the completed inversion is seen in Figure 26.

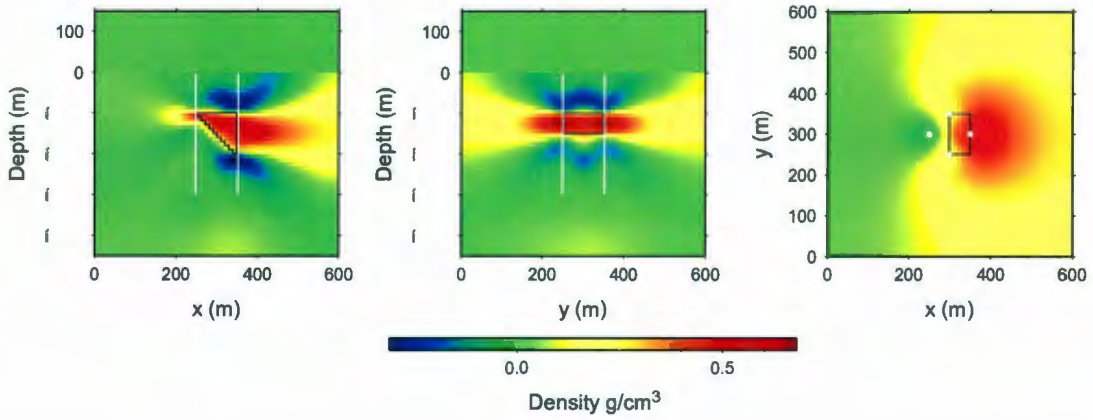

Figure 26. Inversion results for a wedge–in–a–halfspace of gravity data from four boreholes. *left*: the x–slice, *middle*: the y–slice; *right*: the z–slice. Borehole locations are displayed in white. The true wedge model is outlined in black.

Without the data from the central borehole, the inversion produces a density model which exhibits a consistent density spread within the general confines of the model boundaries and structurally does well to reproduce a wedge image. The density distribution between the boreholes in the x–slice represents well the declination of the true wedge model. However, large densities are not confined at the boundaries of the wedge

and a typical l_2 style smeared image is produced. This especially applies to cells positioned around the borehole located at $(x, y) \rightarrow (350, 300)$ in the x–slice of Figure 26 and boreholes $(x, y) \rightarrow (300, 250)$ and $(x, y) \rightarrow (300, 350)$ seen in the y–slice of Figure 26, which all exhibit large density smears. In addition, a fault of the reproduced model is that the peak densities are significantly smaller than those of the true model (0,68 compared to 2.0 g/cm^3), this can be attributed to the general fuzzy nature of the model. The output file for this inversion has the following parameters.

- $\rho_{max} = 0.68$ g/cm^3
- $\rho_{min} = -0.315$ g/cm^3
- $\beta = 0.2100E - 05$
- $\phi_d = 163.69$
- $\phi_m = 4721.3$
- $\Phi = 234.51$

5.4 Four Boreholes + Surface Data

To further the previous inversion, the data from the four boreholes described above is inverted with the addition of surface data measurements. The inclusion of this extra data in the inversion is performed in hopes of obtaining a more centrally confined density distribution and a better corresponding density value representation of the true model. The surface data contains a total of 1521 data points measured at the surface $(z = 0)$ from $(x, y) \rightarrow (105.13, 105.13) : (494.87, 494.87)$m. A datum is calculated at approximately every 10.25m. The result from the inversion is seen in Figure 27.

The addition of surface data to the four borehole data creates a similar density distribution and shape as the four borehole scenario in subsection 5.3 (See Figure 26). The inversion model, however, is improved by confining the density to the shape of the initial model and providing a better representation of the zero-halfspace background. This is attributed to the influence of the surface data in focusing high densities into cells at the center of the wedge and away from the outer proximity of the boreholes. The result provides a reasonable representation of the initial model with a significant

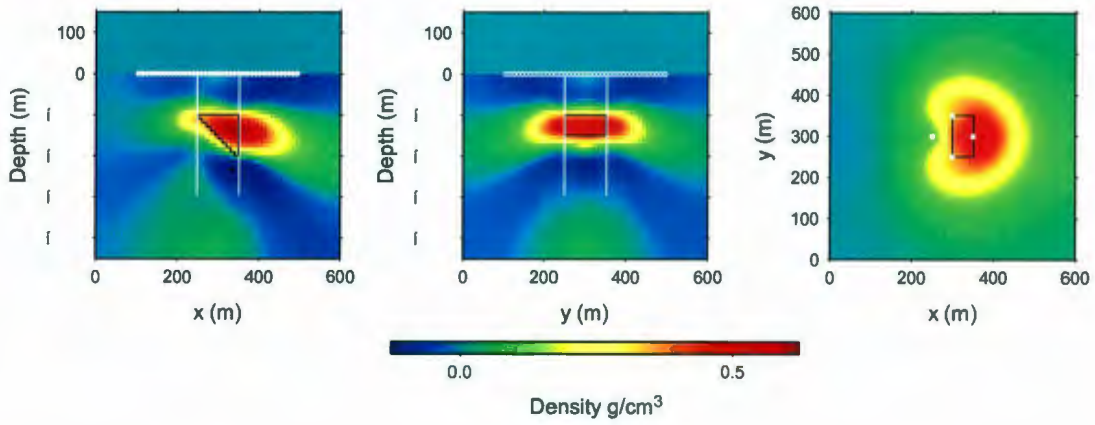

Figure 27. Inversion results for a wedge–in–a–halfspace of gravity data from four boreholes and surface measurements. *left*: the x–slice, *middle*: the y–slice; *right*: the z–slice. Borehole locations are displayed in white. The true wedge model is outlined in black.

improvement from the four borehole example exemplified by comparing z-slice profiles of Figure 27 and Figure 26. The inversion output parameters are as followed.

- $\rho_{max} = 0.623$ g/cm^3
- $\rho_{min} = -0.127$ g/cm^3
- $\beta = 0.40000E-04$
- $\phi_d = 1676.3$
- $\phi_m = 0.61559E+08$
- $\Phi = 4138.7$

5.4.1 Four Boreholes, + Surface Data l_1 style

Despite the reasonable results of the past two inversions using four boreholes, the recovered models still exhibit a fuzzy and generally smeared nature not representative of the distinct density contrasts in the true wedge model. To enhance these features, an l_1 style inversion for each scenario is examined. This is done in hopes to produce distinctive density edges between cells which are located alongside the boreholes. Also, a model that accurately correlates the density peaks present in the wedge model is desired. The l_1 style inversions are ran over multiple iterations with the default Elkbom parameters of $p = 1$ and $\varepsilon = 10^{-4}$. The $20th$ iteration model for the four borehole scenario explored

in subsection 5.3 is seen in Figure 28.

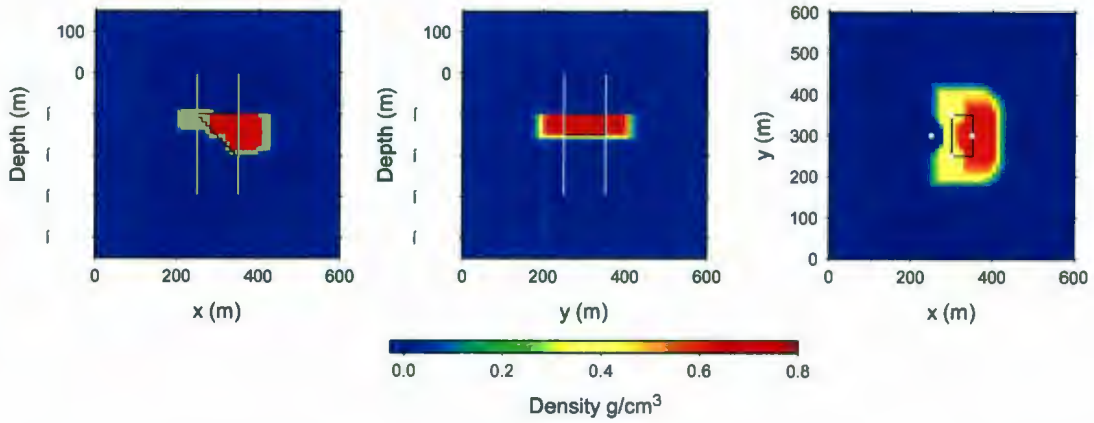

Figure 28. Inversion results for a wedge–in–a–halfspace of gravity data from five boreholes. *left*: the x–slice, *middle*: the y–slice; *right*: the z–slice. Borehole locations are displayed in white. The true block model is outlined in black.

The density model created by the $18th$ iteration for the four borehole and surface data scenario discussed in subsection 5.4 is seen in Figure 29.

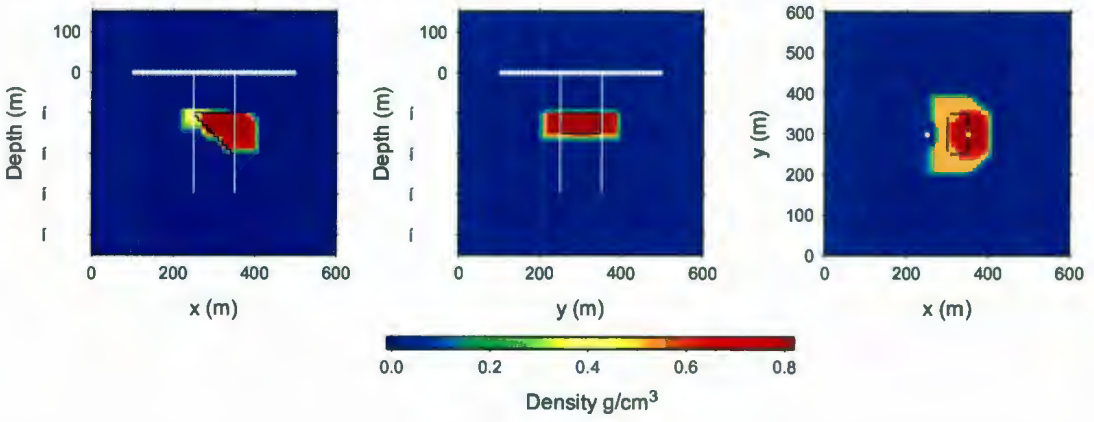

Figure 29. Inversion results for a wedge–in–a–halfspace of gravity data from five boreholes. *left*: the x–slice, *middle*: the y–slice; *right*: the z–slice. Borehole locations are displayed in white. The true block model is outlined in black.

As seen in Figure 28, the data–sets from the four boreholes locations are able to reproduce the general shape of the wedge in the true model with distinct density interfaces between cells. Despite this, however, errors still arise in the density distribution inside the wedge. The x-slice of Figure 28 displays a density of 0.5 g/cm^3 that occurs only in a few cells close to the borehole located at $(x, y) \rightarrow (250, 300)$. In the true model, these cells correspond to where the borehole would intersect the thin 10m cell of 2.0 g/cm^3 density at depth $(z) \rightarrow (-150 : -160)$ m. The remainder of the wedge is comprised of cells which hold a uniform, higher density of approximately 0.74g/cm^3. Despite the difference in density values to the true model, the inversion provides a model which generally reproduces the shape and constant density characteristics of the true model. The outcome parameters for the $20th$ iteration are as follows,

- $\rho_{max} = 0.736$ g/cm^3
- $\rho_{min} = -0.0262$ g/cm^3
- $\beta = 0.40000E - 02$
- $\phi_d = 195.65$
- $\phi_m = 0.11187E + 07$
- $\Phi = 4670.4$

The resulting l_1 density model from the four borehole and surface data example is seen in Figure 29. The outcome is similar to the four borehole scenario, however the addition of surface data helps in obtaining a more even density distribution within the wedge. The region of anomalous density around the borehole at $(x, y) \rightarrow (250, 300)$ in Figure 25 is still apparent, however, the addition of surface data helps to focus the center of density closer to the confines of the true wedge. The outcome parameters for the $18th$ iteration are.

- $\rho_{max} = 0.811$ g/cm^3
- $\rho_{min} = -0.00819$ g/cm^3
- $\beta = 0.90000E - 02$
- $\phi_d = 462.82$
- $\phi_m = 0.89535E + 06$
- $\Phi = 8521.0$

5.5 Summary

Multiple inversions scenarios of gravity data for a wedge–in–a–halfspace model were presented throughout this Chapter and in Appendix B. Through study of these examples, the ability of the inversion to produce a model that recreates the density distribution of the true model depends on the locations and number of borehole and surface gravity data used in the inversion.

The ability to recreate the boundaries of the dense wedge were dependent on the location of the boreholes away from the center of mass. In cases where the boreholes were too far away from the density anomaly, the produced model did not recreate the boundaries of the dense wedge. In examples where the outer boreholes were positioned closer to the edges of the anomaly, the inversion was able to produce models which showed the sharp, tapered boundaries of the dense wedge and provided a better representation of the density distribution. Accurate density models were also produced with four boreholes located on the edge of the true wedge, excluding the central borehole gravity data. This is due to the asymmetry of the wedge model about the center of the x–axis.

In similarity with the block–in–a–halfspace model, the accuracy of the produced density models is dependent on the amount of borehole and surface data incorporated into the inversion. The examples suggest that ideally, a borehole located directly through the center of mass of an anomaly, and borehole data located at the edges of the anomaly are able to produce an accurate density distribution and shape of a asymmetric dense shape. This setup sees that the central borehole will recreate an appropriate peak density, while the outer boreholes confine the high densities to the edges of the density anomaly.

CHAPTER 6

Minimum–Structure Inversion of the Voisey's Bay Ovoid

The following chapter discusses the procedure and analysis for minimum–structure inversions performed to recreate the density structure of the main Ovoid of the Voisey's Bay mineral deposit described in Section 1.6. Inversions involving differing amounts of borehole locations, data–sets, reference models and varying parameters in the *g3dfd* inversion algorithm are examined.

The gravity data–sets used for the inversions are synthetically calculated by forward modelling at different observation locations for a model representation of the subsurface density distribution in the vicinity of the Ovoid. The model was constructed by Ash (2007) through use of downhole samples from over 500 existing drill holes. This provided an extensive database where assay percentages of iron, sulphur and copper were used to create density values. The density equations were derived by use of regression analysis of geochemical data (Ash, 2007). The densities calculated between the troctolite and massive sulphide samples provided a general correlation between the amount of sulphides and corresponding densities. Mean densities below 3.2 g/cm^3 correspond to less than 15% massive sulphides, mean densities between 3.2 to 4.6 g/cm^3 are associated with 40 to 75% massive sulphides, and densities greater than 4.6 g/cm^3 are indicative of massive sulphides.

The 3D rectangular mesh used in the model is based on UTM grid coordinate system and has a top southwest corner of 555297.5 E, 6242847.5 N and at an elevation of 172.5 m above sea level (Ash, 2007). There are 87 cells in the easting direction, 61 cells in the northing direction and 54 cells in the vertical direction meaning that there are 286,578 total cells in the mesh. Each cell has dimensions $(\Delta x, \Delta y, \Delta z) \rightarrow (10, 10, 5)$ m and is considered an appropriate size to enable adequate representation of the various

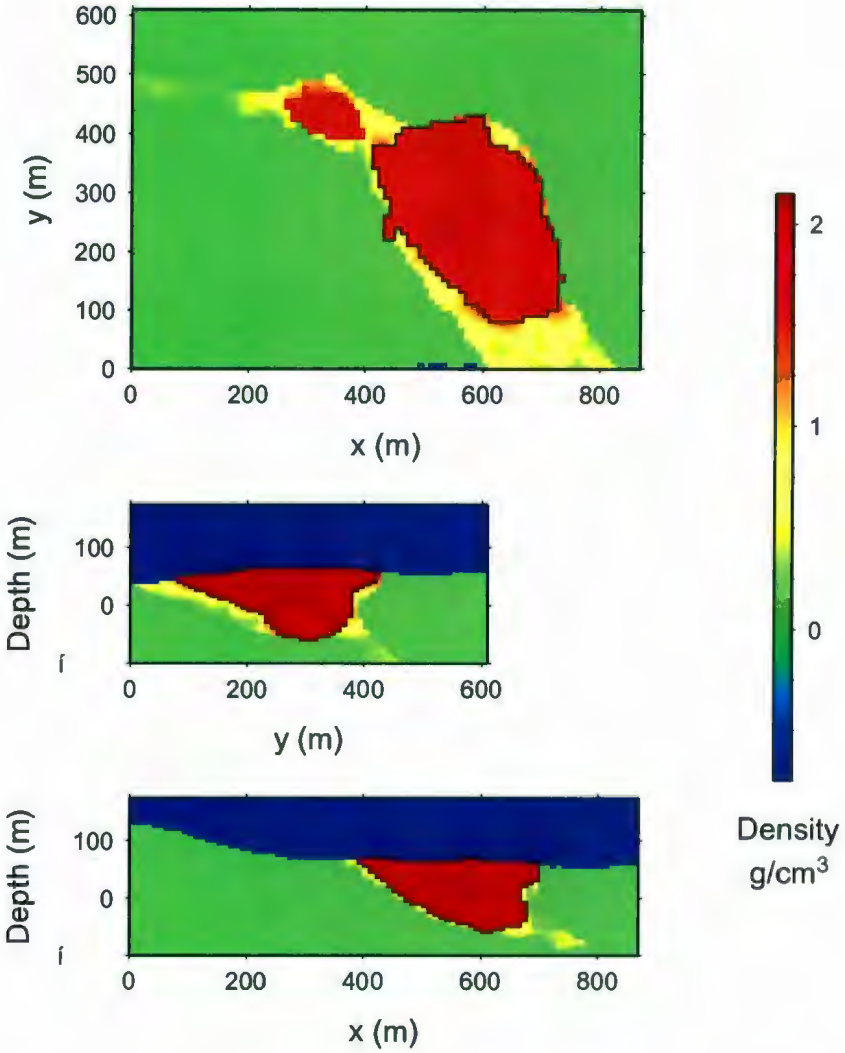

Figure 30. The mesh and model of the Voisey's Bay main Ovoid used for the inversion examples. *top*: the z–slice, $z = 37$ m, *middle*: the y–slice, $x = 600$ m; *bottom*: the x–slice, $y = 600$ m. Borehole locations are displayed in white. The true massive sulphide Ovoid model is outlined in black.

rock types and density distributions of the Ovoid. The mesh dimensions span 870 $\times$ 640 $\times$ 270 m and was chosen to properly accommodate the local topography and all drill hold locations. The domain is also large enough to incorporate the Ovoid, enveloping troctolite, and the enclosing gneiss country rock (Ash, 2007). The density model was created in Gocad using a Kriging procedure which interpolates the measured densities of the borehole samples to obtain densities between boreholes. The model exhibits four distinct regions of the geology: the overburden, enderbitic gneiss, troctolite hosting various percentages of disseminated sulphides, and massive sulphide zones. In the model, all density values are relative to a 2.67 g/cm^3 Bouguer anomaly correction. The model is displayed in three seperate slices in Figure 30. The x–slice displays the xz plane at $y = 310$ m; the y–slice displays the yz plane at $x = 600$ m; and the z–slice displays the xy plane taken at $z = 37$ m. The goal of each inversion is to reproduce a density model that correlates well with the structure and density distribution of the true Ovoid model at these slices. In each borehole, the observed data–set is a total of 79 evenly spaced measurements taken from depths $(z) \rightarrow (85.85 : -93.85)$ m, therefore at approximately every 2.30 m. The observation locations were chosen so that measurements were calculated from the top of the overburden to the bottom of the mesh in hopes to fully study the effects of the Ovoid and varying surrounding densities. Random Gaussian noise of standard deviation equal to five percent of the magnitude of the datum is added to all data–sets.

Minimum–structure inversions are performed using the default l_2 norm of model structure and x, y and z first-order finite–difference terms with $\alpha_1 = 0$, $\alpha_2 = \alpha_3 = \alpha_4 = 1$, and $\alpha_5 = \cdots = \alpha_{14} = 0$ unless otherwise noted (Section 3.2.2). The depth weighting parameters are initially set to default with $\tilde{\beta} = 2$ and $z_0 = 1.25$ m (a quarter of the smallest cell dimension) (Section 3.2.3). The inversions are performed with a value of β which reproduces a data misfit value ϕ_d that equals the total number of data points

within a 10% error margin. There is no reference model applied to the inversions unless otherwise noted.

6.1 Five Boreholes

The first inversion executed involves the gravity data calculated along the lengths of five boreholes. The boreholes are located at $(x, y) \rightarrow (450, 310)$, $(x, y) \rightarrow (610, 310)$, $(x, y) \rightarrow (690, 310)$, $(x, y) \rightarrow (610, 170)$, and $(x, y) \rightarrow (610, 380)$ and were chosen with the shape of the Ovoid in mind. A central borehole is located through the center of density and four boreholes outline the Ovoid at its edges. The locations of the boreholes and the resulting density model from the completed inversion are seen in Figure 31. The predicted and observed gravity data–sets for each borehole are plotted in Figures 32 and 33

The produced density model is not a very good representation of the true model. The peak density is greater than that of the true model by approximately 1.5 g/cm^3 and the density distribution within the Ovoid is highly variable. High densities are also spread outside of the true model around the outer boreholes, which is likely due to the general fuzzy nature of l_2 inversions. There are, however areas of high density values present in between the central and surrounding boreholes, seen particularly in Figure 31 *bottom*. One concern present in the resulting model is that, despite boreholes traveling directly through the Ovoid, the inversion appears to allocate mainly low density values to the cells adjacent to the borehole. The density model suggests that the inversion is encouraging the distribution of high densities away from the observation locations.

The outcome file from the completed inversion displays the following parameters,

- $\rho_{max} = 3.67$ g/cm^3
- $\rho_{min} = -3.69$ g/cm^3
- $\beta = 0.55E - 06$
- $\phi_d = 400.$
- $\phi_m = 0.39E + 10$
- $\Phi = 2528$

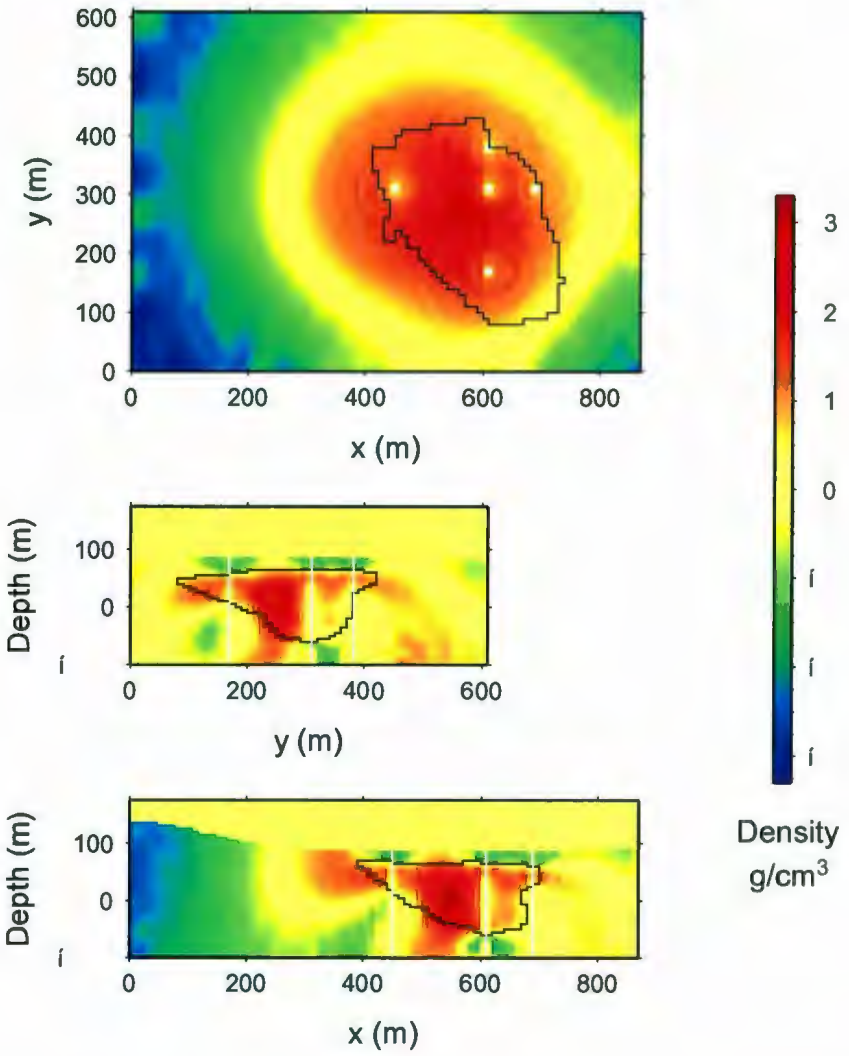

Figure 31. Inversion results for the Ovoid model of gravity data from five boreholes. *top*: the z–slice, $z = 37$ m, *middle*: the y–slice, $x = 600$ m; *bottom*: the x–slice, $y = 600$ m. Borehole locations are displayed in white. The true massive sulphide Ovoid model is outlined in black.

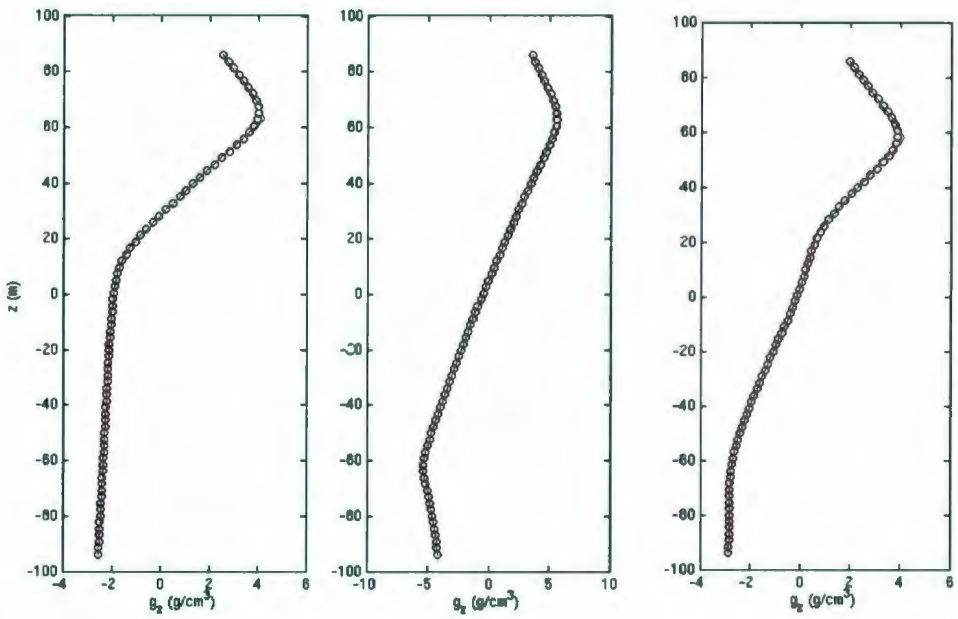

Figure 32. The observed data–set calculated from the Ovoid model shown in circles and the predicted data–set returned by the inversion plotted in red for varying borehole locations. *left*: $(x, y) \rightarrow (450, 310)$; *middle* $(x, y) \rightarrow (610, 310)$; *right*: $(x, y) \rightarrow (670, 310)$.

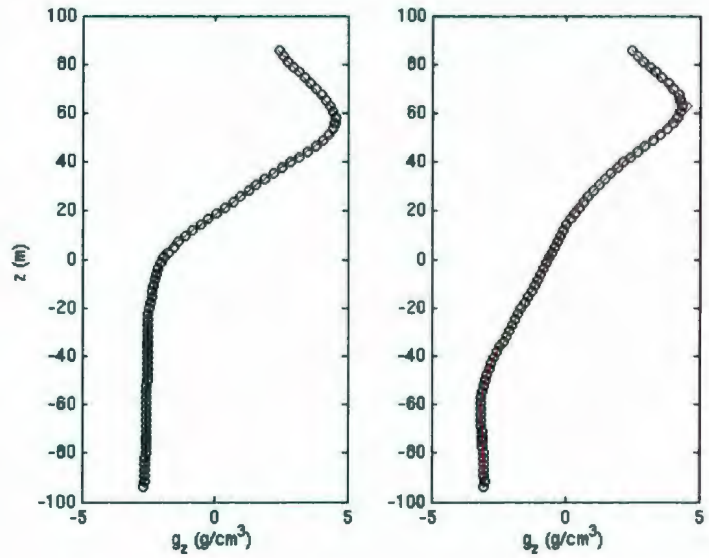

Figure 33. The observed data–set calculated from the Ovoid model shown in circles and the predicted data–set returned by the inversion plotted in red for varying borehole locations. *left*: $(x, y) \rightarrow (610, 170)$; *right*: $(x, y) \rightarrow (610, 380)$.

To further study the peculiarities of the density model, specifically the low density values in cells adjacent to the boreholes, the weighting function which is applied in the inversion and presented in Section 3.2.3 (see equation (43)) is examined in further detail. The function influences the inversion to allocate densities, with equal probability, to cells away from the observed data points. The results of altering the parameter $\tilde{\beta}$ in the weighting function are presented throughout the following two sections.

6.2 Five Boreholes, $\tilde{\beta} = 1$

The next inversion example examines the effects on the produced density model when the $\tilde{\beta}$ weighting parameter is changed from the default of $\tilde{\beta} = 2$ to a value of $\tilde{\beta} = 1$. The observation locations and number of boreholes remain the same as in the previous example. The density model produced by the completed inversion is seen in Figure 34.

The impact of $\tilde{\beta}$ on the inversion is clearly presented by comparing the density distributions of Figure 31 and Figure 34. In the initial scenario, with default weighting parameters, the model exhibited high densities away from the borehole locations, whereas an opposite scenario occurs with $\tilde{\beta} = 1$ where high densities are allocated to cells directly near the boreholes and spreading of high densities to cells away from the boreholes appears to be discouraged. Peak densities are still higher than the true models, however are less deviated than the default five borehole inversion example. Also, despite the lack of high densities between boreholes, the model coincides more accordingly with the shape of the true Ovoid model. This could be because the boreholes are all in the Ovoid and the inversion and high densities are constrained to be near the boreholes. The output parameters from the completed inversion are as follows.

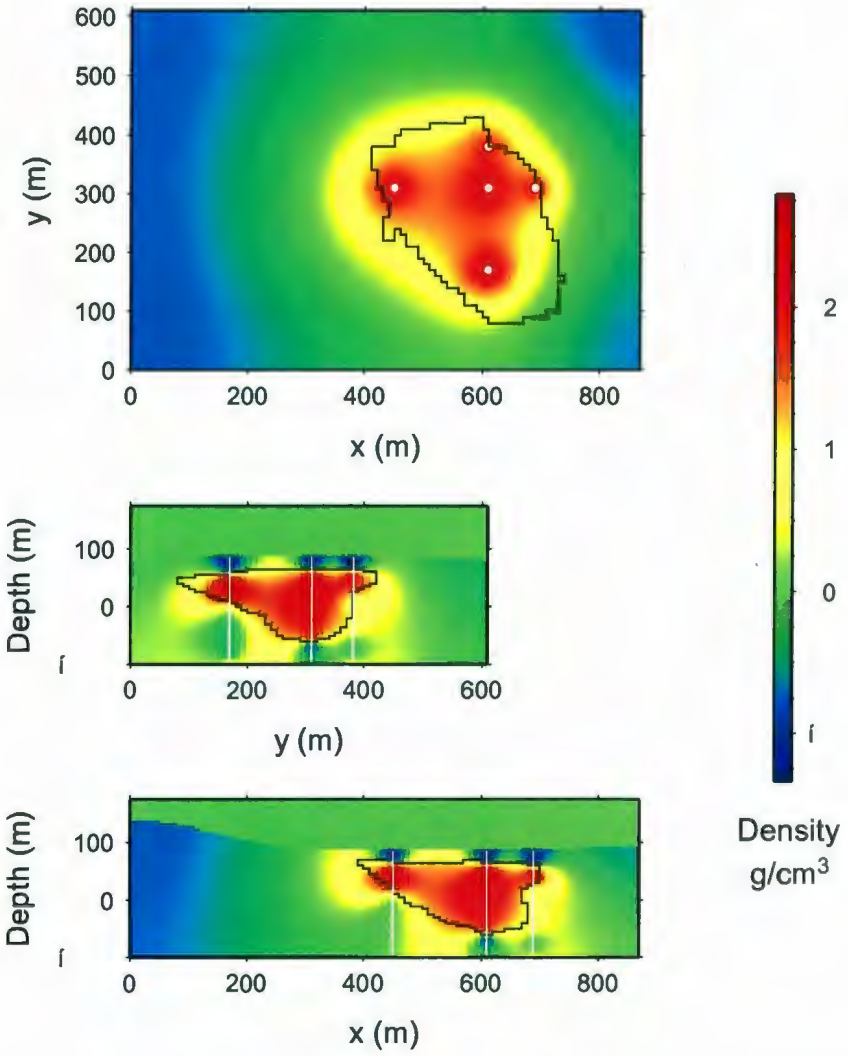

Figure 34. Inversion results for the Ovoid model of gravity data from five boreholes applying a weighting parameter of $\tilde{\beta} = 1$. *top*: the z–slice, $z = 37$ m, *middle*: the y–slice, $x = 600$ m; *bottom*: the x–slice, $y = 600$ m. Borehole locations are displayed in white. The true massive sulphide Ovoid model is outlined in black.

- $\rho_{max} = 2.77\ \text{g/cm}^3$
- $\rho_{min} = -1.37\ \text{g/cm}^3$
- $\beta = 0.51E-06$
- $\phi_d = 382.$
- $\phi_m = 0.692E+10$
- $\Phi = 3911$

6.3 Five Boreholes, $\tilde{\beta} = 1.5$

The effects of modifying the value of $\tilde{\beta}$ were previously examined with the two scenarios providing differing features in the output density models. It is noted that when $\tilde{\beta}$ is decreased, the weighting function effects also decrease causing the model to exhibit high densities in cells adjacent to the observation locations and limit the spreading out of density anomalies throughout the model. On the other hand, when $\tilde{\beta}$ is increased, the effects of the weighting function are increased causing the inversion to allocate densities away from the observation locations, which includes situations where boreholes are located directly through areas of high density. In both examples, the produced model showed some similarities with the structure and density distribution of the true model, however it is believed that further adjustment of the value of $\tilde{\beta}$ will provide a better representation.

The following inversion attempts to create a model that better represents the true model by applying a weighting function parameter value of $\tilde{\beta} = 1.5$. This is conducted in hopes of producing a model that exhibits high densities both between and adjacent to the borehole measurements within the confines of the true Ovoid. The density distribution provided by the completed inversion is seen in Figure 35.

The model produced by this inversion is a more accurate representation of the true model with the structure and density distribution correlating within reason. By inverting the data with a value of $\tilde{\beta} = 1.5$ in the weighting function, the inversion is able to place densities in between boreholes a characteristic seen in Figure 31, and in cells adjacent to the length of the boreholes as seen in Figure 34. The output parameters for the inversion

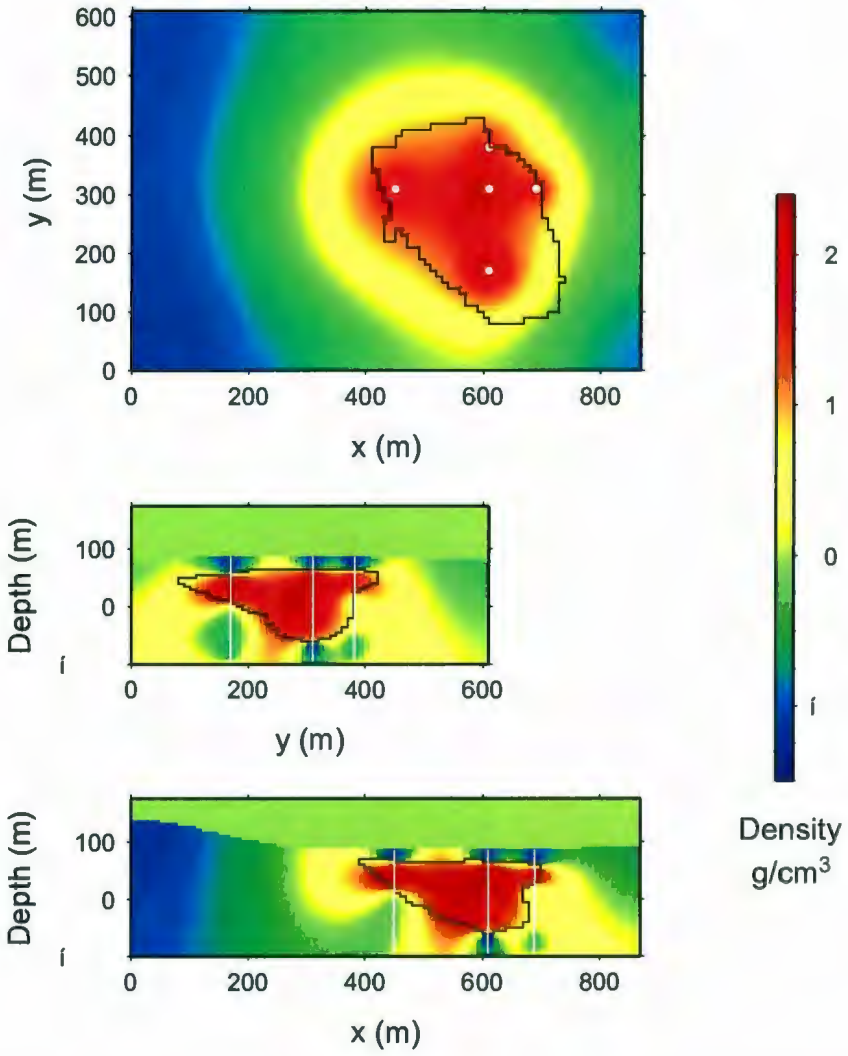

Figure 35. Inversion results for the Ovoid model of gravity data from five boreholes applying a weighting parameter of $\tilde{\beta} = 1.5$. *top*: the z–slice, $z = 37$ m, *middle*: the y–slice, $x = 600$ m; *bottom*: the x–slice, $y = 600$ m. Borehole locations are displayed in white. The true massive sulphide Ovoid model is outlined in black.

are,

- $\rho_{max} = 2.38$ g/cm^3
- $\rho_{min} = -1.40$ g/cm^3
- $\beta = 0.65E-06$
- $\phi_d = 398$
- $\phi_m = 0.43E+10$
- $\Phi = 3227$

Since inversion models that feature a $\tilde{\beta} = 1.5$ value in the depth weighting function providing a better overall representation of the true model, all inversion examples will now use $\tilde{\beta} = 1.5$ as a default parameter.

6.4 Four Boreholes

The next inversion is conducted with borehole data from four boreholes. The data is from boreholes located at $(x, y) \rightarrow (450, 300)$, $(x, y) \rightarrow (690, 310)$, $(x, y) \rightarrow (610, 170)$, and$(x, y) \rightarrow (610, 380)$. It is the same scenario as the five borehole study with the middle borehole data removed from the inversion. The density distribution provided by the completed inversion is seen in Figure 36.

The produced model shows the impact that the central borehole has in reconstructing the proper shape of the Ovoid. With only four boreholes used in the inversion, the uniform density distribution throughout the Ovoid is not recovered. High densities are present in cells around the boreholes, however are not found between the boreholes. Also, the high densities are present in a constant radius around the boreholes, which makes for high densities outside of the Ovoid limits. The output parameters for the inversion are,

- $\rho_{max} = 2.39$ g/cm^3
- $\rho_{min} = -1.40$ g/cm^3
- $\beta = 0.65E-06$
- $\phi_d = 308$
- $\phi_m = 0.341E+10$
- $\Phi = 2532$

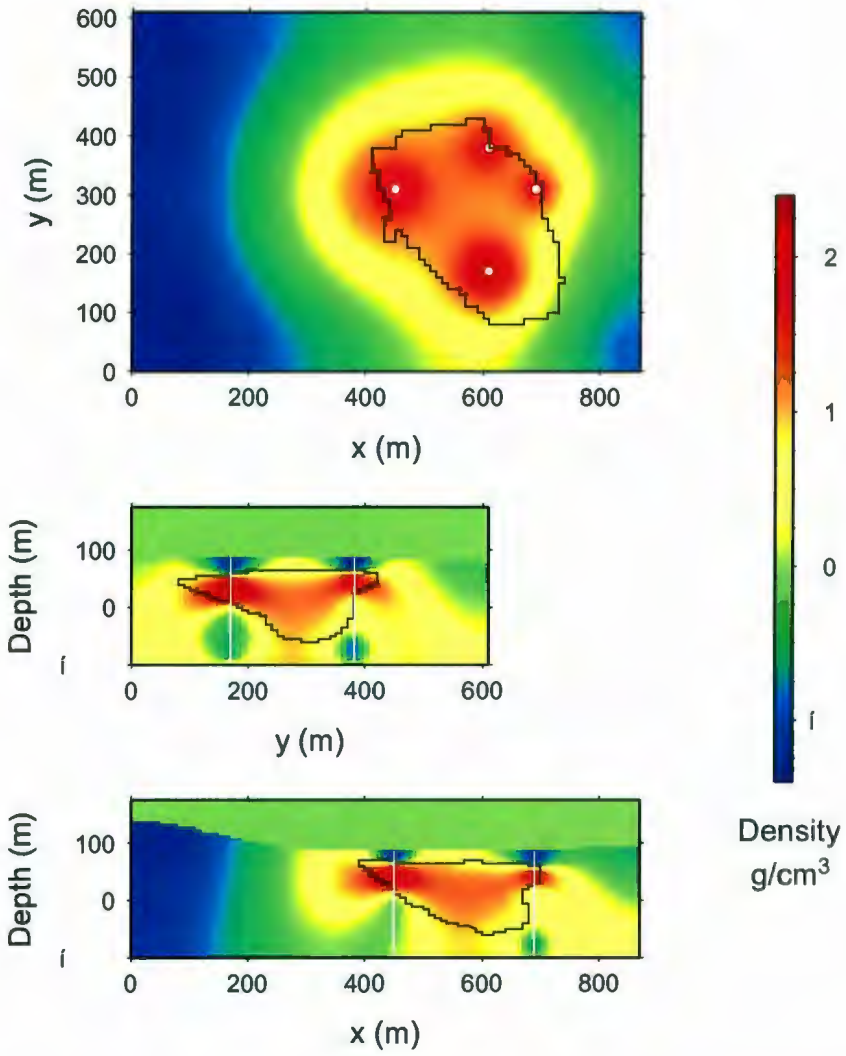

Figure 36. Inversion results for the Ovoid model of gravity data from four boreholes. *top*: the z–slice, $z = 37$ m, *middle*: the y–slice, $x = 600$ m; *bottom*: the x–slice, $y = 600$ m. Borehole locations are displayed in white. The true massive sulphide Ovoid model is outlined in black.

6.5 Four Boreholes + Surface Data

The results from the previous section using four boreholes proved to have inappropriately low density values between the boreholes. In an attempt to influence the inversion to allocate densities towards the center of the Ovoid, a scenario mimicking the four boreholes of the previous example is performed with the addition of 89 surface data measurements. It was measured along lines separated by an average of 200 m and along each line, the spacing between observation locations ranges from 25 to 50 m. The surface gravity data–set is supplied by the Voiseys Bay Nickel Company and is seen in Figure 37 (see also Ash (2007)). The data was subjected to the typical cor-

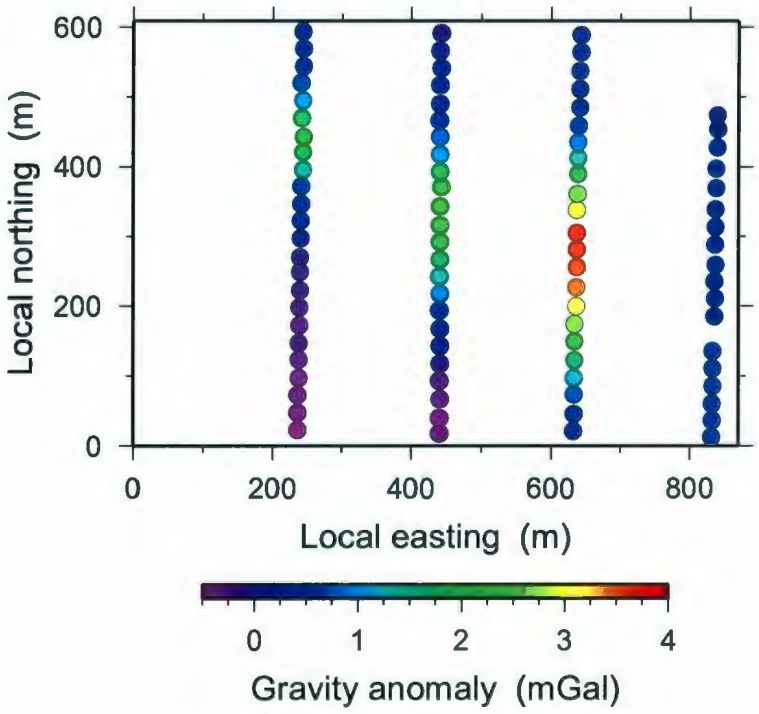

Figure 37. Surface gravity data–set collected over the Voisey's Bay Ovoid

rections outlined in Chapter 1 and are relative to the standard crustal density value of 2.67 g/cm^3. The provided data had no accompanying uncertainty estimates, therefore uncertainties of 0.05 g/cm^3 were assumed in the inversion. The density model produced

by the completed inversion is seen in Figure 38.

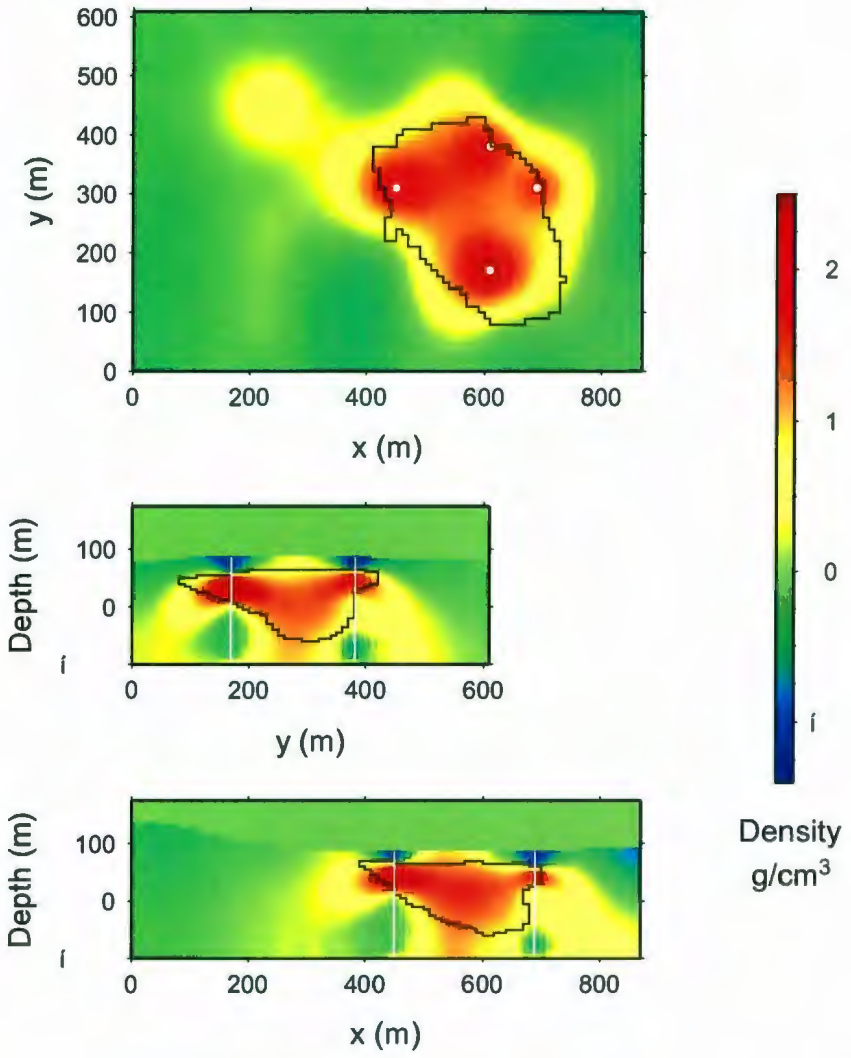

Figure 38. Inversion results for the Ovoid model of gravity data from four boreholes and surface measurements. *top*: the z–slice, $z = 37$ m, *middle*: the y–slice, $x = 600$ m; *bottom*: the x–slice, $y = 600$ m. Borehole locations are displayed in white. The true massive sulphide Ovoid model is outlined in black.

With the inclusion of surface data, the density model produced by the inversion is a slight improvement over the four borehole study, the main difference being the distribution of negative density values on the outer edges of the domain. The surface data moderately influences the distribution of high density values in between the borehole

locations. It is possible that with additional surface gravity values, higher densities would be allocated towards the center of the Ovoid. The output parameters of the inversion are as follows,

- $\rho_{max} = 2.46$ g/cm^3
- $\rho_{min} = -1.57$ g/cm^3
- $\beta = 0.85E-06$
- $\phi_d = 418$
- $\phi_m = 0.358E+10$
- $\Phi = 3462$

6.6 Five Boreholes and overburden model DM05

The following examples study inversions which incorporate a reference model (DM05) of the overburden densities present in the true Ovoid model (Ash, 2007). The reference model is comprised of a basic two-layered density distribution which is divided by the known position of the overburden-bedrock contact. In the model, cells that are in the overburden and above are assigned density values of -0.75 g/cm^3 and all other cells are assigned density values of 0.14 g/cm^3 as seen in Figure 39. It is noted that all cells above the overburden are given a value of -0.75 g/cm^3 as well, however these cells are considered void by the inversion with the inclusion of the topography file. It is observed that in past models, high density values were spreading into the region of the overburden creating possible error in the produced model's density distribution. The inclusion of the overburden densities is done in hopes of obtaining a more distinct density barrier between the top of the Ovoid and overburden encouraging the inversion to allocate a consistent density distribution to cells within the Ovoid.

The inversions incorporates the data calculated from the five identical boreholes examined in Sections 6.1–6.3. The resulting density model from the completed inversion is seen in Figure 40

The produced density model displays a boundary between the overburden and the remaining areas of the subsurface and provides a superior upper density barrier for the

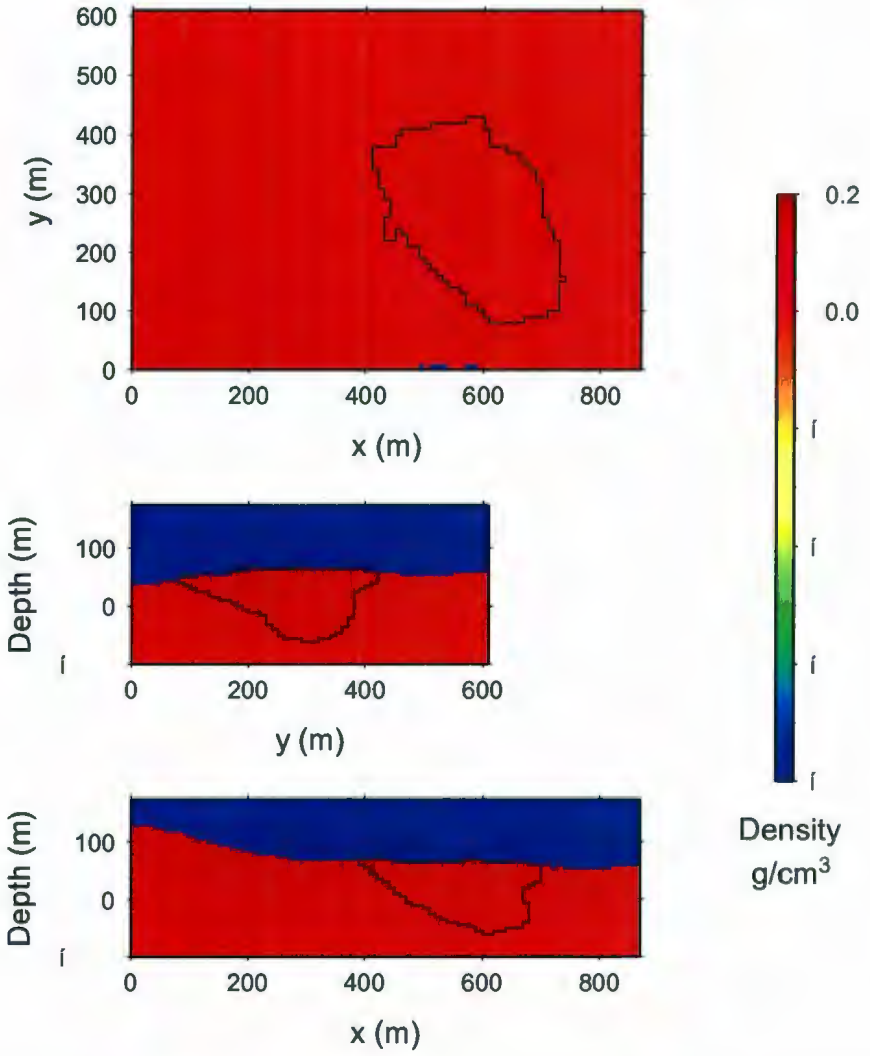

Figure 39. The reference model DM05 that incorporates the overburden densities. *top*: the z–slice, $z = 37$ m, *middle*: the y–slice, $x = 600$ m; *bottom*: the x–slice, $y = 600$ m. Borehole locations are displayed in white. The true massive sulphide Ovoid model is outlined in black.

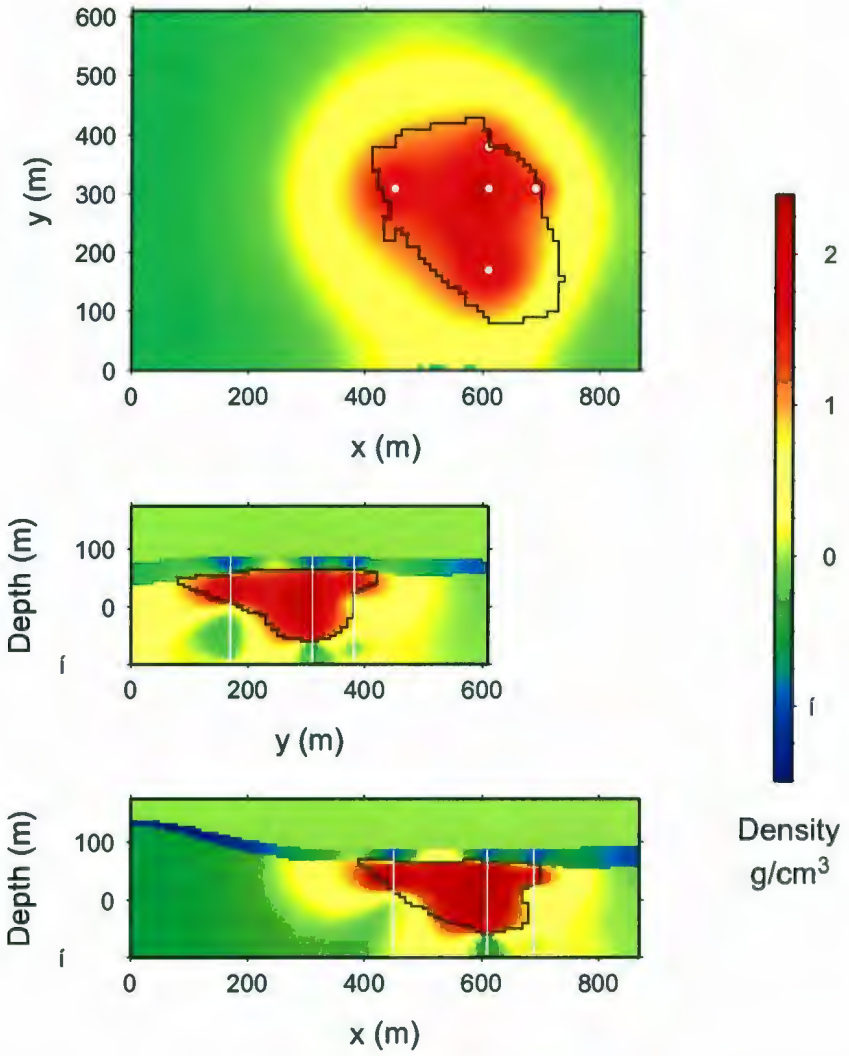

Figure 40. Inversion results for the Ovoid model of gravity data from five boreholes applying the reference model DM05. *top*: the z–slice, $z = 37$ m, *middle*: the y–slice, $x = 600$ m; *bottom*: the x–slice, $y = 600$ m. Borehole locations are displayed in white. The true massive sulphide Ovoid model is outlined in black..

Ovoid in comparison to the density model produced in Figure 35. The sharp interface observed between the overburden and underlying material is a direct result from incorporating the DM05 overburden reference model into the inversion. The densities in the overburden above the Ovoid, however, range between large positive and negative values. The density ranges from approximately 0.6 to -1.5 g/cm^3 and does not correspond to the uniform -0.75 g/cm^3 density that was assigned by the reference model. The parameters from the completed inversion are as follows,

- $\rho_{max} = 2.4$ g/cm^3
- $\rho_{min} = -1.47$ g/cm^3
- $\beta = 0.12E-05$
- $\phi_d = 383$
- $\phi_m = 0.209E+10$
- $\Phi = 2901$

6.7 Five Boreholes and overburden model DM05, $\alpha_s = 1$

To allow the reference model to have more of an influence on the final model, the value of the spatial weighting coefficient α_s (or α_1) from equation (41) can be altered. The value of α_s has the ability to either increase or decrease the influence of function w_s which controls the amount of correlation between the final model and the reference model. In all previous inversions, the value of α_s had a default value of zero, thus limiting the influence of the reference model to the derivative terms in equation (41). The appropriate value of α_s is undefined and relative on the dynamics of the inversion. Here a value of $\alpha_s = 1$ is chosen and implemented into the inversion. The resulting density model is seen in Figure 41.

Changing the value of the term α_s has a great effect on the inversion. The densities throughout the overburden are more constrained and range from approximately -1.0 g/cm ^{3} to 0. The density distribution within the Ovoid is more uniform as well. The areas in the troctolite region are also in agreement with the initial Ovoid model and exhibit a average density of around 0.2 g/cm^3. The model does have areas of error seen

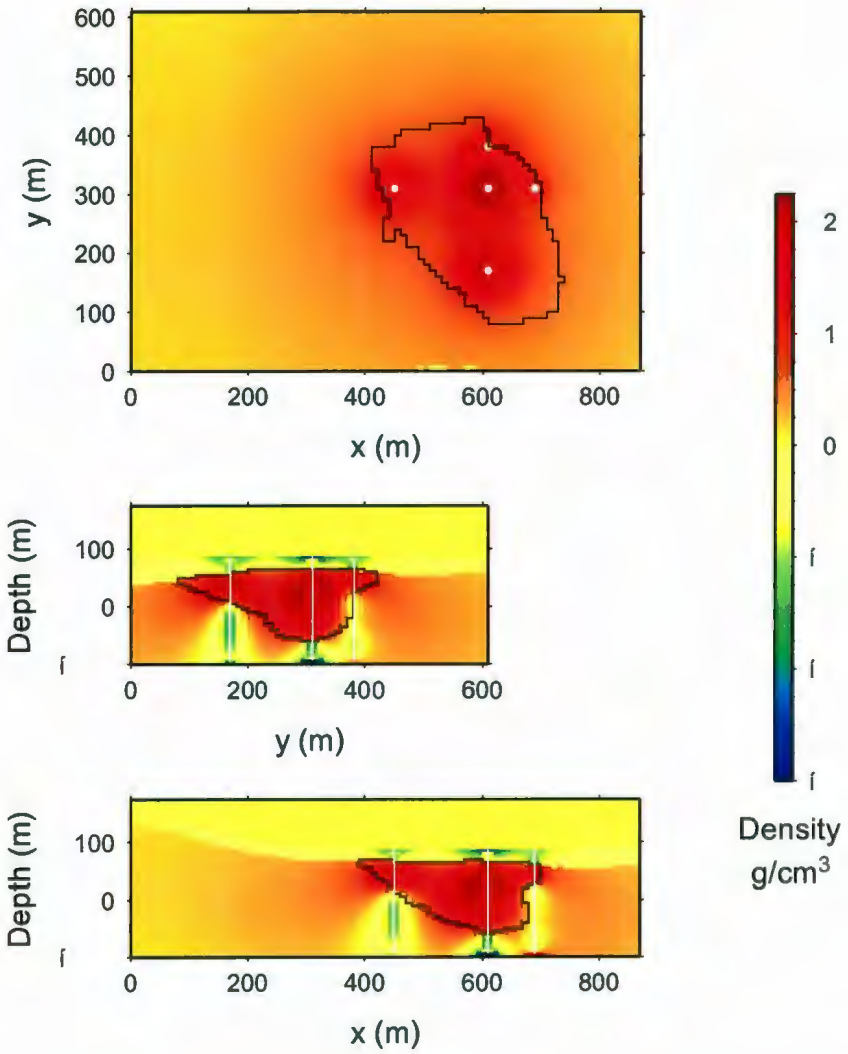

Figure 41. Inversion results for the Ovoid model of gravity data from five boreholes applying the reference model DM05 and a parameter value of $\alpha_s = 1$. *top*: the z–slice, $z = 37$ m, *middle*: the y–slice, $x = 600$ m; *bottom*: the x–slice, $y = 600$ m. Borehole locations are displayed in white. The true massive sulphide Ovoid model is outlined in black.

at the bottom of the boreholes at a depth of approximately $z = -100$ m, where the model exhibit either extreme highs or extreme lows in density. The cause of this is likely due to the inversion overcompensating when trying to match the values of all cells with that of the reference model. The output parameters of the inversion are,

- $\rho_{max} = 2.24$ g/cm^3
- $\rho_{min} = -4.68$ g/cm^3
- $\beta = 0.52E-08$
- $\phi_d = 392$
- $\phi_m = 0.21E+13$
- $\Phi = 11115.$

6.8 Five Boreholes, DM05 $\alpha_s = 1$ with weighting

By encouraging the inversion to assign the reference model densities of the overburden to the model, it is assumed that the remaining density distribution inside the confines of the Ovoid will correlate better with the true model. This is because the inversion is given a starting density model to use as a guide to aid in the remaining density distribution. To assure that the cells in the overburden are assigned a value of -0.75 g/cm^3, an extra weighting file is included in the inversion procedure. The file contains a list of entries, one for each cell in the mesh. Manipulation of the entries can greatly encourage the inversion to assign densities from the reference model to the corresponding cells of the produced model. The weighting file used in the following example has entries of 100 for cells in the overburden and entries of 1 for every other cell in the mesh. This greatly encourages densities of -0.75 g/cm^3 to be assigned to cells in the overburden. The inversion is executed with identical data from the previous example and with the same value of $\alpha_s = 1$, the only difference being the inclusion of the weighting file. The density model produced from the inversion is seen in Figure 42.

From the inversion result, it is clearly shown that the extra weighting file limits the overburden densities to -0.75 g/cm^3. It also appears that the densities of the enveloping rocks average around a 0.1 g/cm^3 density which is close to their true value of 0.14 g/cm^3.

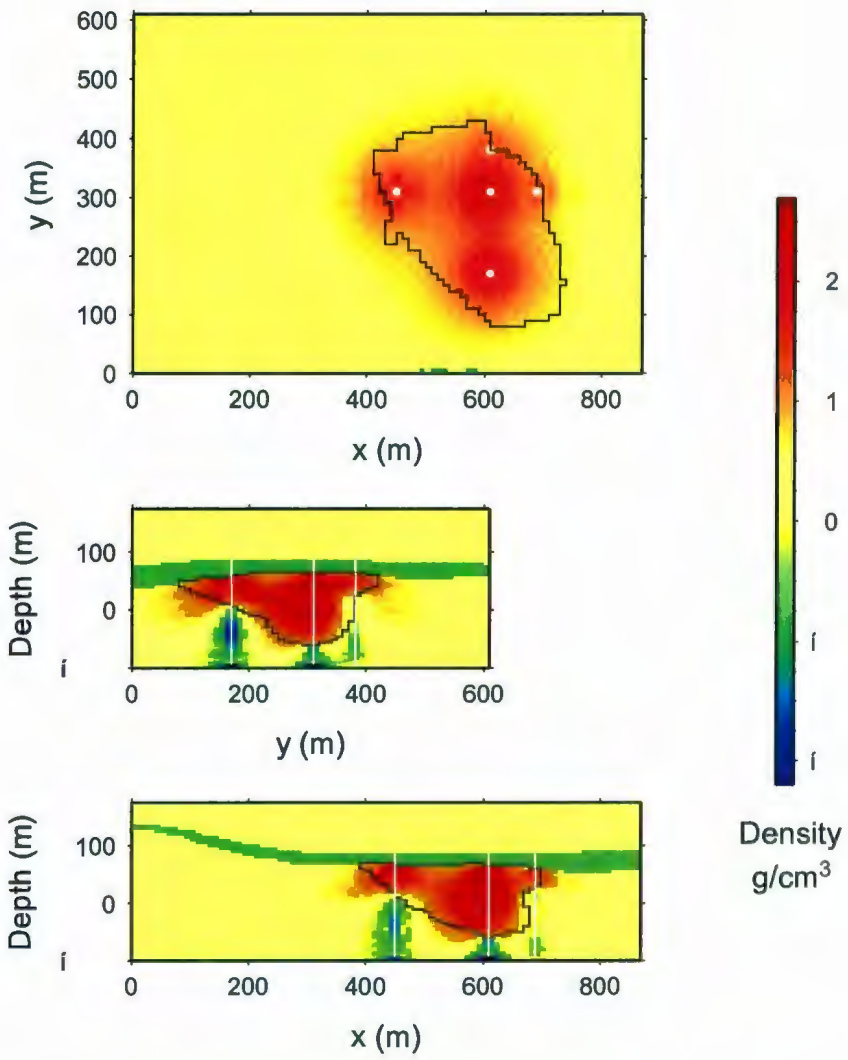

Figure 42. Inversion results for the Ovoid model of gravity data from five boreholes applying the reference model DM05, a parameter value of $\alpha_s = 1$ and extra weighting for cells in the overburden. *top*: the z–slice, $z = 37$ m, *middle*: the y–slice, $x = 600$ m; *bottom*: the x–slice, $y = 600$ m. Borehole locations are displayed in white. The true massive sulphide Ovoid model is outlined in black.

The densities within the Ovoid, however, are not modeled as well as in the past model as the densities between boreholes are of lower value. The output parameters from the inversion are,

- $\rho_{max} = 2.67$ g/cm^3
- $\rho_{min} = -3.81$ g/cm^3
- $\beta = 0.50E-08$
- $\phi_d = 373$
- $\phi_m = 0.25E+13$
- $\Phi = 13086.$

6.9 Five Boreholes and reference model DM09

The next example is performed to simulate an inversion which incorporates information collected from the five boreholes; that is, densities derived by methods such as gamma-ray borehole logging or core sample analysis from boreholes. The inversion includes a reference model that has assigned density values for the cells adjacent to each borehole. The reference model is shown in Figure 43. The inversion includes the identical five borehole data present from past examples and a coefficient value of $\alpha_s = 1$ is used. The resulting inversion density model is seen in Figure 44.

This density model does create the density pattern implied by the reference model, however, the incorporated density values are massively skewed. The high density values present around the boreholes limit an even spread of density in between boreholes and the result is an overall poor representation of the true model. The parameters produced from the inversion are as follows,

- $\rho_{max} = 4.25$ g/cm^3
- $\rho_{min} = -1.87$ g/cm^3
- $\beta = 0.85E-06$
- $\phi_d = 393$
- $\phi_m = 0.36E+10$
- $\Phi = 3425$

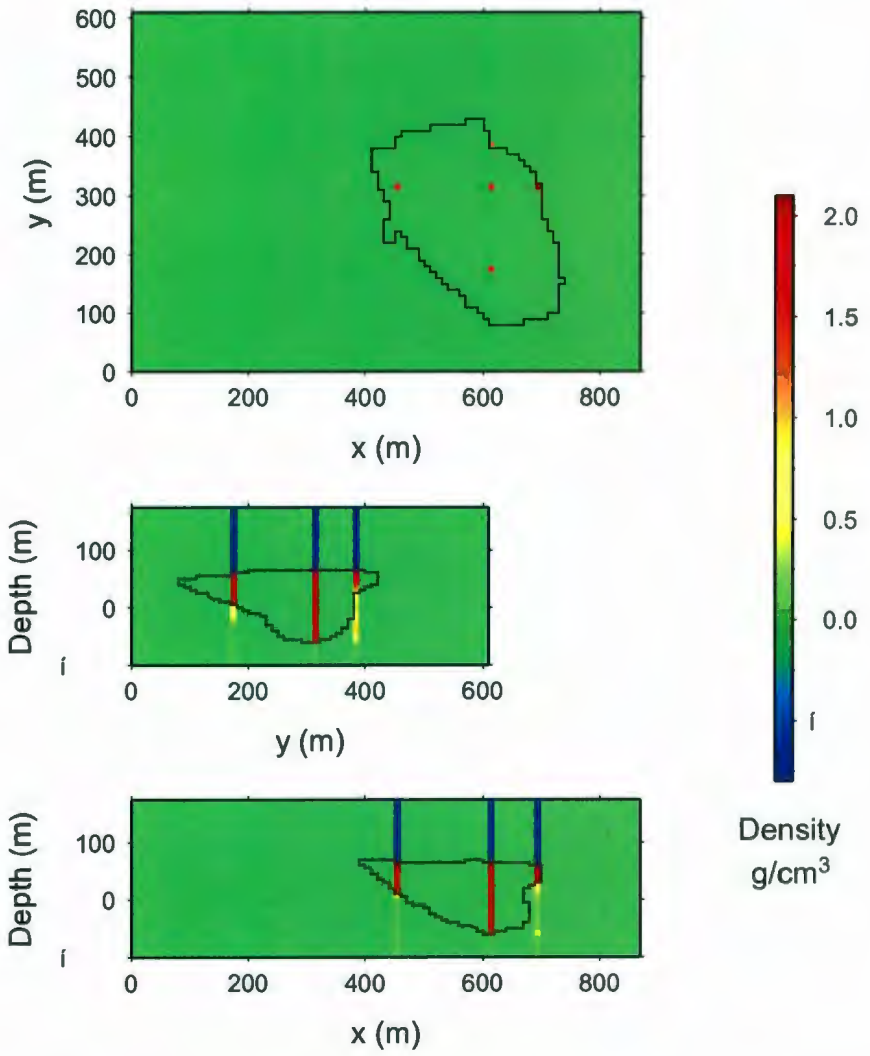

Figure 43. The reference model DM09 of density for cells positioned adjacent to the five borehole locations.

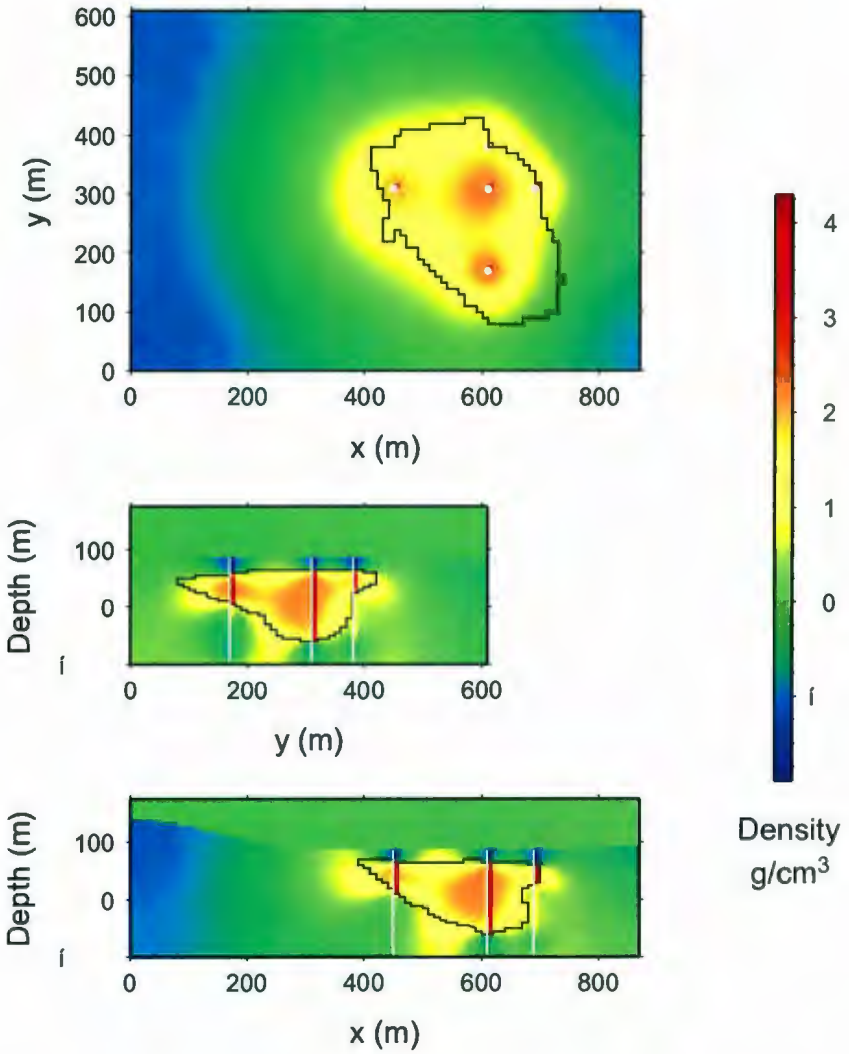

Figure 44. Inversion results for the Ovoid model of gravity data from five boreholes applying the reference model DM09. *top*: the z–slice, $z = 37$ m, *middle*: the y–slice, $x = 600$ m; *bottom*: the x–slice, $y = 600$ m. Borehole locations are displayed in white. The true massive sulphide Ovoid model is outlined in black.

6.10 Five Boreholes, reference model DM09 $\alpha_s = 1$ with weighting

To ensure the reference model densities are allocated to the proper cells with the appropriate value, the following inversion uses the borehole reference model and incorporates a weighting file. The borehole weighting file includes entries of 100 for cells that are positioned along the lengths of the boreholes and values of 1 for all other cells. In the inversion, data is from the same five boreholes as previous inversions and a coefficient value of $\alpha_s = 1$ is used. The resulting inversion density model is seen in Figure 45.

By incorporating the weighting file, the produced model differs greatly from the one shown in Figure 44. The weighting file does force the density next to the borehole to hold its initial reference model value, however, the density distribution throughout the rest of the produced model does not correlate and is different in shape and value from the true Ovoid model. This could be due to the relatively high coefficient value of $\alpha_s = 1$, which may have too greatly influenced the inversion to produce a model that coincides with the reference model. The parameters produced from the inversion are as follows,

- $\rho_{max} = 4.46$ g/cm^3
- $\rho_{min} = -2.69$ g/cm^3
- $\beta = 0.425E-08$
- $\phi_d = 367$
- $\phi_m = 0.27E+13$
- $\Phi = 11746.$

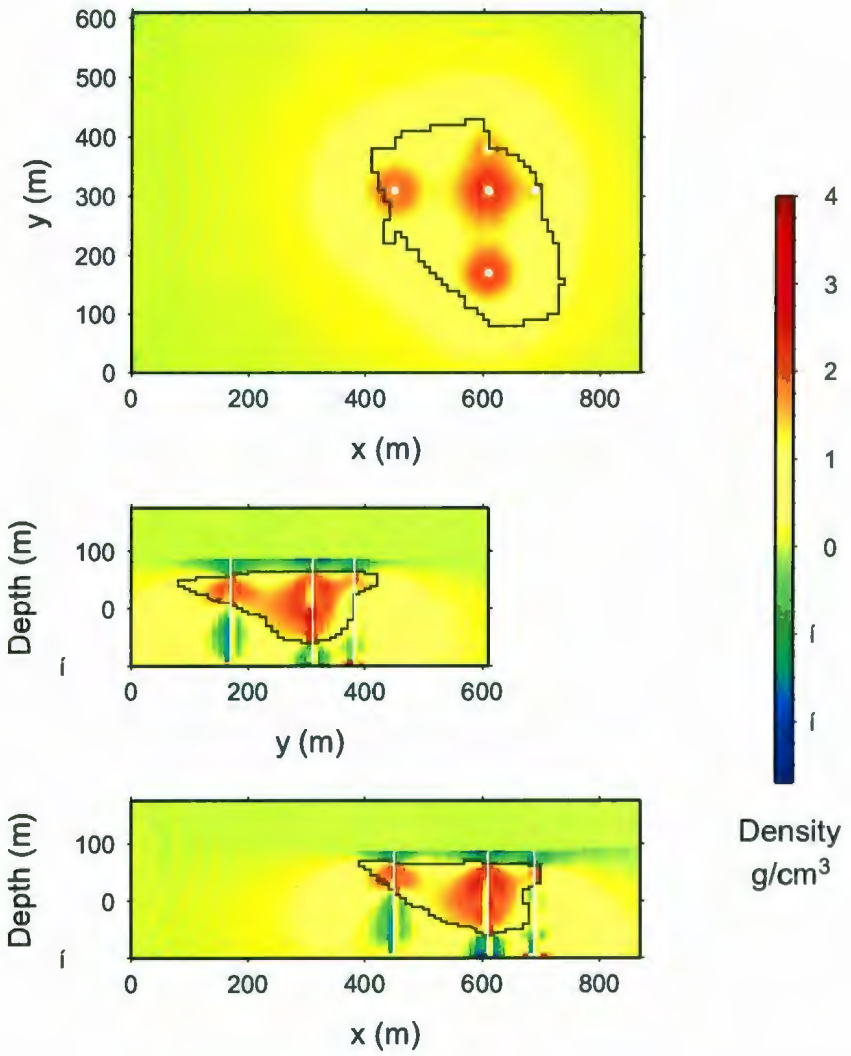

Figure 45. Inversion results for the Ovoid model of gravity data from five boreholes applying the reference model DM09, a parameter value of $\alpha_s = 1$ and extra weighting for cells along the boreholes. *top*: the x–slice, *middle*: the y–slice; *bottom*: the z–slice. Borehole locations are displayed in white. The true block model is outlined in black.

6.11 Five Boreholes, reference model DM09, $\alpha_s = 0.1$ with weighting

For the past example it was suggested that the poor model could have been due to the high value of the coefficient $\alpha_s = 1$ having too large of an influence on the inversion. In the next example, the exact same scenario is examined, however the α_s coefficient is changed to $\alpha_s = 0.1$. This inversion involves the same data and borehole weighting used in the previous example. The α_s value is lowered so that the inversion will be less inclined to produce a model so similar to the reference model. The resulting density distribution from this inversion example is seen in Figure 46.

As seen in the density distribution, changing the value of α_s from 1 to 0.1 does little to produce a model which compares to the true model. In fact, despite a minimal improvement in the peak density values, the produced density models shown in Figures 45 and 46 resemble each other. The parameters produced from the inversion are as follows,

- $\rho_{max} = 4.24$ g/cm^3
- $\rho_{min} = -2.4$ g/cm^3
- $\beta = 0.40E-07$
- $\phi_d = 363$
- $\phi_m = 0.28E+12$
- $\Phi = 11416.$

6.12 Five Boreholes, reference model DM09 $\alpha_s = 0.0001$ increased weighting

In a final effort to obtain an acceptable density model from an inversion which involves the borehole density reference model, the parameters are once again altered. The model structure coefficient is changed to $\alpha_s = 0.0001$, meaning that the inversion has little influence to produce a model which resembles the reference model. Also, the borehole weighting is changed where values for cells along the borehole had been 100 are switched to 10,000, the weighting for all other cells in the mesh remains 1. This means that, despite the little influence the inversion has to replicate the entire reference model, the inversion is strongly encouraged to allocate the densities along the boreholes

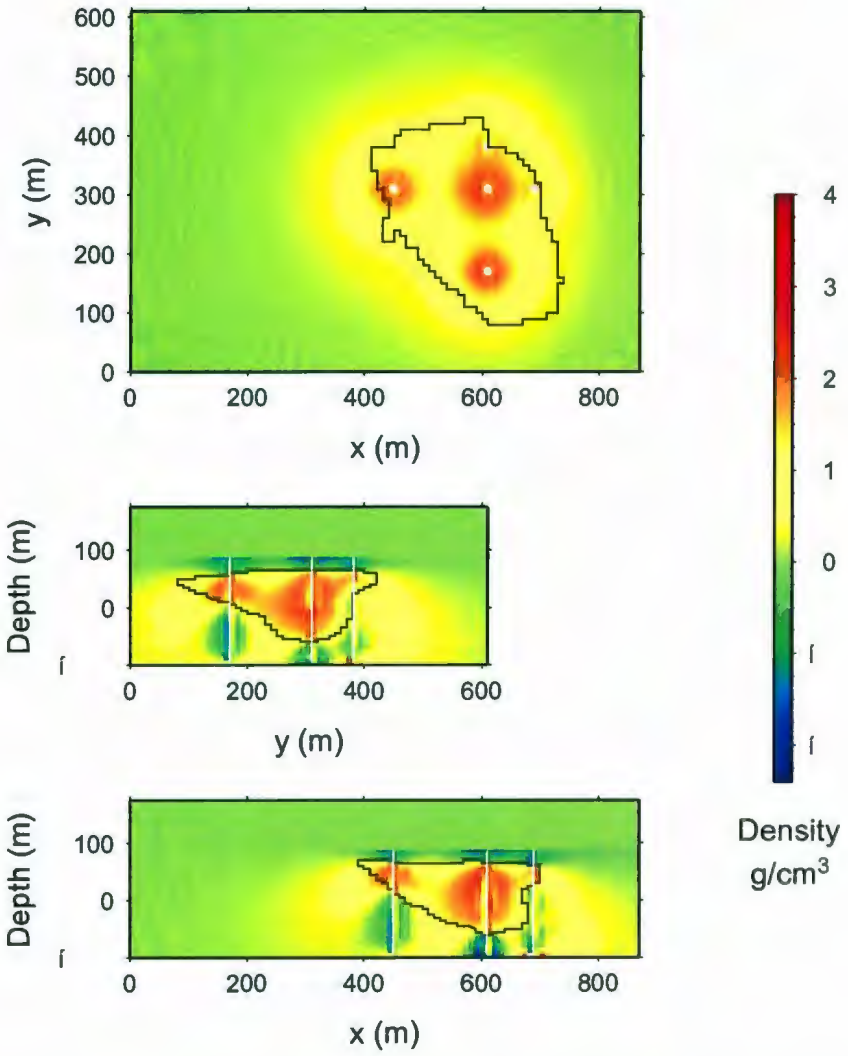

Figure 46. Inversion results for the Ovoid model of gravity data from five boreholes applying the reference model DM05, a parameter value of $\alpha_s = 0.1$ and extra weighting for cells along the boreholes. *top*: the z–slice, $z = 37$ m, *middle*: the y–slice, $x = 600$ m; *bottom*: the x–slice, $y = 600$ m. Borehole locations are displayed in white. The true massive sulphide Ovoid model is outlined in black.

to those cells. Again, the data used in the inversion is from the same five borehole locations as previously. The results from the completed inversion are seen in Figure 47 and the parameters produced from the inversion are as follows,

- $\rho_{max} = 4.38$ g/cm^3
- $\rho_{min} = -4.54$ g/cm^3
- $\beta = 0.38E-06$
- $\phi_d = 367$
- $\phi_m = 0.38E+11$
- $\Phi = 14350.$

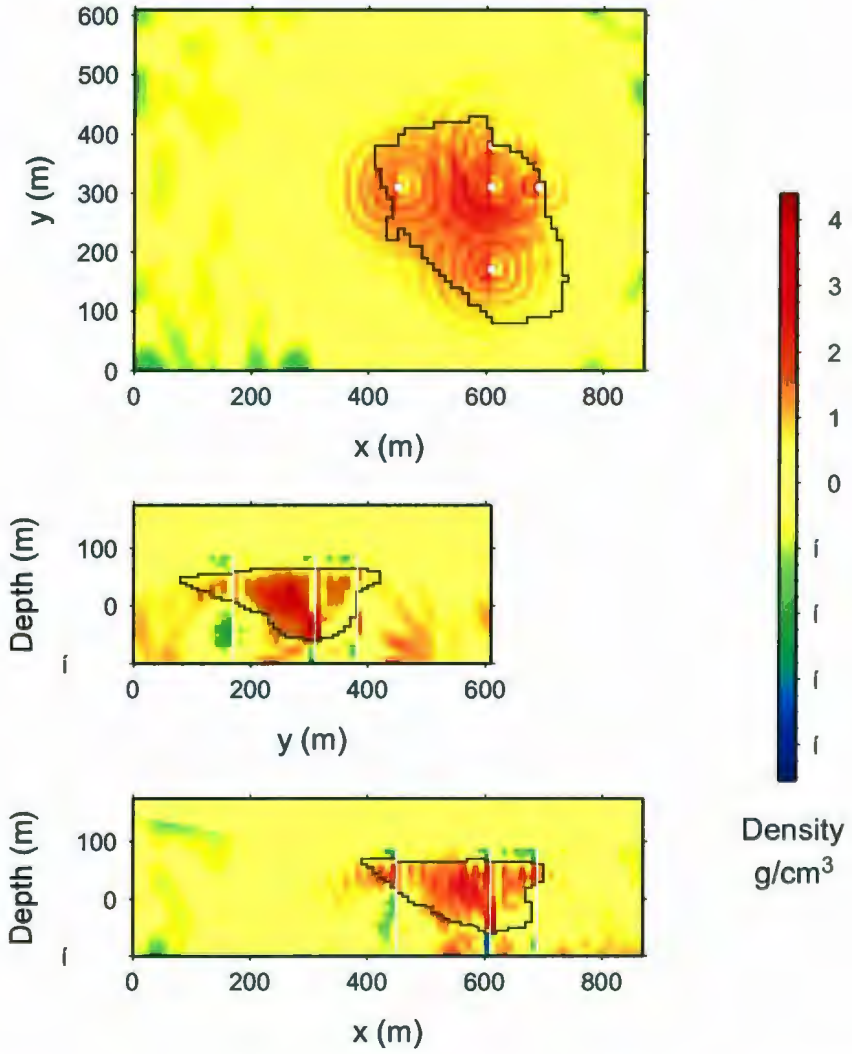

Figure 47. Inversion results for the Ovoid model of gravity data from five boreholes applying the reference model DM05, a parameter value of $\alpha_s = 0.0001$ and extra weighting for cells along the boreholes. *top*: the x–slice, *middle*: the y–slice; *bottom*: the z–slice. Borehole locations are displayed in white. The true block model is outlined in black.

The produced model is another failed attempt to recreate the density distribution and shape of the true Ovoid model. In fact, the results from the recent set of inversions involving the borehole density reference model demonstrate the issues peculiar and particular to minimum–structure borehole gravity inversion. It was initially thought that the inclusion of the borehole density reference model would provide useful subsurface information into the inversion to help produce a model which more accurately correlated with the true Ovoid model. This, however, was not the case and all the reproduced density models were of poorer results than, for example, the simple case shown in Figure 35.

It is speculated that the appearance of the reference model in all terms in the measure of model structure (equation (41)) is the cause of the disappointing results described in these sections. The jump in densities in the reference model between cells down the boreholes and then away from the boreholes still strongly influences equation (41) irrespective of the value of α_s (Section 3.2.2). Unfortunately, it was not possible to test this hypothesis because the starting model m_0 of equation (41) cannot be removed from the derivative terms in the program $g3dfd$ in its current form.

It has been examined that the density models produced by the inversion differ depending on the amount of data, the size of mesh and cells, and the density distribution and shape of the true model. While minimum–structure inversion has significant flexibility in that many different parameters can be adjusted and additional reference model and weighting files can be incorporated, these adjustments are done in an ad-hoc manor, and may not produce better results; sometimes a simpler approach will produce an overall better density model.

CHAPTER 7

Conclusion

The following final chapter summarizes the studies performed and results obtained throughout the previous chapters. This includes the use of a finite–difference approximation of Poisson's equation as a forward solving device and the use of borehole gravity data in minimum–structure inversions for a block–in–a–halfspace, wedge–in–a–halfspace, and the main Ovoid of Voisey's Bay Nickel Mine as models. This chapter also discusses the impact that borehole gravity measurement inversion will have on the mineral exploration industry and concludes with recommendations for future work.

7.1 Forward Modelling

One major obstacle for using borehole gravity in minimum–structure inversions was that a new method to forward model gravity data was needed. This was due to the fact that current day inversion programs are unable to take measurements within the confines of a dense anomaly. To solve this problem, the inversion program designed by Farquharson applies a forward modeller for gravity calculations by means of a finite–difference approximation to Poisson's equation. This method was chosen due to its minimalist use of computational memory. An in depth description of the method is presented in Chapter 2 and in Farquharson and Mosher (2009). Because the method uses an approximation of Poisson's equation, testing was necessary to validate the method. Borehole gravity data calculated at identical locations for a dense cube were compared between the finite–difference approximation method and the algorithm of Okabe – Steiner and Zilahi-Sebess presented by Li and Chouteau (1998). In Chapter 2, three borehole locations at various distances from the cube were observed for four cube meshes each of size 600 m^3, but with varying cell sizes. The finite–difference method proved to emulate the Li and Chouteau (1998) method in measurement and trend, and less deviation occurred

between measurements as cell size in the mesh decreased. A cumulative error measurement was performed for all four mesh sizes. It was determined that the finite–difference approximation to Poisson's equation was a viable method to forward model gravity data for a mesh which exhibited cell sizes of $10 \times 10 \times 10$ m or $5 \times 5 \times 5$ m. The other two meshes studied of $50 \times 50 \times 50$ m and $25 \times 25 \times 25$ m cell sizes still adequately fit the data trend, however inaccuracies around the peak gravity values discouraged their use. The finite–difference approximation of Poisson's equation was used as the forward modelling method in all of the minimum–structure inversions presented in this thesis.

7.2 Block–in–a–halfspace

The first series of inversions performed aimed to recover a dense cube in a zero–halfspace by use of various scenarios of borehole and surface data. The obtained results varied with some scenarios producing adequate representations of the true model density distribution and structure while others lacked any kind of spatial resolution. It is observed that inclusion of borehole gravity data is able to provide the inversion with correct depth resolution, however a sole borehole lacks spatial resolution in the xy–plane. Generally, boreholes located closer to the dense block provided more successful results and greater resolution, with the best occurring when borehole data located directly through the middle of the dense block is incorporated into the inversion. Contrarily, inversions that involved borehole data far away from the center of density provided the poorest results as the borehole data had little influence on creating the density distribution with resolution. The combination of surface data and borehole data directed directly through the dense block provided the best results as the model exhibited proper depth and spatial resolution with an accurate density representation of the dense block and zero–halfspace background. The l_1 style inversions were able to reproduce an image of the true dense block with accurately matching density distribution and shape that exhibit sharp interfaces between cells.

7.3 Wedge–in–a–halfspace

While the block–in–a–halfspace provided an initial test of a simple and symmetric model, inversions were next studied for a more complex wedge–in–a–halfspace model, non–symmetric about the middle of the x–axis. Similar borehole scenarios as the block–in–a–halfspace example were studied. Once again, the boreholes located far from the center of mass proved to be of little use in recreating the boundaries of the dense wedge. A borehole located through the center of the wedge proved to over power the influence of the boreholes positioned further away. Inversions were then performed for boreholes located on the edges of the true model. The use of the outer boreholes on the edge and central borehole were able to adequately reproduce the tapering shape of the wedge. Favourable results were also obtained without use of the central borehole data. The use of surface data with the outer edge borehole data provided the best result as the produced model matched the density distributions both in and outside of the wedge with proper depth resolution correlating with the non–symmetry of the model. The l_1 style inversions were able to reproduce an image of the true dense wedge with accurately matching density distribution and shape that exhibit sharp interfaces between cells.

7.4 Voisey's Bay Ovoid

The next set of inversions were aimed at reproducing the main ovoid of the Voisey's Bay Nickel Mine. The true model used to forward model the gravity data was created with data collected from over 500 actual boreholes. The inversions incorporated the data from five boreholes, one central borehole located through the center of mass where the ovoid extended the furthest in depth, and four other boreholes positioned on the edges of the Ovoid. From the produced inversion model, it was noted that the parameters of the depth weighting function outlined in Chapter 3 required alteration. In particular, the manipulation of $\tilde{\beta}$, in equation (43), greatly influenced the outcome of the inversion. It was concluded that if the value of $\tilde{\beta}$ is too large, the produced models exhibited

unexpectedly low density values in cells adjacent to the borehole locations with higher densities between the boreholes, even in situations where the borehole location passes directly through the dense mass. Counterintuitively, if the value of the depth weight parameter $\tilde{\beta}$ is too low, the outcome models exhibited high density values limited to cells around the borehole, with little to no high density values spread between boreholes.

Another scenario studied for the Ovoid included the use of four boreholes, eliminating the central borehole data from the inversion. The resulting density model proved to be a poor representation as it lacked the proper density distribution throughout the center of the Ovoid. The inclusion of the limited surface data improved the model, although improvement was minimal for the four borehole example.

Methods to include a priori knowledge of the Voisey's Bay area were also included into inversions for the Ovoid. A reference model of the overburden densities was incorporated and the resulting density model limited the spreading of high density values outside of the area above the Ovoid in the true model providing an accurate constraint at the top of the anomaly and a better density distribution throughout. A reference model incorporating the densities for cells along the lengths of the boreholes was also incorporated into inversions which aimed to simulate the densities recovered through logging of the core or through a gamma ray survey. The inversion results from this scenario provided models of little quality and outlined the potential peculiarity of altering parameters in minimum–structure inversions.

7.5 Final Statements

The scenarios studied from the multiple inversion trials were performed to create a basis on the type of information that borehole gravity calculations and inversions are able to provide. The inversion of borehole gravity data is able to produce a proper density resolution for a dense anomaly, however lacks spatial resolution in the xy–plane. The more successful inversion results arise from the use of both surface and borehole

data. The benefits of borehole gravity data also depend on the location of the borehole relative to the anomalous mass. When close enough, inversions which reproduce images of more complex density distribution are attainable as seen with the wedge and Ovoid models. Borehole data which is located further away from the model constrains the outer parts of the domain. Ideally, a borehole oriented through the center of mass is preferred, while other boreholes positioned to outline the dense area confine the density and reproduce a greater resolution of an anomaly.

Upon the completion of the borehole gravimeter, the use of minimum structure borehole gravity inversion will be a valuable tool that has the possibility to aid in various aspects of mining and, with the appropriate data, can provide accurate information regarding an anomaly's shape with proper depth resolution and density distribution.

7.6 Future Work

A main area of future work proposed for this study is performing minimum structure inversions with data recorded by a functional slimhole gravimeter from an actual survey of a mining site. With this, inversion examples can be studied which exhibit real life density distribution from data which contains real noise.

Bibliography

Ash, M. R. (2007). Constrained inversion of gravity data over the ovoid and mini-ovoid in the voiseys bay ni-cu-co deposit, labrador. M. sci. thesis, Memorial University of Newfoundland.

Barnett, C. T. (1976). Theoretical modeling of the magnetic and gravitational fields of an arbitrarily shaped three-dimensional body. *Geophysics*, **41**:1353 1364.

Bear, G. W., Al-Shukri, H. J., and Rudman, A. J. (1995). Linear inversion of gravity data for 3 d density distributions. *Geophysics*, **60**:1354 1364.

Blakely, R. J. (1996). *Potential Theory in Gravity and Magnetic Applications*. Cambridge University Press.

Boulanger, O. and Chouteau, M. (2001). Constraints in 3d gravity inversion. *Geophysical Prospecting*, **49**:265–280.

Chasseriau, P. and Chouteau, M. (2003). 3d gravity inversion using a model of parameter covariance. *Journal of Applied Geophysics*, **52**:59 74.

Coggon, J. H. (1976). Magnetic and gravity anomalies of polyhedra. *Geoexploration*, **14**:93 105.

Constable, S. C., Parker, R. L., and Constable, C. G. (1987). Occam's inversion: A practical algorithm for generating smooth models from electromagnetic sounding data. *Geophysics*, **52**:289–300.

de Groot-Hedlin, C. and Constable, S. (1990). Occam's inversion to generate smooth, two-dimensional models from magnetotelluric data. *Geophysics*, **55**:1613 1624.

EDCON, Inc. (1990). Introduction to borehole gravity. [Online]. Available: http://edcon-prj.com/introbhg.htm.

Farqharson, C. G. and Oldenburg, D. W. (1998). Nonlinear inversion using general measures of data misfit and model structure. *Geophysical Journal International*, **134**:213–227.

Farquharson, C. G. (2008). Constructing piecewise-constant models in multidimensional minimum-structure inversions. *Geophysics*, **73**:K1–K9.

Farquharson, C. G., Ash, M. R., and Miller, H. G. (2008). Geologically constrained gravity inversion for the voisey's bay ovoid deposit. *The Leading Edge*, **27**:64–69.

Farquharson, C. G. and Mosher, C. R. W. (2009). Three-dimensional modelling of gravity data using finite differences. *Journal of Applied Geophysics*, in press (DOI: 10.1016/j.jappgeo.2009.03.007).

Farquharson, C. G. and Oldenburg, D. W. (2003). Constructing piece-wise-constant models using general measuresin non-linear, minimum-structure inversion algorithms. In *6th International Symposium, Society of Exploration Geophysicists of Japan, Expanded Abstracts*, pages 240–243.

Giroux, B., Chouteau, M., Seigel, H. O., and Nind, C. J. M. (2007). A program to model and interpret borehole gravity data. In *Exploration07: Fifth Decennial International Conference on Mineral Exploration*, pages 1111–1114.

Gotze, H. J. and Lahmeyer, B. (1988). Application of three-dimensional interactive modeling in gravity and magnetics. *Geophysics*, **53**:1096–1108.

GRAV3D (2007). Grav3d manual. [Online]. Available: http://www.eos.ubc.ca/ubcgif/.

Green, W. R. (1975). Inversion of gravity profiles by use of a backus–gilbert approach. *Geophysics*, **40**:763–772.

Guillen, A. and Menichetti, V. (1984). Gravity and magnetic inversion with minimization of a specific functional. *Geophysics*, **49**:1354 1360.

Haáz, I. B. (1953). Relation between the potential of the attraction of the mass contained in a finite rectangular prism and its first and second derivatives. *Geofizikai Kzlemenyek*, **2**(7):(in Hungarian).

Hammer, S. (1950). Density determinations by underground gravity measurements. *Geophysics*, **15**:637–652.

Jung, K. (1961). *Schwerkraft verfahren in der Angewandten Geophysik*. Akademisches Verlag, Leipzig, Germany.

Kellogg, O. D. (1967). *Foundations of Potential Theory*. Springer-Verlag.

LaFehr, T. R. (1983). Rock density from borehole gravity surveys. *Geophysics*, **48**:341 356.

Last, B. J. and Kubik, K. (1983). Compact gravity inversion. *Geophysics*, **48**:713 721.

Li, X. and Chouteau, M. (1998). Three-dimensional gravity modeling in all space. *Surveys in Geophysics*, **19**:339 368.

Li, Y. and Oldenburg, D. W. (1996). 3-d inversion of magnetic data. *Geophysics*, **54**:200 215.

Li, Y. and Oldenburg, D. W. (1998). 3-d inversion of gravity data. *Geophysics*, **63**:109 119.

Li, Y. and Oldenburg, D. W. (2000). Joint inversion of surface and three-component borehole magnetic data. *Geophysics*, **65**:540 552.

Li, Y. and Oldenburg, D. W. (2003). Fast inversion of large-scale magnetic data using wavelet transforms and a logarithmic barrier method. *Geophysical Journal International*, **152**:251 265.

Loke, M. H., Acworth, I., and Dahlin, T. (2003). A comparison of smooth and blocky inversion methods in 2d electrical imaging surveys. *Exploration Geophysics*, **34**:182 187.

Mackie, R. L. and Madden, T. R. (1993). Three-dimensional magnetotelluric inversion using conjugate gradients. *Geophysics Journal International*, **115**:215 229.

Nabighian, M. N., Ander, M. E., Grauch, V. J. S., Hansen, R. O., LaFehr, T. R., Li, Y., Pearson, W. C., Peirce, J. W., Phillips, J. D., and Ruder, M. E. (2005). Historical development of the gravity method in exploration. *Geophysics*, **70**:63ND 89ND.

Nagihara, S. and Hall, S. A. (2001). Three-dimensional gravity inversion using simulated annealing: Constraints on the diapiric roots of allochthonous salt structures. *Geophysics*, **66**:1438 1449.

Nagy, D. (1966). The gravitational attraction of a right rectangular prism. *Geophysics*, **31**:362 371.

Naldrett, A. J., Keats, H., Sparks, K., and More, R. (1996). Geology of the voiseys bay ni-cu-co deposit, labrador, canada. *Exploration and Mining Geology*, **5**:169 179.

Nind, C., Seigel, H. O., Chouteau, M., and Giroux, B. (2007). Development of a borehole gravimeter for mining applications. *First Break*, **25**:71 77.

Okabe, M. (1979). Analytical expressions for gravity anomalies due to homogeneous polyhedral bodies and translations into magnetic anomalies. *Geophysics*, **44**:730 741.

Oldenburg, D. W. and Li, Y. (1994). Inversion of induced polarization data. *Geophysics*, **59**:1327–1341.

Pedersen, L. B. (1979). Constrained inversion of potential field data. *Geophysical Prospecting*, **27**:726–748.

Plouff, D. (1976). Gravity and magnetic fields of polygonal prisms and application to magnetic terrain corrections. *Geophysics*, **41**:727–741.

Portniguine, O. and Zhadov, M. S. (1999). Focusing geophysical inversion images. *Geophysics*, **64**:874–887.

Reynolds, J. M. (2005). *An Introduction to Applied and Environmental Geophysics, 6th edt.* John Wiley & Sons Ltd., West Sussex, England.

Rodi, W. and Mackie, R. L. (2001). Nonlinear conjugate gradients algorithm for 2–d magnetotelluric inversion. *Geophysics*, **115**:215–229.

Saad, Y. (2003). Iterative methods for sparse linear systems. *SIAM.*

Scintrex (2009). Cg-5 scintrex autograv system operation manual. [Online]. Available: http://www.scintrexltd.com/documents/CG-5Rev4.pdf.

Singh, B. and Guptasarma, D. (2001). New method for fast computation of gravity and magnetic anomalies from arbitrary polyhedral. *Geophysics*, **66**:521–526.

Smith, J. T. and Booker, J. R. (1988). Magnetotelluric inversion for minimum structure. *Geophysics*, **53**:1565–1576.

Smith, N. J. (1950). The case for gravity data from boreholes. *Geophysics*, **15**:605–636.

Soronkin, L. V. (1951). *Gravimetry and Gravimetrical Prospecting.* State Technology Publishing, Moscow. (in Russian).

Steiner, F. and Zilahi-Sebess, L. (1988). *Interpretation of Filtered Gravity Maps.* Akademiai Kiado, Budapest, Hungary.

Telford, W. M., Geldart, L. P., and Sherriff, R. E. (1990). *Applied Geophysics.* Cambridge University Press, New York.

VBNC (2009). Voisey's bay development. [Online]. Available: http://vinl.valeinco.com/.

Zhang, J., Wang, C.-Y., Shiz, Y., Cai, Y., Chi, W.-C., Dreger, D., Cheng, W.-B., and Yuanzz, Y.-H. (2004). Three-dimensional crustal structure in central taiwan from gravity inversion with a parallel genetic algorithm. *Geophysics*, **69**:917 924.

APPENDIX A

Block in a halfspace models

In the following appendix, more inversion results are shown for different scenarios of borehole data and locations for a block in a halfspace model. The mesh used in the block density model and for results has dimensions $(x, y, z) \rightarrow (0, 0, 150) : (600, 600, -450)$ and cell sizes of 10m in each direction. The mesh therefore contains 216,000 cells. A cube with a density of 2.0 g/cm^3 is located at the center of the mesh with coordinates, $(x, y, z) \rightarrow (250, 250, -100) : (350, 350, -200)$. The cells outside of the cube have a density of zero. The block density model is shown in Figure 7. All borehole data observation points are calculated along boreholes which travel from $(z) \rightarrow (-3.846 : -296.153)$ m. A total of thirty nine observations are taken at evenly spaced intervals at approximately every 7.7 m. Random Gaussian noise of standard deviation equal to five percent of the magnitude of the datum is added to all data–sets. If surface data is included in the example, a total of 1521 data points are taken at the surface ($z = 0$) from $(x, y) \rightarrow (105.13, 105.13) : (494.87, 494.87)$ m. Thus measurements are calculated at approximately every 10.25 m.

A.1 One + Surface Data Far

The resulting density distribution and output parameters from an inversion of data calculated at the surface and a borehole located at $(x, y) \rightarrow (150, 300)$.

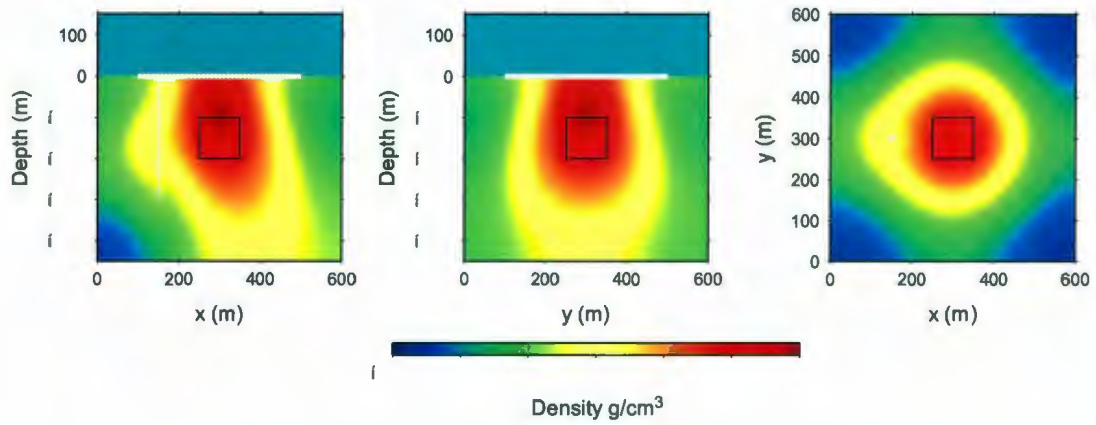

Figure A.1. Inversion results for a block–in–a–halfspace from surface data and a borehole. *left*: the x–slice, *middle*: the y–slice; *right*: the z–slice. Borehole location is displayed in white and the surface locations are displayed in white dots. The true block model is outlined in black.

- $\rho_{max} = 0.0986$ g/cm^3
- $\rho_{min} = -0.0106$ g/cm^3
- $\beta = 0.27500E - 02$
- $\phi_d = 1614.5$
- $\phi_m = 0.67830E + 06$
- $\Phi = 3479.8$

A.2 One + Surface Data Edge

The resulting density distribution and output parameters from an inversion of data calculated at the surface and a borehole located at $(x, y) \rightarrow (250, 300)$.

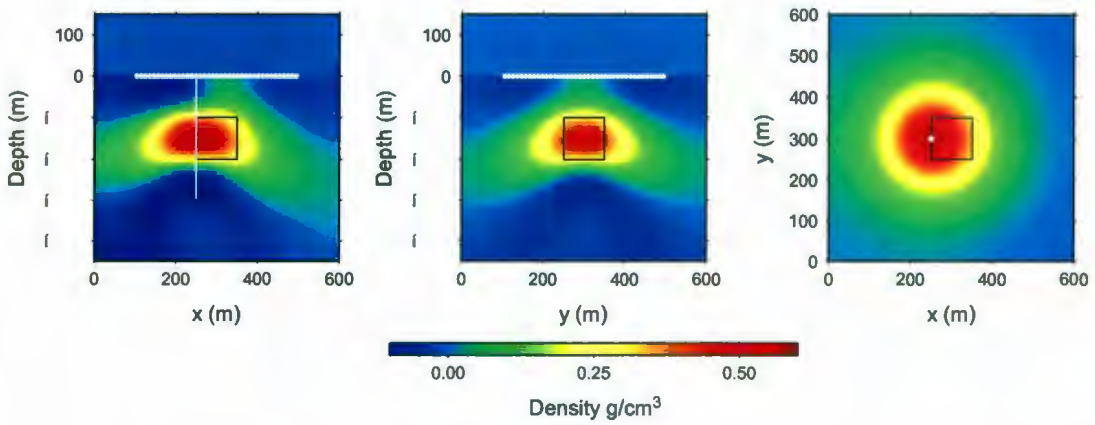

Figure A.2. Inversion results for a block–in–a–halfspace from surface data and a borehole. *left*: the x–slice, *middle*: the y–slice; *right*: the z–slice. Borehole location is displayed in white and the surface locations are displayed in white dots. The true block model is outlined in black.

- $\rho_{max} = 0.587$ g/cm^3
- $\rho_{min} = -0.0946$ g/cm^3
- $\beta = 0.12000E - 03$
- $\phi_d = 1624.7$
- $\phi_m = 0.23009E + 08$
- $\Phi = 4385.8$

A.3 Two Edge

The resulting density distribution and output parameters from an inversion of data calculated from boreholes located at $(x, y) \rightarrow (250, 300)$ and $(x, y) \rightarrow (350, 300)$.

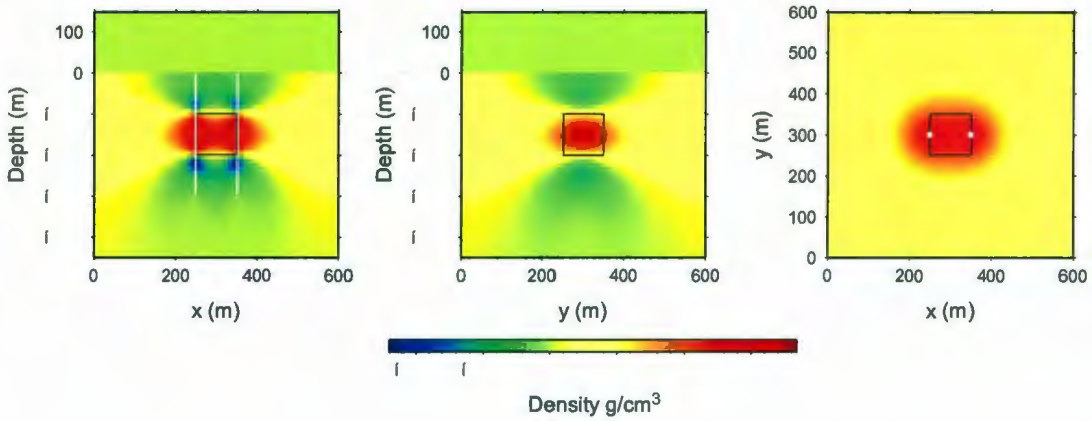

Figure A.3. Inversion results for a block–in–a–halfspace from two boreholes. *left*: the x–slice, *middle*: the y–slice; *right*: the z–slice. Borehole locations are displayed in white. The true block model is outlined in black.

- $\rho_{max} = 0.853$ g/cm^3
- $\rho_{min} = -0.531$ g/cm^3
- $\beta = 0.15000E - 05$
- $\phi_d = 85.166$
- $\phi_m = 0.39079E + 09$
- $\Phi = 671.36$

A.4 Two Edge, One Middle

The resulting density distribution and output parameters from an inversion of data calculated from boreholes located at $(x, y) \rightarrow (250, 300)$, $(x, y) \rightarrow (300, 300)$ and $(x, y) \rightarrow (350, 300)$.

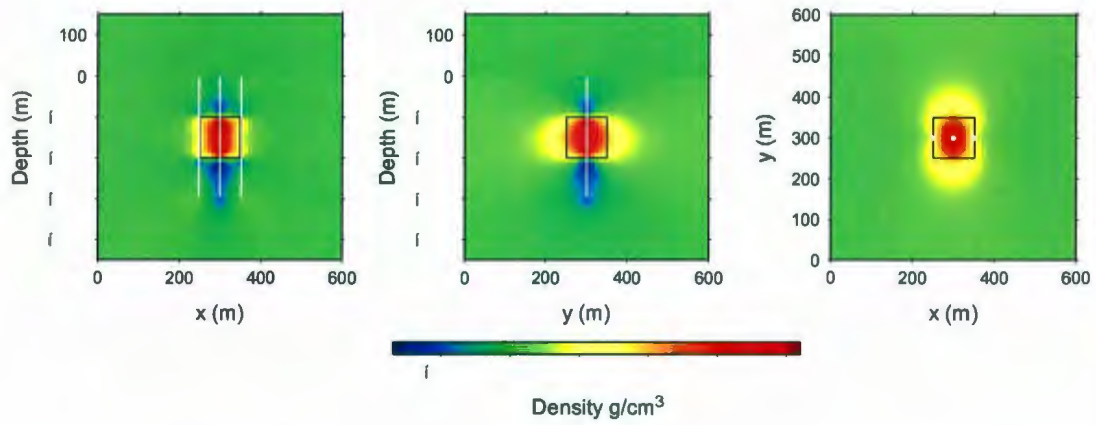

Figure A.4. Inversion results for a block–in–a–halfspace from two boreholes. *left*: the x–slice, *middle*: the y–slice; *right*: the z–slice. Borehole locations are displayed in white. The true block model is outlined in black.

- $\rho_{max} = 2.1$ g/cm^3
- $\rho_{min} = -0.821$ g/cm^3
- $\beta = 0.68000E - 06$
- $\phi_d = 114.98$
- $\phi_m = 0.10315E + 10$
- $\Phi = 816.37$

A.5 One Far, One Middle

The resulting density distribution and output parameters from an inversion of data calculated from boreholes located at $(x, y) \rightarrow (150, 300)$ and $(x, y) \rightarrow (300, 300)$.

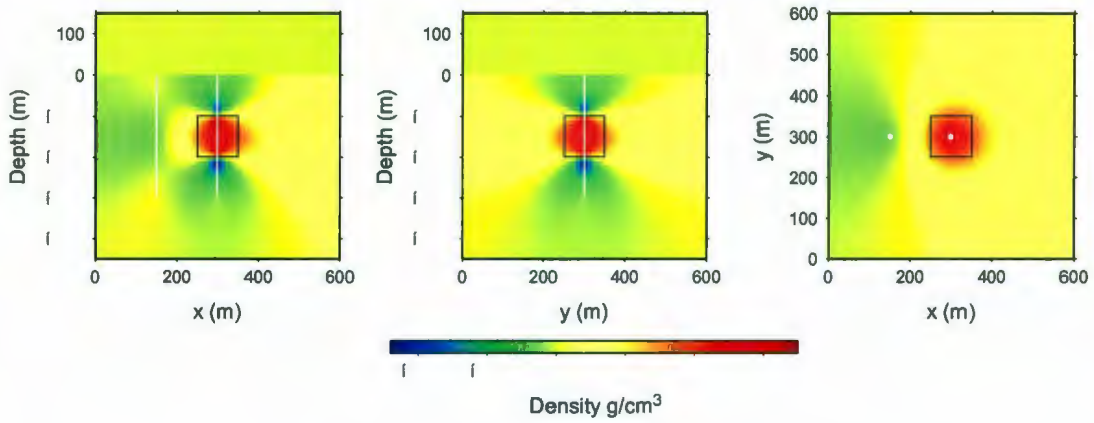

Figure A.5. Inversion results for a block–in–a–halfspace from two boreholes. *left*: the x–slice, *middle*: the y–slice; *right*: the z–slice. Borehole locations are displayed in white. The true block model is outlined in black.

- $\rho_{max} = 1.71$ g/cm^3
- $\rho_{min} = -1.16$ g/cm^3
- $\beta = 0.80000E - 06$
- $\phi_d = 84.491$
- $\phi_m = 0.84054E + 09$
- $\Phi = 756.92$

A.6 One Half, One Middle

The resulting density distribution and output parameters from an inversion of data calculated from boreholes located at $(x, y) \rightarrow (200, 300)$ and $(x, y) \rightarrow (300, 300)$.

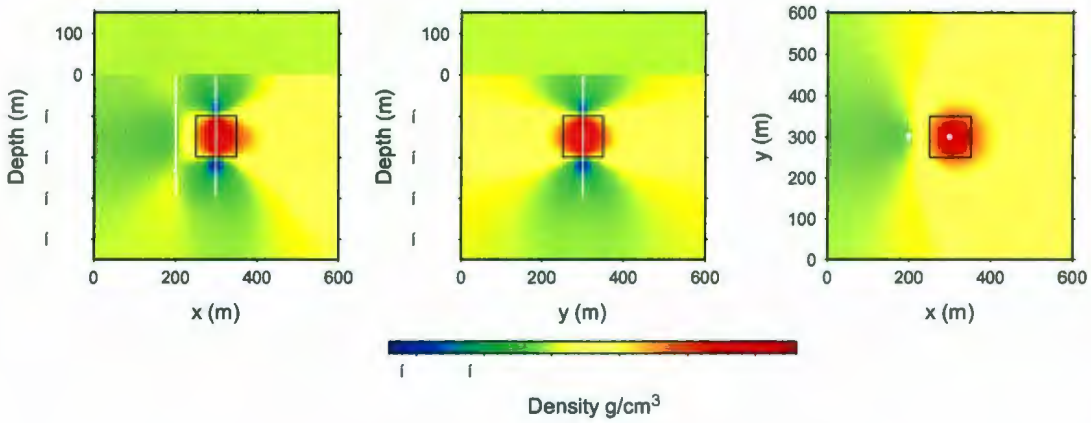

Figure A.6. Inversion results for a block–in–a–halfspace from two boreholes. *left*: the x–slice, *middle*: the y–slice; *right*: the z–slice. Borehole locations are displayed in white. The true block model is outlined in black.

- $\rho_{max} = 1.77$ g/cm^3
- $\rho_{min} = -1.16$ g/cm^3
- $\beta = 0.75000E - 06$
- $\phi_d = 77.071$
- $\phi_m = 0.85659E + 09$
- $\Phi = 719.51$

A.7 One Edge, One Middle

The resulting density distribution and output parameters from an inversion of data calculated from boreholes located at $(x, y) \rightarrow (250, 300)$ and $(x, y) \rightarrow (300, 300)$.

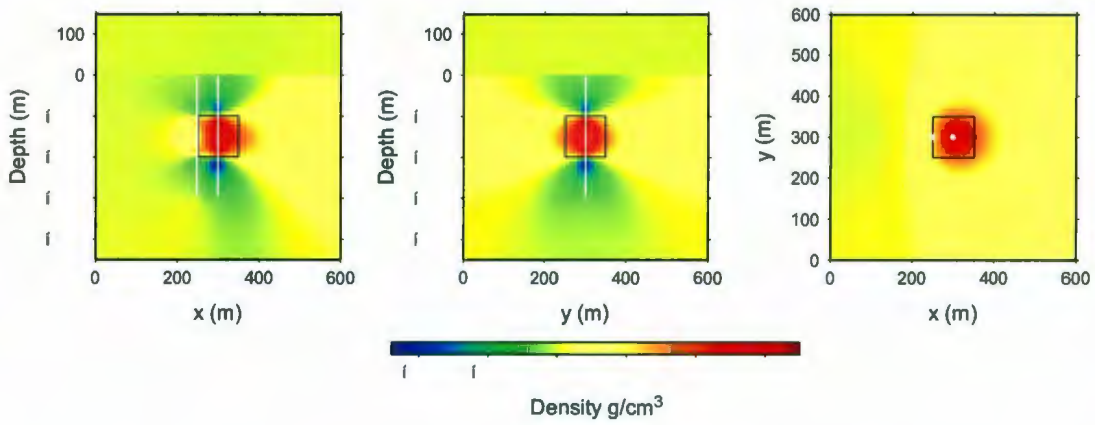

Figure A.7. Inversion results for a block–in–a–halfspace from two boreholes. *left*: the x–slice, *middle*: the y–slice; *right*: the z–slice. Borehole locations are displayed in white. The true block model is outlined in black.

- $\rho_{max} = 1.73$ g/cm^3
- $\rho_{min} = -1.18$ g/cm^3
- $\beta = 0.73000E - 06$
- $\phi_d = 84.377$
- $\phi_m = 0.85798E + 09$
- $\Phi = 710.70$

A.8 One Edge, One Half

The resulting density distribution and output parameters from an inversion of data calculated from boreholes located at $(x, y) \rightarrow (250, 300)$ and $(x, y) \rightarrow (400, 300)$

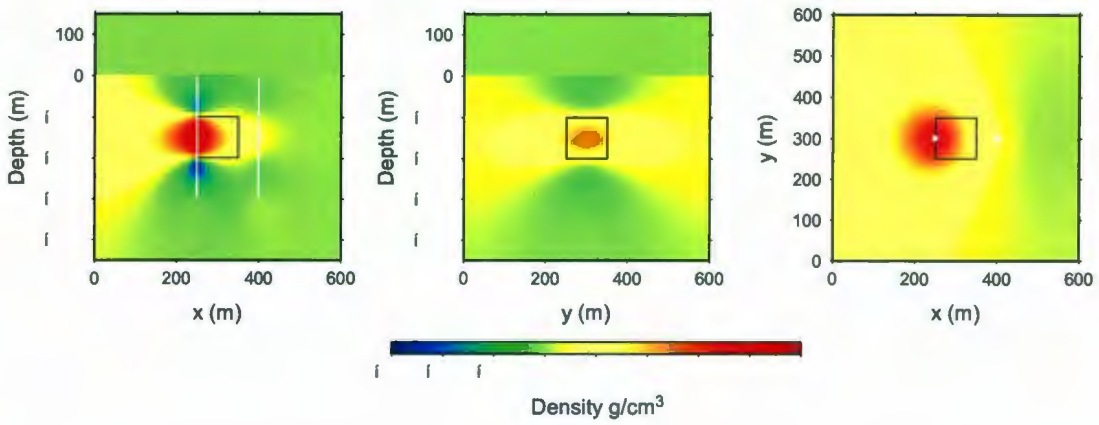

Figure A.8. Inversion results for a block–in–a–halfspace from two boreholes. *left*: the x–slice, *middle*: the y–slice; *right*: the z–slice. Borehole locations are displayed in white. The true block model is outlined in black.

- $\rho_{max} = 0.939$ g/cm^3
- $\rho_{min} = -0.503$ g/cm^3
- $\beta = 0.22000E - 05$
- $\phi_d = 77.909$
- $\phi_m = 0.23911E + 09$
- $\Phi = 603.96$

A.9 One Edge, One Half 2

The resulting density distribution and output parameters from an inversion of data calculated from boreholes located at $(x, y) \rightarrow (200, 300)$ and $(x, y) \rightarrow (250, 300)$

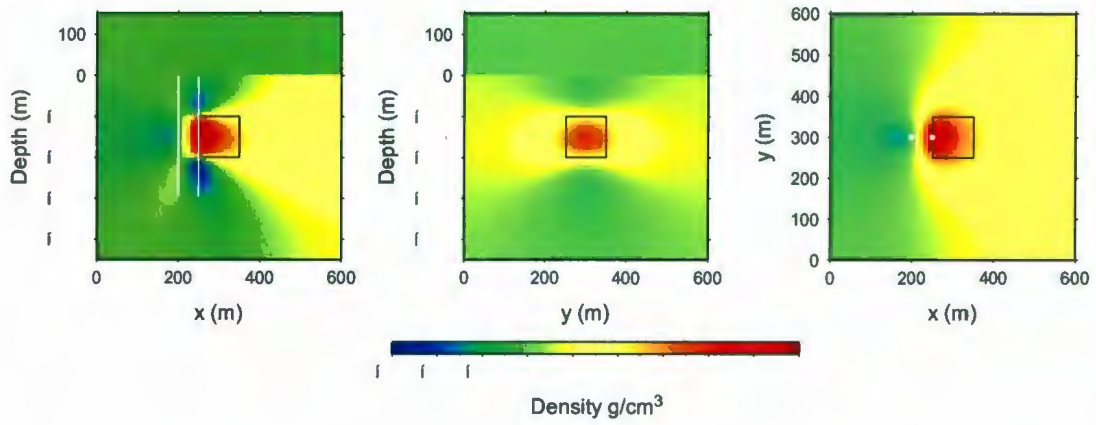

Figure A.9. Inversion results for a block–in–a–halfspace from two boreholes. *left*: the x–slice, *middle*: the y–slice; *right*: the z–slice. Borehole locations are displayed in white. The true block model is outlined in black.

- $\rho_{max} = 1.14$ g/cm^3
- $\rho_{min} = -0.571$ g/cm^3
- $\beta = 0.16500E - 05$
- $\phi_d = 82.971$
- $\phi_m = 0.34502E + 09$
- $\Phi = 652.25$

A.10 One Middle, Two Corner Edge

The resulting density distribution and output parameters from an inversion of data calculated from boreholes located at $(x, y) \rightarrow (300, 300)$, $(x, y) \rightarrow (250, 250)$ and $(x, y) \rightarrow (450, 450)$.

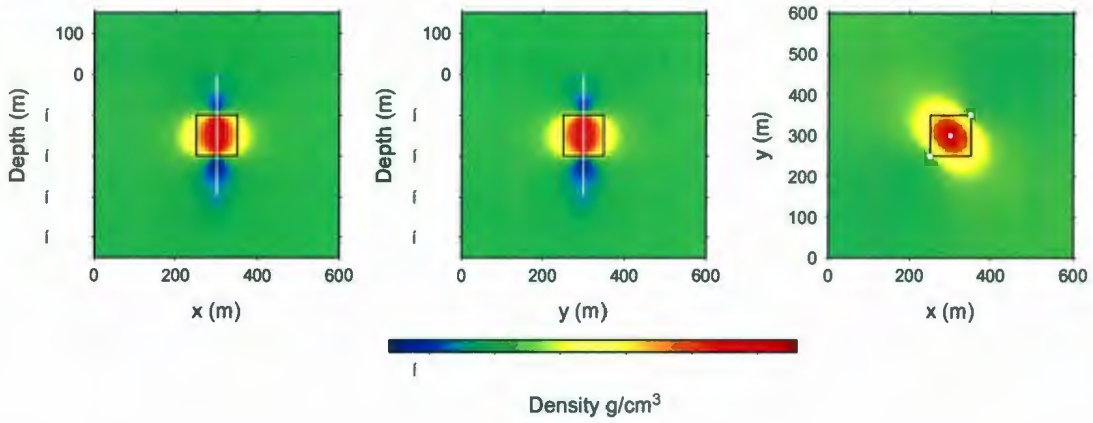

Figure A.10. Inversion results for a block–in–a–halfspace from three boreholes. *left*: the x–slice, *middle*: the y–slice; *right*: the z–slice. Borehole locations are displayed in white. The true block model is outlined in black.

- $\rho_{max} = 2.12$ g/cm^3
- $\rho_{min} = -0.787$ g/cm^3
- $\beta = 0.84000E - 06$
- $\phi_d = 123.31$
- $\phi_m = 0.10130E + 10$
- $\Phi = 974.20$

A.11 Five Boreholes

The resulting density distribution and output parameters from an inversion of data calculated from boreholes located at $(x, y) \rightarrow (150, 300)$, $(x, y) \rightarrow (300, 300)$, $(x, y) \rightarrow (450, 300)$, $(x, y) \rightarrow (300, 150)$ and $(x, y) \rightarrow (300, 450)$.

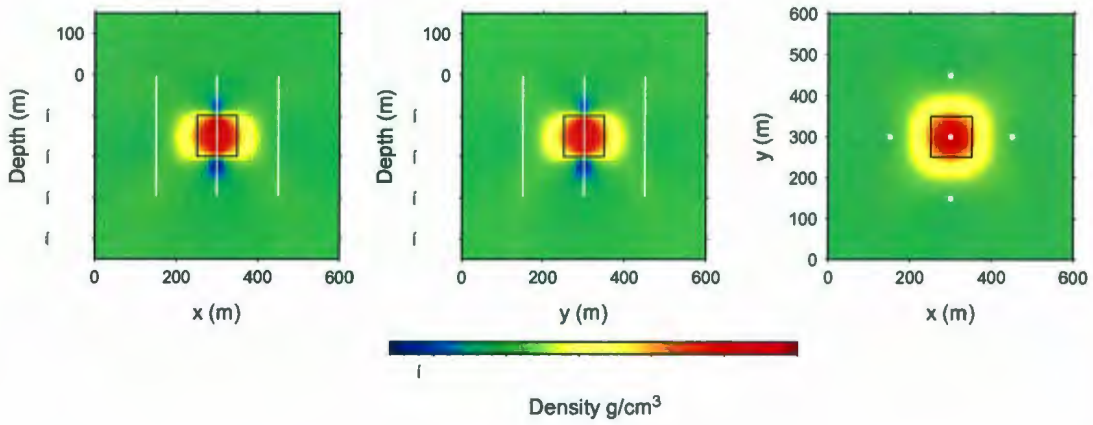

Figure A.11. Inversion results for a block–in–a–halfspace from five boreholes. *left*: the x–slice, *middle*: the y–slice; *right*: the z–slice. Borehole locations are displayed in white. The true block model is outlined in black.

- $\rho_{max} = 1.96$ g/cm^3
- $\rho_{min} = -0.732$ g/cm^3
- $\beta = 0.13000E - 05$
- $\phi_d = 186.81$
- $\phi_m = 0.99629E + 09$
- $\Phi = 1482.0$

A.12 Five Boreholes Line

The resulting density distribution and output parameters from an inversion of data calculated from boreholes located at $(x, y) \rightarrow (200, 300)$, $(x, y) \rightarrow (250, 300)$, $(x, y) \rightarrow (300, 300)$, $(x, y) \rightarrow (350, 300)$ and $(x, y) \rightarrow (400, 300)$.

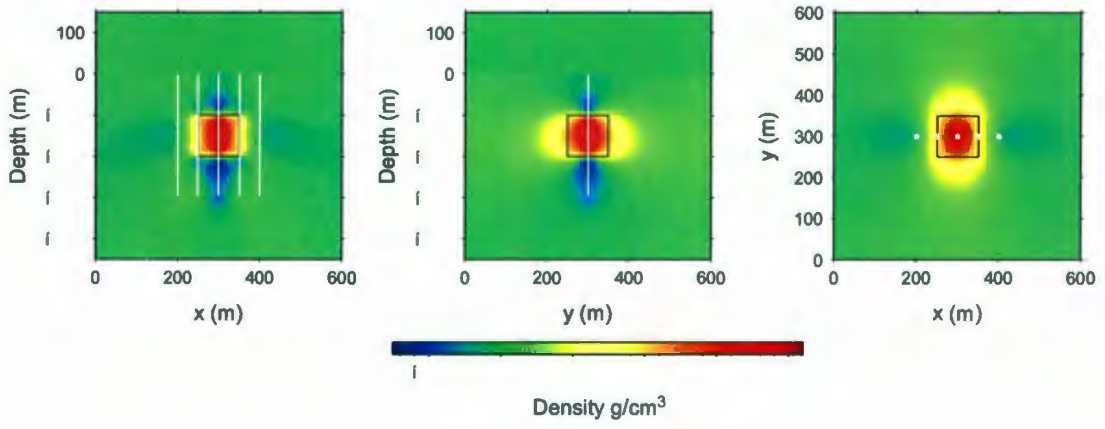

Figure A.12. Inversion results for a block–in–a–halfspace from five boreholes. *left*: the x–slice, *middle*: the y–slice; *right*: the z–slice. Borehole locations are displayed in white. The true block model is outlined in black.

- $\rho_{max} = 2.03$ g/cm^3
- $\rho_{min} = -0.706$ g/cm^3
- $\beta = 0.11000E - 05$
- $\phi_d = 185.66$
- $\phi_m = 0.10518E + 10$
- $\Phi = 1342.7$

A.13 Five Boreholes X

The resulting density distribution and output parameters from an inversion of data calculated from boreholes located at $(x, y) \rightarrow (150, 150)$, $(x, y) \rightarrow (150, 450)$, $(x, y) \rightarrow (300, 300)$, $(x, y) \rightarrow (450, 450)$ and $(x, y) \rightarrow (450, 150)$.

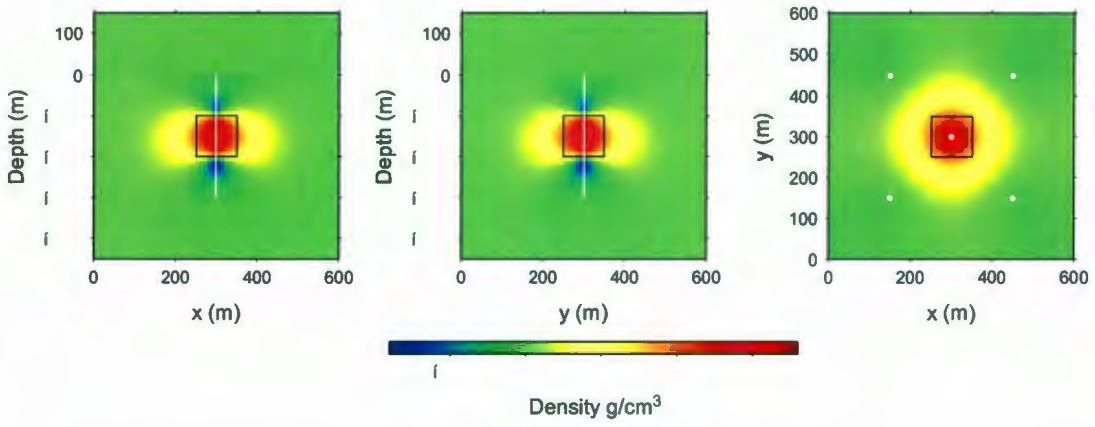

Figure A.13. Inversion results for a block–in–a–halfspace from five boreholes. *left*: the x–slice, *middle*: the y–slice; *right*: the z–slice. Borehole locations are displayed in white. The true block model is outlined in black.

- $\rho_{max} = 1.77$ g/cm^3
- $\rho_{min} = -0.837$ g/cm^3
- $\beta = 0.14000E - 05$
- $\phi_d = 203.50$
- $\phi_m = 0.93862E + 09$
- $\Phi = 1517.6$

A.14 Seven Boreholes Line

The resulting density distribution and output parameters from an inversion of data calculated from boreholes located at $(x, y) \rightarrow (150, 300)$, $(x, y) \rightarrow (200, 300)$, $(x, y) \rightarrow (250, 300)$, $(x, y) \rightarrow (300, 300)$, $(x, y) \rightarrow (350, 300)$, $(x, y) \rightarrow (400, 300)$ and $(x, y) \rightarrow (450, 300)$.

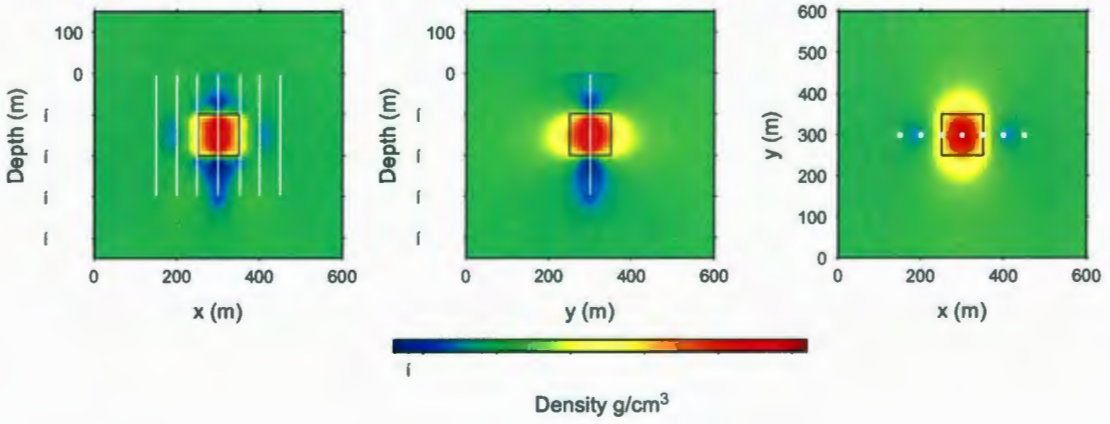

Figure A.14. Inversion results for a block–in–a–halfspace from seven boreholes. *left*: the x–slice, *middle*: the y–slice; *right*: the z–slice. Borehole locations are displayed in white. The true block model is outlined in black.

- $\rho_{max} = 2.00$ g/cm^3
- $\rho_{min} = -0.683$ g/cm^3
- $\beta = 0.13000E - 05$
- $\phi_d = 251.99$
- $\phi_m = 0.10588E + 10$
- $\Phi = 1628.4$

A.15 Eight Boreholes

The resulting density distribution and output parameters from an inversion of data calculated from boreholes located at $(x, y) \rightarrow (150, 150)$, $(x, y) \rightarrow (150, 300)$ $(x, y) \rightarrow (150, 450)$, $(x, y) \rightarrow (300, 450)$, $(x, y) \rightarrow (450, 450)$, $(x, y) \rightarrow (450, 300)$, $(x, y) \rightarrow (450, 150)$ and $(x, y) \rightarrow (300, 150)$.

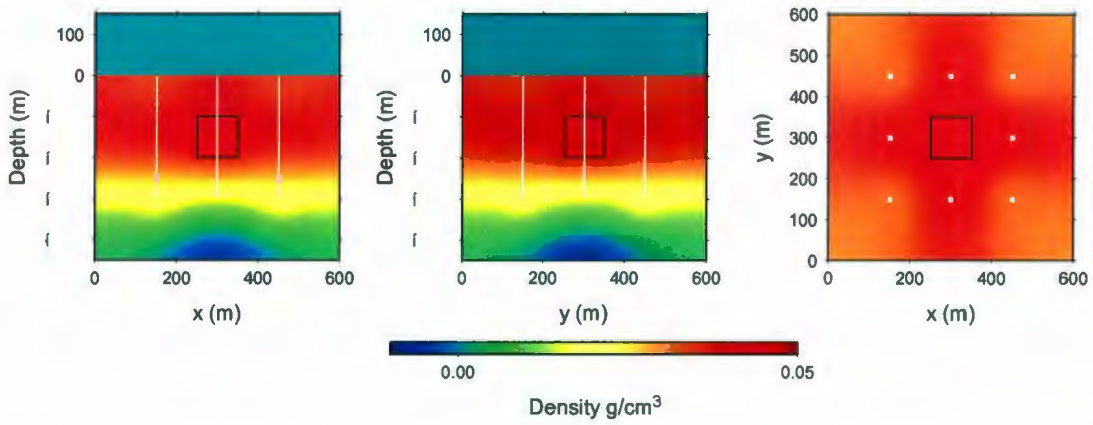

Figure A.15. Inversion results for a block–in–a–halfspace from two boreholes. *left*: the x–slice, *middle*: the y–slice; *right*: the z–slice. Borehole locations are displayed in white. The true block model is outlined in black.

- $\rho_{max} = 0.0436$ g/cm^3
- $\rho_{min} = -0.00387$ g/cm^3
- $\beta = 0.21000E - 02$
- $\phi_d = 344.12$
- $\phi_m = 72990.$
- $\Phi = 497.40$

A.16 Eight + Surface Data

The resulting density distribution and output parameters from an inversion of data calculated at the surface and boreholes located at $(x, y) \rightarrow (150, 150)$, $(x, y) \rightarrow (150, 300)$ $(x, y) \rightarrow (150, 450)$, $(x, y) \rightarrow (300, 450)$, $(x, y) \rightarrow (450, 450)$, $(x, y) \rightarrow (450, 300)$, $(x, y) \rightarrow (450, 150)$ and $(x, y) \rightarrow (300, 150)$.

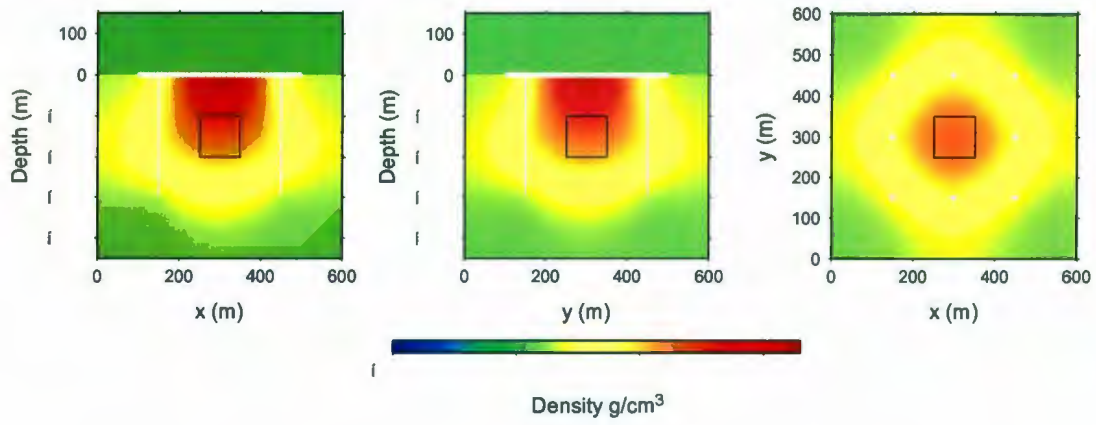

Figure A.16. Inversion results for a block–in–a–halfspace from surface data and eight boreholes. *left*: the x–slice, *middle*: the y–slice; *right*: the z–slice. Borehole locations are displayed in white and surface locations are shown in white dots. The true block model is outlined in black.

- $\rho_{max} = 0.113$ g/cm^3
- $\rho_{min} = 0.0$ g/cm^3
- $\beta = 0.60000E - 03$
- $\phi_d = 1983.4$
- $\phi_m = 0.35081E + 07$
- $\Phi = 4088.3$

A.17 Eight Diamond

The resulting density distribution and output parameters from an inversion of data calculated at the surface and boreholes located at $(x, y) \rightarrow (200, 300)$, $(x, y) \rightarrow (300, 200)$ $(x, y) \rightarrow (400, 300)$, $(x, y) \rightarrow (300, 400)$, $(x, y) \rightarrow (250, 250)$, $(x, y) \rightarrow (350, 350)$, $(x, y) \rightarrow (350, 250)$ and $(x, y) \rightarrow (250, 350)$.

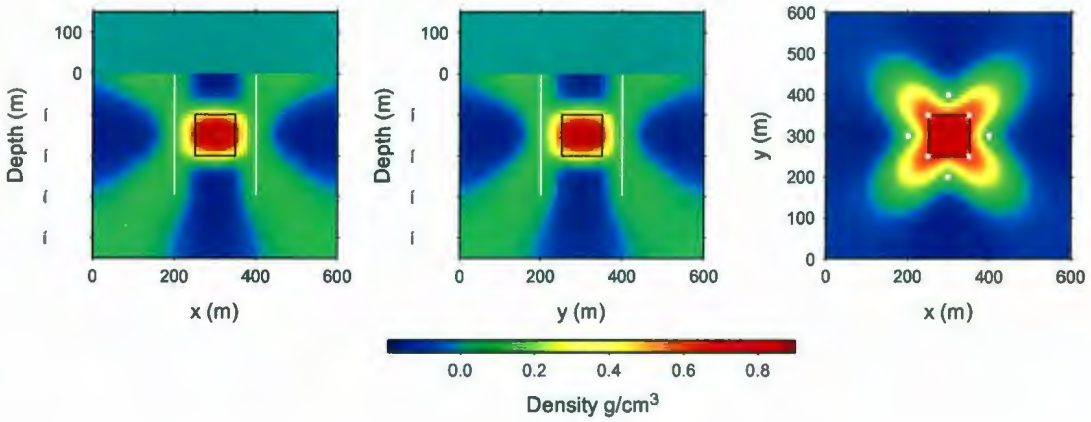

Figure A.17. Inversion results for a block–in–a–halfspace from eight boreholes. *left*: the x–slice, *middle*: the y–slice; *right*: the z–slice. Borehole locations are displayed in white and surface locations are shown in white dots. The true block model is outlined in black.

- $\rho_{max} = 0.85$ g/cm^3
- $\rho_{min} = -0.193$ g/cm^3
- $\beta = 0.65000E - 05$
- $\phi_d = 319.28$
- $\phi_m = 0.16285E + 09$
- $\Phi = 1377.8$

A.18 Nine

The resulting density distribution and output parameters from an inversion using data calculated from boreholes located at $(x, y) \rightarrow (150, 150)$, $(x, y) \rightarrow (150, 300)$ $(x, y) \rightarrow (150, 450)$, $(x, y) \rightarrow (300, 450)$, $(x, y) \rightarrow (450, 450)$, $(x, y) \rightarrow (450, 300)$, $(x, y) \rightarrow (450, 150)$ $(x, y) \rightarrow (300, 150)$ and $(x, y) \rightarrow (300, 300)$.

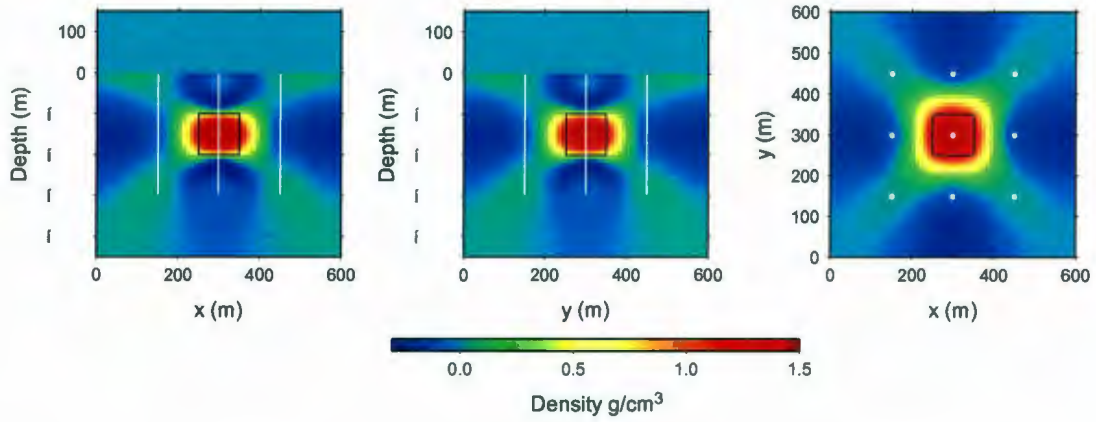

Figure A.18. Inversion results for a block–in–a–halfspace from nine boreholes. *left*: the x–slice, *middle*: the y–slice; *right*: the z–slice. Borehole locations are displayed in white. The true block model is outlined in black.

- $\rho_{max} = 1.48$ g/cm^3
- $\rho_{min} = -0.289$ g/cm^3
- $\beta = 0.35000E - 05$
- $\phi_d = 349.13$
- $\phi_m = 0.33021E + 09$
- $\Phi = 1504.9$

APPENDIX B

Wedge–in–a–Halfspace–Models

In the following appendix, more inversion results are shown for different scenarios of borehole data and locations for a wedge–in–a–halfspace model. The mesh used is the wedge density model and for results has dimensions $(x, y, z) \rightarrow (0, 0, 150) : (600, 600, -450)$ and cell sizes of 10m in each direction. The mesh therefore contain 216,000 cells. A wedge with a density of 2.0 g/cm^3 is located at the center of the mesh. The y–coordinates of the wedge are $(y) \rightarrow (250 : 350)$. The x– and z– coordinates of the wedge decrease by 10m per cell, the x– and z–coordinate are $(x, z) \rightarrow (250, -100) : (350, -110)$ to $(x, z) \rightarrow (250, -100) : (350, -200)$. The cells outside of the wedge have a background density of zero. The wedge density model is shown in Figure 18. All borehole data observation points are calculated along boreholes which travels from $(z) \rightarrow (-3.846 : -296.153)$ m. A total of thirty nine observations are taken at evenly spaced intervals at approximately every 7.7 m. Random Gaussian noise of standard deviation equal to five percent of the magnitude of the datum is added to all data–sets. If surface data is included in the inversion, a total of 1521 data points are taken at the surface $(z = 0)$ from $(x, y) \rightarrow (105.13, 105.13) : (494.87, 494.87)$ m. Thus measurements are calculated at approximately every 10.25 m.

B.1 One Borehole + Surface Data

The resulting density distribution and output parameters from an inversion of data calculated at the surface and a borehole located at $(x, y) \rightarrow (300, 300)$

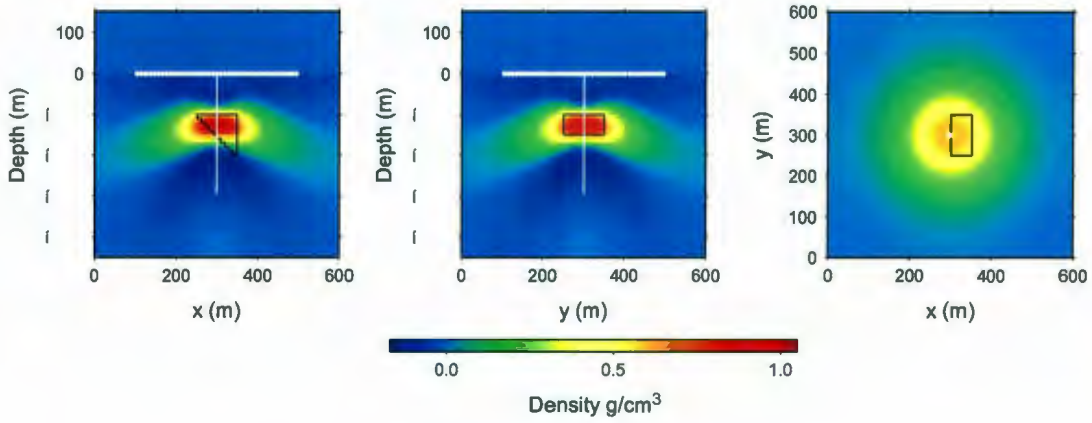

Figure B.1. Inversion results for a wedge–in–a–halfspace from surface data and a borehole. *left*: the x–slice, *middle*: the y–slice; *right*: the z–slice. Borehole location is displayed in white and the surface locations are displayed in white dots. The true wedge model is outlined in black.

- $\rho_{max} = 1.02$ g/cm^3
- $\rho_{min} = -0.162$ g/cm^3
- $\beta = 0.33000E - 04$
- $\phi_d = 1554.6$
- $\phi_m = 0.71630E + 08$
- $\Phi = 3918.4$

B.2 One Far, One Middle

The resulting density distribution and output parameters from an inversion of data calculated from boreholes located at $(x, y) \rightarrow (150, 300)$ and $(x, y) \rightarrow (300, 300)$.

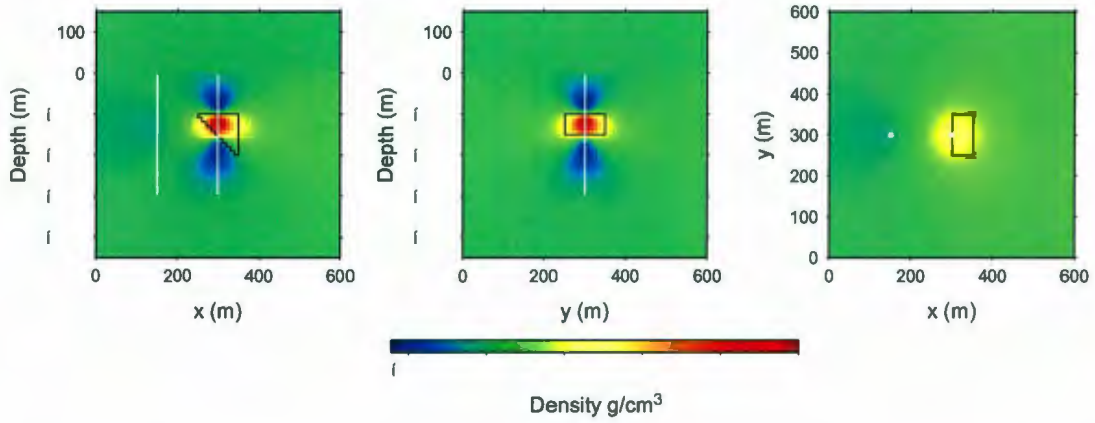

Figure B.2. Inversion results for a wedge–in–a–halfspace from two boreholes. *left*: the x–slice, *middle*: the y–slice; *right*: the z–slice. Borehole locations are displayed in white. The true wedge model is outlined in black.

- $\rho_{max} = 1.96$ g/cm^3
- $\rho_{min} = -0.608$ g/cm^3
- $\beta = 0.90000E - 06$
- $\phi_d = 73.857$
- $\phi_m = 0.59101E + 09$
- $\Phi = 605.76$

B.3 One Far, One Middle 2

The resulting density distribution and output parameters from an inversion of data calculated from boreholes located at $(x, y) \rightarrow (450, 300)$ and $(x, y) \rightarrow (300, 300)$.

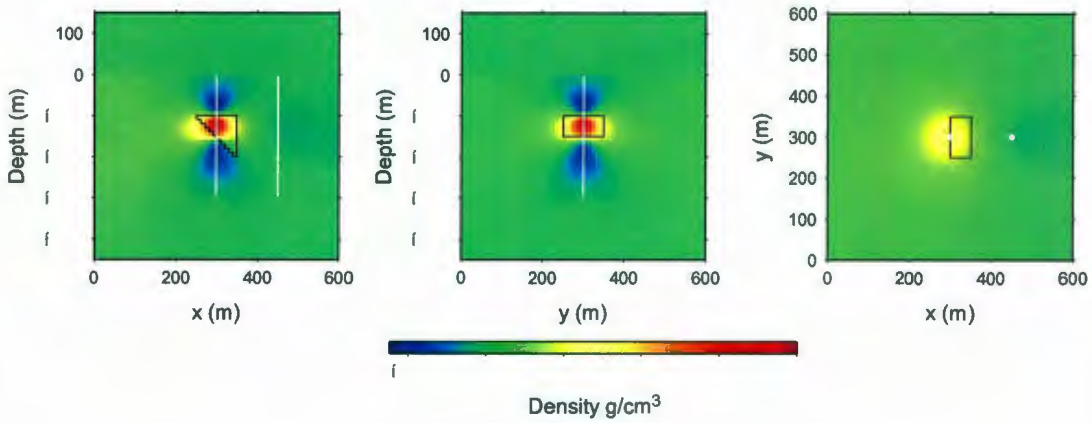

Figure B.3. Inversion results for a wedge–in–a–halfspace from two boreholes. *left*: the x–slice, *middle*: the y–slice; *right*: the z–slice. Borehole locations are displayed in white. The true wedge model is outlined in black.

- $\rho_{max} = 1.96$ g/cm^3
- $\rho_{min} = -0.613$ g/cm^3
- $\beta = 0.88000E - 06$
- $\phi_d = 71.595$
- $\phi_m = 0.58964E + 09$
- $\Phi = 590.47$

B.4 One Half, One Middle

The resulting density distribution and output parameters from an inversion of data calculated from boreholes located at $(x, y) \rightarrow (200, 300)$ and $(x, y) \rightarrow (300, 300)$.

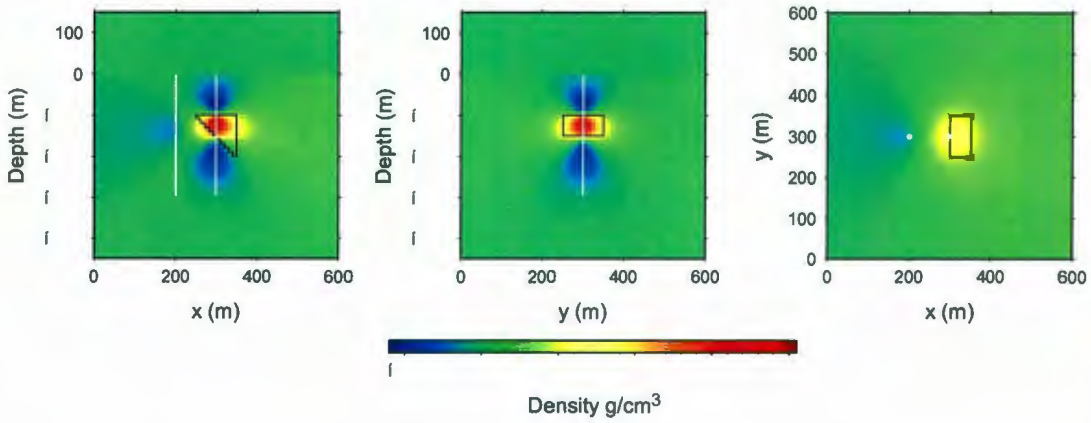

Figure B.4. Inversion results for a wedge–in–a–halfspace from two boreholes. *left*: the x–slice, *middle*: the y–slice; *right*: the z–slice. Borehole locations are displayed in white. The true wedge model is outlined in black.

- $\rho_{max} = 2.01$ g/cm^3
- $\rho_{min} = -0.597$ g/cm^3
- $\beta = 0.89000E - 06$
- $\phi_d = 72.063$
- $\phi_m = 0.59912E + 09$
- $\Phi = 605.28$

B.5 One Half, One Middle 2

The resulting density distribution and output parameters from an inversion of data calculated from boreholes located at $(x, y) \rightarrow (400, 300)$ and $(x, y) \rightarrow (300, 300)$.

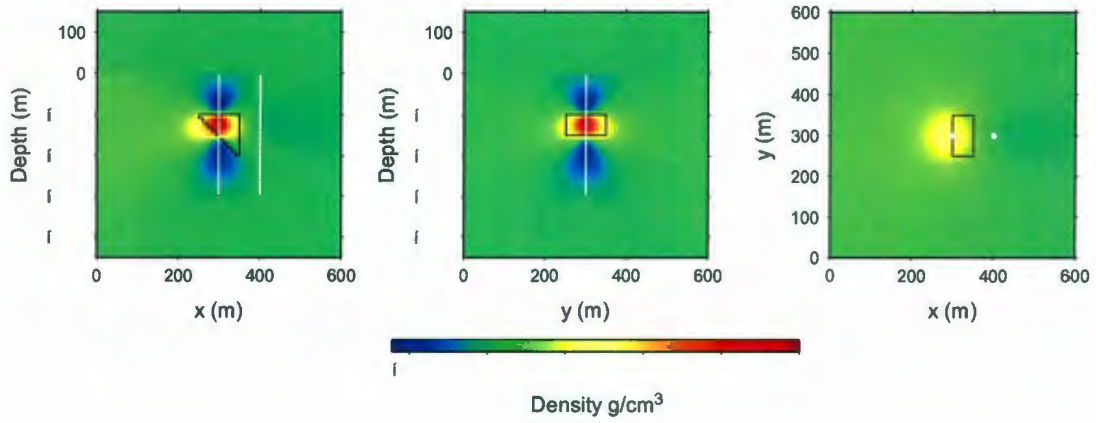

Figure B.5. Inversion results for a wedge–in–a–halfspace from two boreholes. *left*: the x–slice, *middle*: the y–slice; *right*: the z–slice. Borehole locations are displayed in white. The true wedge model is outlined in black.

- $\rho_{max} = 1.99$ g/cm^3
- $\rho_{min} = -0.604$ g/cm^3
- $\beta = 0.88000E - 06$
- $\phi_d = 70.404$
- $\phi_m = 0.58510E + 09$
- $\Phi = 585.29$

B.6 One Edge, One Middle

The resulting density distribution and output parameters from an inversion of data calculated from boreholes located at $(x, y) \rightarrow (250, 300)$ and $(x, y) \rightarrow (300, 300)$.

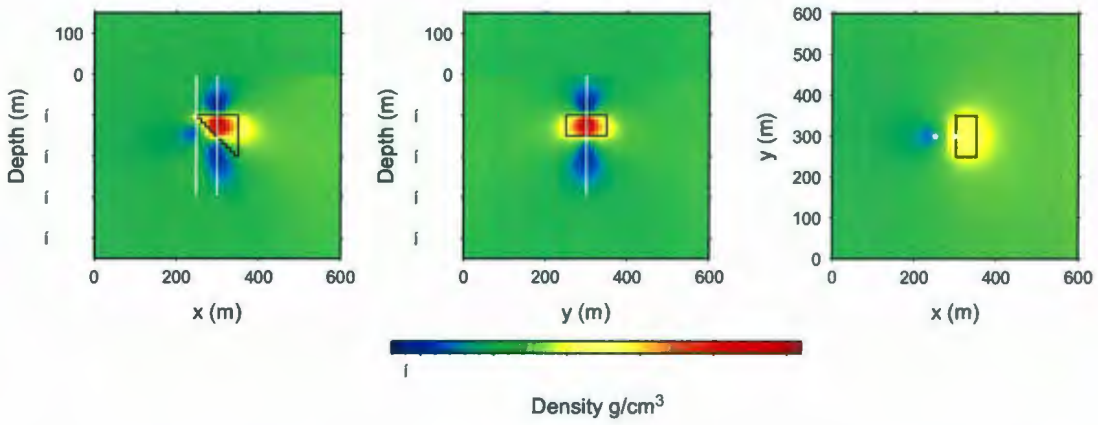

Figure B.6. Inversion results for a wedge–in–a–halfspace from two boreholes. *left*: the x–slice, *middle*: the y–slice; *right*: the z–slice. Borehole locations are displayed in white. The true wedge model is outlined in black.

- $\rho_{max} = 2.08$ g/cm^3
- $\rho_{min} = -0.637$ g/cm^3
- $\beta = 0.78000E - 06$
- $\phi_d = 82.101$
- $\phi_m = 0.67982E + 09$
- $\Phi = 612.36$

B.7 One Edge, One Middle 2

The resulting density distribution and output parameters from an inversion of data calculated from boreholes located at $(x, y) \rightarrow (350, 300)$ and $(x, y) \rightarrow (300, 300)$.

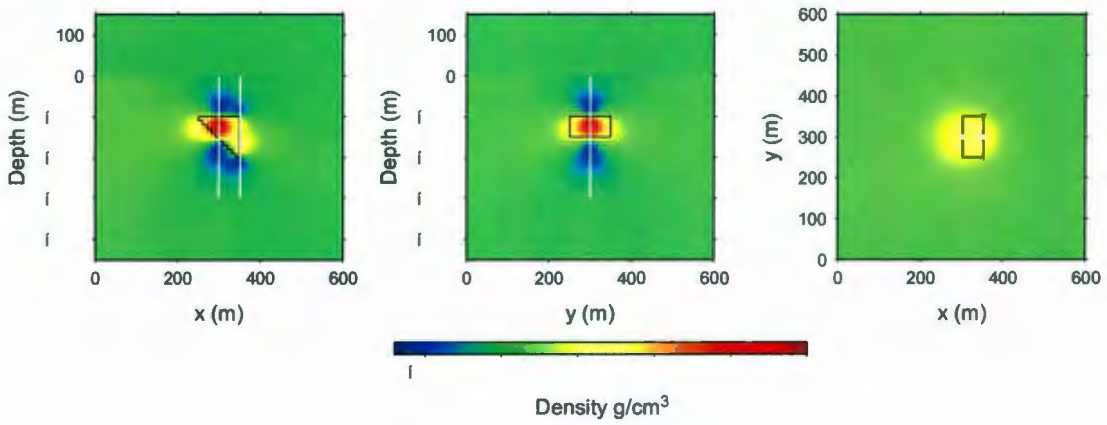

Figure B.7. Inversion results for a wedge–in–a–halfspace from two boreholes. *left*: the x–slice, *middle*: the y–slice; *right*: the z–slice. Borehole locations are displayed in white. The true wedge model is outlined in black.

- $\rho_{max} = 1.96$ g/cm^3
- $\rho_{min} = -0.611$ g/cm^3
- $\beta = 0.80000E-06$
- $\phi_d = 72.546$
- $\phi_m = 0.63229E+09$
- $\Phi = 578.38$

B.8 One Edge, One Half

The resulting density distribution and output parameters from an inversion of data calculated from boreholes located at $(x, y) \rightarrow (250, 300)$ and $(x, y) \rightarrow (400, 300)$.

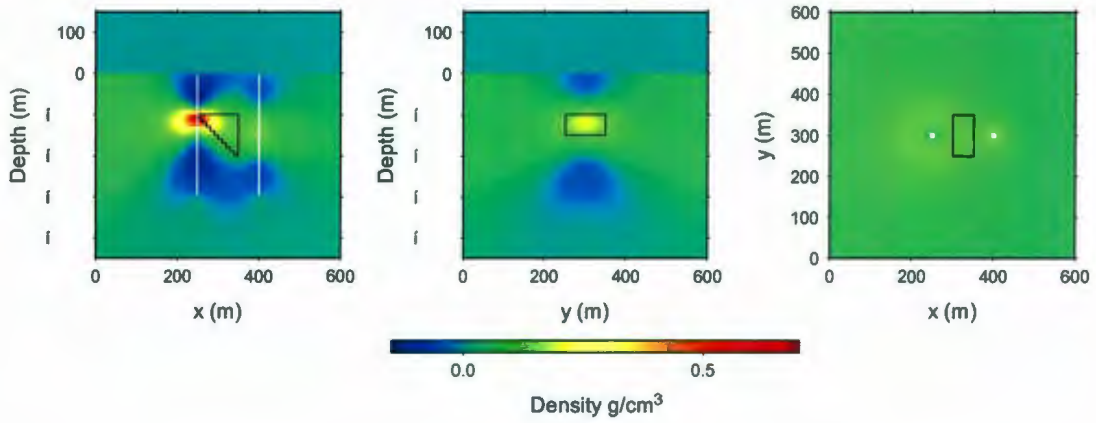

Figure B.8. Inversion results for a wedge–in–a–halfspace from two boreholes. *left*: the x–slice, *middle*: the y–slice; *right*: the z–slice. Borehole locations are displayed in white. The true wedge model is outlined in black.

- $\rho_{max} = 0.692$ g/cm^3
- $\rho_{min} = -0.13$ g/cm^3
- $\beta = 0.33500E - 05$
- $\phi_d = 84.861$
- $\phi_m = 0.59420E + 08$
- $\Phi = 283.92$

B.9 One Edge, One Half 2

The resulting density distribution and output parameters from an inversion of data calculated from boreholes located at $(x, y) \rightarrow (350, 300)$ and $(x, y) \rightarrow (200, 300)$.

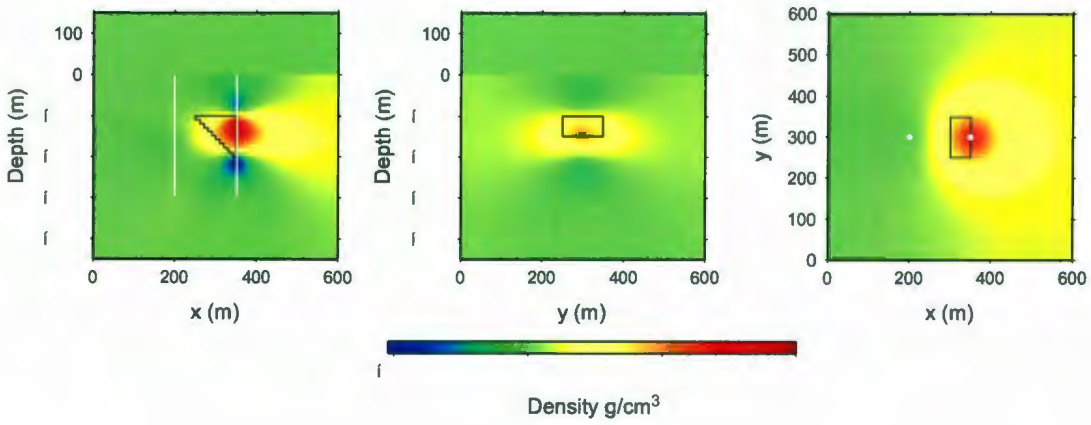

Figure B.9. Inversion results for a wedge–in–a–halfspace from two boreholes. *left*: the x–slice, *middle*: the y–slice; *right*: the z–slice. Borehole locations are displayed in white. The true wedge model is outlined in black.

- $\rho_{max} = 0.91$ g/cm^3
- $\rho_{min} = -0.519$ g/cm^3
- $\beta = 0.27000E - 05$
- $\phi_d = 84.377$
- $\phi_m = 0.17283E + 09$
- $\Phi = 551.01$

B.10 One Edge, One Half 3

The resulting density distribution and output parameters from an inversion of data calculated from boreholes located at $(x, y) \rightarrow (350, 300)$ and $(x, y) \rightarrow (400, 300)$.

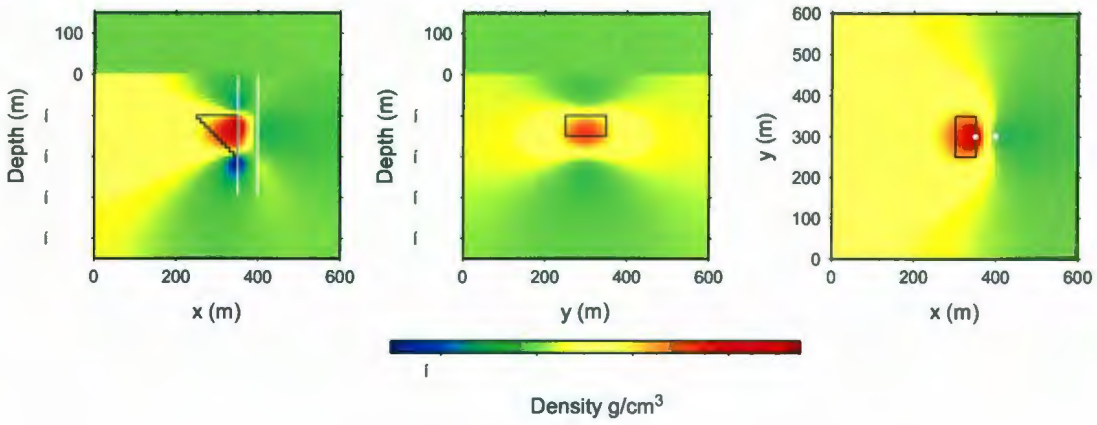

Figure B.10. Inversion results for a wedge–in–a–halfspace from two boreholes. *left*: the x–slice, *middle*: the y–slice; *right*: the z–slice. Borehole locations are displayed in white. The true wedge model is outlined in black.

- $\rho_{max} = 1.08$ g/cm^3
- $\rho_{min} = -0.607$ g/cm^3
- $\beta = 0.19700E - 05$
- $\phi_d = 82.979$
- $\phi_m = 0.23458E + 09$
- $\Phi = 545.10$

B.11 One Edge, One Half 4

The resulting density distribution and output parameters from an inversion of data calculated from boreholes located at $(x, y) \rightarrow (250, 300)$ and $(x, y) \rightarrow (200, 300)$.

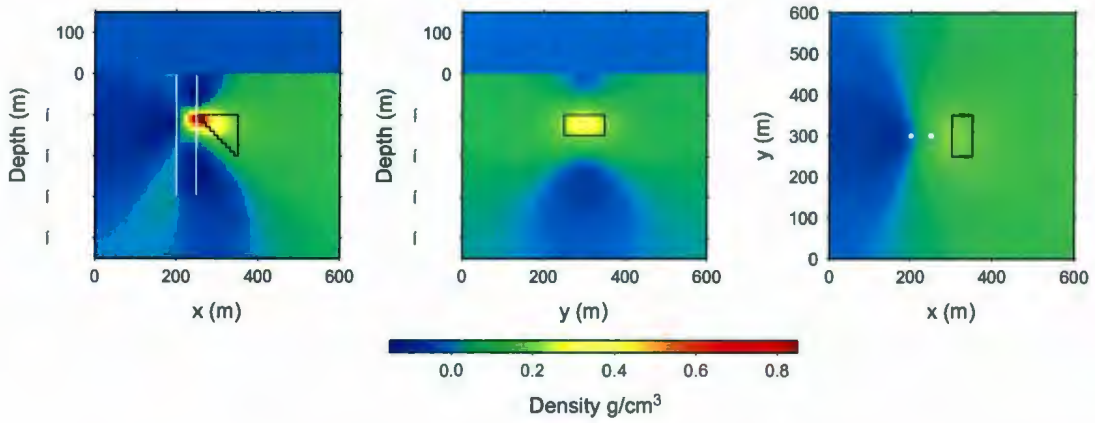

Figure B.11. Inversion results for a wedge–in–a–halfspace from two boreholes. *left*: the x–slice, *middle*: the y–slice; *right*: the z–slice. Borehole locations are displayed in white. The true wedge model is outlined in black.

- $\rho_{max} = 0.831$ g/cm^3
- $\rho_{min} = -0.131$ g/cm^3
- $\beta = 0.26000E - 05$
- $\phi_d = 79.820$
- $\phi_m = 0.77474E + 08$
- $\Phi = 281.25$

B.12 Two Edge

The resulting density distribution and output parameters from an inversion of data calculated from boreholes located at $(x, y) \rightarrow (250, 300)$ and $(x, y) \rightarrow (350, 300)$.

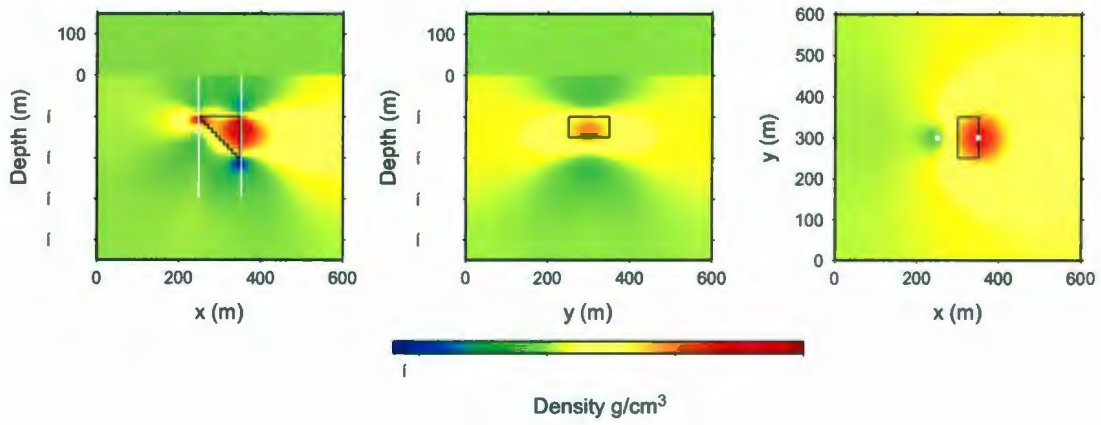

Figure B.12. Inversion results for a wedge–in–a–halfspace from two boreholes. *left*: the x–slice, *middle*: the y–slice; *right*: the z–slice. Borehole locations are displayed in white. The true wedge model is outlined in black.

- $\rho_{max} = 0.917$ g/cm^3
- $\rho_{min} = -0.560$ g/cm^3
- $\beta = 0.15000E - 05$
- $\phi_d = 75.059$
- $\phi_m = 0.23916E + 09$
- $\Phi = 433.80$

B.13 Two Edge, One Middle

The resulting density distribution and output parameters from an inversion of data calculated from boreholes located at $(x, y) \rightarrow (250, 300)$, $(x, y) \rightarrow (300, 300)$ and $(x, y) \rightarrow (350, 300)$.

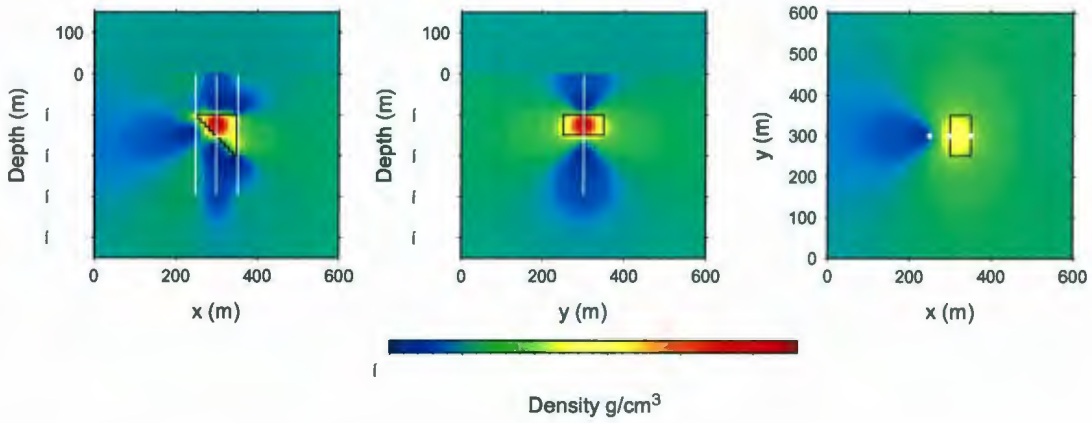

Figure B.13. Inversion results for a wedge–in–a–halfspace from two boreholes. *left*: the x–slice, *middle*: the y–slice; *right*: the z–slice. Borehole locations are displayed in white. The true wedge model is outlined in black.

- $\rho_{max} = 2.27$ g/cm^3
- $\rho_{min} = -0.473$ g/cm^3
- $\beta = 0.87000E - 06$
- $\phi_d = 123.97$
- $\phi_m = 0.75142E + 09$
- $\Phi = 777.71$

B.14 One Middle, Two Edge Corner

The resulting density distribution and output parameters from an inversion of data calculated from boreholes located at $(x, y) \rightarrow (250, 250)$, $(x, y) \rightarrow (300, 300)$ and $(x, y) \rightarrow (350, 350)$.

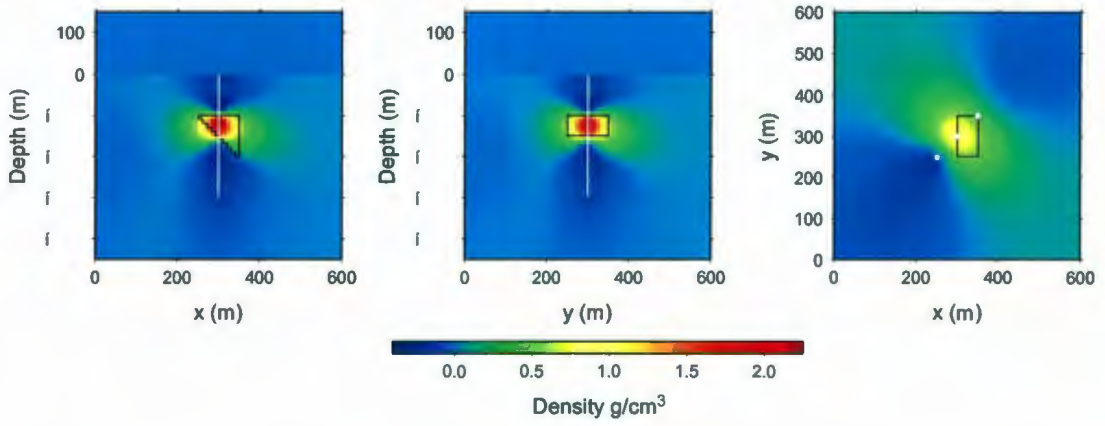

Figure B.14. Inversion results for a wedge–in–a–halfspace from three boreholes. *left*: the x–slice, *middle*: the y–slice; *right*: the z–slice. Borehole locations are displayed in white. The true wedge model is outlined in black.

- $\rho_{max} = 2.23$ g/cm^3
- $\rho_{min} = -0.398$ g/cm^3
- $\beta = 0.97000E-06$
- $\phi_d = 105.98$
- $\phi_m = 0.67452E+09$
- $\Phi = 760.26$

B.15 Seven Line

The resulting density distribution and output parameters from an inversion of data calculated from boreholes located at $(x, y) \rightarrow (150, 300)$, $(x, y) \rightarrow (200, 300)$, $(x, y) \rightarrow (250, 300)$, $(x, y) \rightarrow (300, 300)$, $(x, y) \rightarrow (350, 300)$, $(x, y) \rightarrow (400, 300)$ and $(x, y) \rightarrow (450, 300)$.

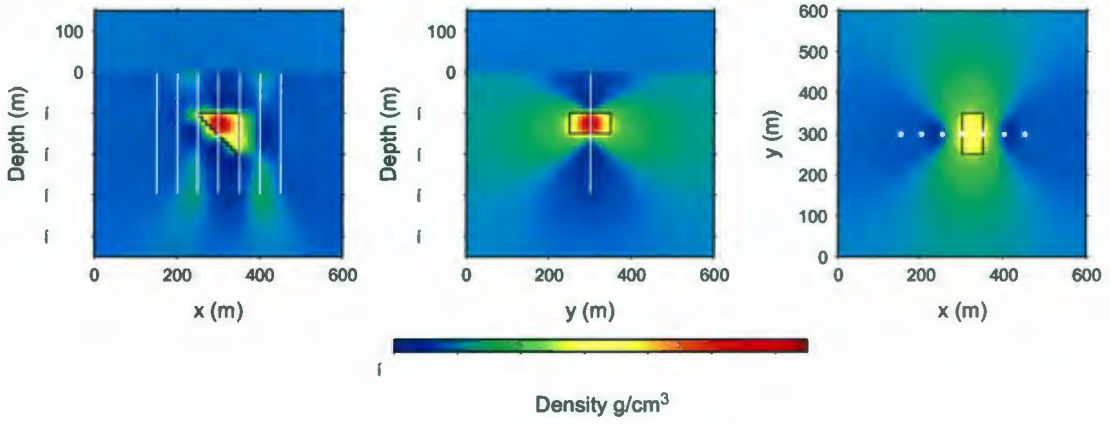

Figure B.15. Inversion results for a wedge–in–a–halfspace from three boreholes. *left*: the x–slice, *middle*: the y–slice; *right*: the z–slice. Borehole locations are displayed in white. The true wedge model is outlined in black.

- $\rho_{max} = 2.19$ g/cm^3
- $\rho_{min} = -0.357$ g/cm^3
- $\beta = 0.15000E - 05$
- $\phi_d = 266.93$
- $\phi_m = 0.75073E + 09$
- $\Phi = 1393.0$

B.16 Eight Diamond

The resulting density distribution and output parameters from an inversion of data calculated at the surface and boreholes located at $(x, y) \rightarrow (200, 300)$, $(x, y) \rightarrow (300, 200)$ $(x, y) \rightarrow (400, 300)$, $(x, y) \rightarrow (300, 400)$, $(x, y) \rightarrow (250, 250)$, $(x, y) \rightarrow (350, 350)$, $(x, y) \rightarrow (350, 250)$ and $(x, y) \rightarrow (250, 350)$.

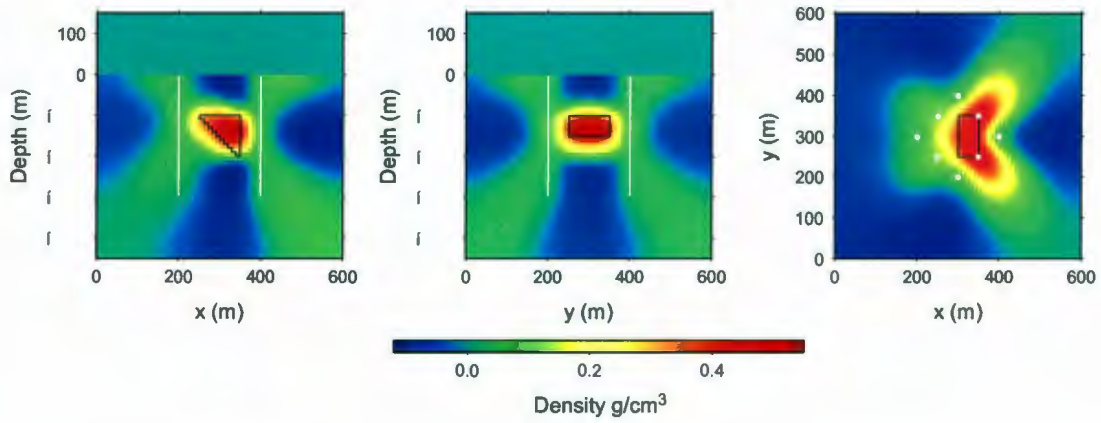

Figure B.16. Inversion results for a wedge–in–a–halfspace from three boreholes. *left*: the x–slice, *middle*: the y–slice; *right*: the z–slice. Borehole locations are displayed in white. The true wedge model is outlined in black.

- $\rho_{max} = 0.535$ g/cm^3
- $\rho_{min} = -0.117$ g/cm^3
- $\beta = 0.10000E - 04$
- $\phi_d = 295.26$
- $\phi_m = 0.65861E + 08$
- $\Phi = 953.87$